Développement de points quantiques de pérovskite pour la technologie de l'information quantique tout optique et la spintronique

Minh Tuan Duong

THÈSE

Pour obtenir le grade de

DOCTEUR DE L'UNIVERSITÉ GRENOBLE ALPES

École doctorale : CSV- Chimie et Sciences du Vivant
Spécialité : Chimie Physique Moléculaire et Structurale
Unité de recherche : Systèmes Moléculaires et Nano Matériaux pour l'Énergie et la Santé

Développement de points quantiques de pérovskite pour la technologie de l'information quantique tout optique et la spintronique

Development of Perovskite Quantum Dots for All-Optical Quantum Information Technology and Spintronics

Présentée par :

Minh Tuan DUONG

Direction de thèse :

Peter REISS Chercheur, chef de laboratoire, CEA	Directeur de thèse
Gilles NOGUES DIRECTEUR DE RECHERCHE, Université Grenoble Alpes	Co-encadrant de thèse

Rapporteurs :

Yannick MUGNIER
MAITRE DE CONFERENCE HDR, Université de Chambéry
Maria CHAMARRO
PROFESSEUR DES UNIVERSITES, Sorbonne Université

Thèse soutenue publiquement le **3 mars 2023**, devant le jury composé de :

Alain IBANEZ DIRECTEUR DE RECHERCHE, CNRS délégation Alpes	Président
Céline TERNON MAITRE DE CONFERENCES HDR, Grenoble INP	Examinatrice
Yannick MUGNIER MAITRE DE CONFERENCE HDR, Université de Chambéry	Rapporteur
Maria CHAMARRO PROFESSEUR DES UNIVERSITES, Sorbonne Université	Rapporteure

Invités :

Peter Reiss
DIRECTEUR DE RECHERCHE, CEA Grenoble
Gilles Nogues
DIRECTEUR DE RECHERCHE, Institut NEEL CNRS

Acknowledgement

First and foremost, I would like to express my sincere gratitude to my supervisors, Dr. Peter Reiss and Dr. Gilles Nogues. You let me freely explore my thesis topic, giving valuable advices along the way. You punish not my errors, using them instead to teach. Most importantly, you taught me the joy and woe of academic research.

I would also like to express my appreciation to my unofficial advisers, Prof. Lê Sĩ Đảng, and Prof. Stéphanie Pouget. Scientific discussions with you were always a pleasure as they provided not only fundamental knowledge, but also scientific thinking. Furthermore, your dedication to research has been most inspiring.

I would like to thank the members of my jury for evaluating my thesis despite their busy schedules. I greatly appreciate all the constructive discussion during the defense as well as the meaningful words of encouragement you gave me.

This thesis would not have been completed without the help with characterization and analysis from Mme. Céline Rivaux (ICP-AES), Dr. Wai Li Ling (TEM), and Prof. David Ferrand (micro-PL). For that, I offer you my thanks. A special thank is also given to Dr. Dmitry Aldakov (XPS), who not only helped me with science, but also provided quality of life with his jokes, stories, and his requests to leave the lab before 6 p.m.

To the former and current non-permanent members of the STEP team that I've had the pleasure to know, thank you for your help and your stories.

To the boy bound by the past and duty, who dreams still, thank you for the kinship. o_/

To the people in that reed field, thank you for the inspiration.

To my parents, flawed and beautiful, the anchor. To my sister, who inherited the fortitude of our parents. To Grandmother, still teaching from the beyond. These lines are dedicated to you.

And to my haven, my burden, thank you.

Table of Contents

List of Figures and Tables

Figures

Chapter 1

Chapter 2

Chapter 3

Chapter 4

Appendices

Tables

List of abbreviations

AFM	Atomic force microscopy
APD	Avalanche photodiode
CBM	Conduction band minimum
CCD	Charge-coupled device
CW	Continuous-wave
DBM	Dibromomethane
DMS	Diluted magnetic semiconductor
EDX	Energy dispersive X-ray spectroscopy
FTIR	Fourrier-transform infrared spectroscopy
HBT	Hanbury Brown - Twiss
HI	Hot injection
ICDD	International Center for Diffraction Data
ICP-AES	Inductively coupled plasma - atomic emission spectroscopy
LARP	Ligand-assisted reprecipitation
LHP	Lead halide perovskite
LO	Longitudinal optical
MW	Molecular weight
NC	Nanocrystal
OA	Oleic acid
ODE	1-octadecene
OLA	Oleylamine
OTMS	Octadecyltrimethoxysilane
PL	Photoluminescence
QY	Quantum yield
RKKY	Ruderman–Kittel–Kasuya–Yosida
SEM	Scanning electron microscopy
TEM	Transmission electron microscopy
TOP	Trioctylphosphine
TOPO	Trioctylphosphine oxide
UV - vis	Ultra violet - visible
VBM	Valence band maximum
XPS	X-ray photoelectron spectroscopy
XRD	X-ray diffraction

Introduction

Having been discovered and characterized as early as the 1950s, lead halide perovskites (LHP) only broke into the research spotlight since the 2010s. This class of materials possesses highly desirable properties for photovoltaics research: low, easily tunable band gap, high charge mobility, and facile synthesis suitable for up-scaled fabrication. As a matter of fact, the efficiency of perovskite solar cells has rapidly increased since their initial conception reaching a power conversion efficiency of 3.8% in 2009 to 25.7% in 2022.[1-2] However, research on LHP has extended far beyond this field. As a semiconductor, LHP can take advantage of the quantum confinement effect in the form of nanocrystals. They exhibit highly efficient luminescence, defect tolerance, and easy emission tuning by composition. Furthermore, in-depth investigations into the physics of LHP, especially at low temperature, has yielded valuable insight and revealed unique features of the system. Despite the vast body of research on LHP, the lack of robustness of the material is a formidable challenge in practical implementation. As an ionic compound, LHP can quickly degrade on contact with water. For nanocrystals, the surfactants (ligands) meant to passivate the surface and prevent particle agglomeration do not bind strongly. As a result, the nanocrystals are highly susceptible to the environment.

Another reason for the surge in perovskite nanocrystal research is the emerging importance of quantum technology. Since the beginning of quantum mechanics as a science, our efforts to construct a framework to understand nature has gradually allowed us to create and control quantum objects, especially with recent advances in the field. The next step, which is to turn these objects into technologies and products, has received much attention and funding from governments around the world.[3] For example, the European Union has launched several initiatives since 2016, with the most ambitious being the Quantum Technology Flagship program, with a budget of at least €1 billion for 10 years. In this technology, devices operate using single photons and electron spin, and algorithms take advantage of quantum effects such as superposition and entanglement to perform calculations. As such, there is a great demand for systems that can generate these quantum objects at a high rate and precision. In many cases, semiconductor nanocrystals have a high potential to be an integral part of these systems.

In the above context, this thesis has been carried out with three major objectives. The first aim is to improve the stability of lead halide perovskite nanocrystals on a single particle level. This will allow robust and high-performing nanocrystals to be integrated individually into quantum devices, which is the second goal of the thesis. Here, the nanocrystals will be used as single photon emitters coupled to a nanopatch antenna. A final objective of the thesis was – depending on the progress in the first two – to study the capability of the nanocrystals to demonstrate charge carrier-dependent magnetic properties when doped with magnetic ions. This effect has been researched extensively for other nanocrystal systems from II-VI and III-V binary compounds and is very important for spintronics. However, only preliminary works have been performed on LHP nanocrystals, resulting in a relatively unexplored research topic.

Chapter 1 provides the general introduction to the topics covered in this thesis. The first are lead halide perovskite nanocrystals. Their physical properties are reviewed along with their colloidal synthesis, with an emphasis on the hot-injection method. Afterward, the research on surface passivation is summarized. The next section focuses on single photon emitters. The basic physics of single photons, as well as their generation and detection are introduced. A brief review on the use of

structures known as nanoantenna to direct emitted photons is also given. The final topic is diluted magnetic semiconductors. Their electronic structures are presented, followed by different types of exchange interaction in the materials. The resulting magneto-optical properties are then discussed, focusing on the giant Zeeman effect in particular.

Chapter 2 details the synthesis and characterization of $CsPbBr_3$ nanocrystals and the $CsPbBr_3/AlO_x$ core/shell structures. Afterward, different shelling strategies are discussed, focusing on the anchoring of shell precursors on the surface of the core nanocrystals. The overall success of the strategies is then reflected by the results of photostability tests, the design of which is discussed in-depth.

Chapter 3 presents the process of fabricating nanopatch antennas where Ag nanocubes reside on a thin film of $CsPbBr_3$ and $CsPbBr_3/AlO_x$ nanocrystals. The process is broken down into several steps, and the optimization of the relevant parameters is discussed. Finally, the performance of the structure in terms of emission rate enhancement is evaluated.

Chapter 4 focuses on the doping of $CsPbBr_3$ nanocrystals with Al^{3+} and Mn^{2+}. Cation doping is an established method to tune the emission energy of nanocrystals (Al^{3+}) as well as give them novel properties (Mn^{2+}). The structural and spectroscopic investigations of these doped nanocrystals are detailed, and hypotheses on the origin of observed features are proposed.

References

1. National Renewable Energy Laboratory. Best Research-Cell Efficiency Chart. https://www.nrel.gov/pv/cell-efficiency.html (accessed Dec 22, 2022).
2. Kojima, A.; Teshima, K.; Shirai, Y.; Miyasaka, T., Organometal halide perovskites as visible-light sensitizers for photovoltaic cells. *J. Am. Chem. Soc.* **2009,** *131* (17), 6050-1.
3. Thew, R.; Jennewein, T.; Sasaki, M., Focus on quantum science and technology initiatives around the world. *Quantum Sci. Technol* **2019,** *5* (1), 010201.

Chapter 1: General introduction

Lead halide perovskite nanocrystals

History of lead halide perovskite nanocrystals

Despite gaining immense research interest in the last decade, the development history of lead halide perovskite dates back to the late 19th century, with the discovery of their existence.[1] The study of the material was continued in 1957-1958, when the crystal structure, phase transitions and photoconductivity of $CsPbX_3$ (X= Cl, Br, I) were determined.[2-3] In the late 1990s and early 2000s, the focus was placed on the optical and excitonic properties of lead halide perovskite structures.

A breakthrough was made when methylammonium lead halide films were used as light absorber with a TiO_2 electron transport layer in a dye-sensitized solar cell configuration.[4] At first, studies coupling perovskite with liquid electrolytes reported low efficiency (<7%). It was not until 2012, when a solid-state hole transporting layer was used instead, that a high efficiency of 9.7% was reached.[5] The following years marked a rapid progress in the field of perovskite solar cell, in which the halide perovskites were used in different solar cell architectures. The current record performance of a perovskite solar cell is 25.7%, fast approaching the efficiency range of crystalline Si cells (27.6%), the dominant technology in the solar cell market.[6]

At the same time, interest in the material also rose within the colloidal quantum dots community. In 2014, $MAPbBr_3$ nanocrystals (NCs) were synthesized for the first time without the use of templates.[7] Shortly after, a hot-injection pathway for the synthesis of $CsPbX_3$ NCs (X=Cl, Br, I) was proposed, which was able to obtain highly luminescent NCs with a wide range of compositions.[8] Research on lead halide perovskite NCs has greatly expanded since then, with numerous efforts in refining the synthesis protocol, elucidating the underlying physics and surface chemistry of this class of materials, and utilizing perovskite NCs in various applications.

Structural and optical properties

In a typical cubic ABX_3 perovskite crystal, the unit cell comprises eight corner-sharing $[BX_6]$ octahedra, situated at the vertices of the cell, while the center is occupied by the A^+ cation (Figure 1.1). The composition can vary greatly, especially A^+ can be an organic cation, such as methylammonium ($CH_3NH_2^+$, MA^+) or formamidinium ($CH(NH_2)_2^+$, FA^+), or an inorganic one such as Cs^+. However, to ensure the phase stability, the choice of A, B, and X is guided by t, also known as the Goldschmidt tolerance factor ($t = (r_A + r_X)/\sqrt{2}(r_B + r_X)$.[9] This factor is derived based on the relation between the edge length of the cubic lattice cell, which equals $2(r_B + r_X)$, and the cube's diagonal length, which is $2(r_A + r_X)$. Generally, the value of t for the perovskite structure lies in the range of 0.8 and 1.[10] The practical importance of this factor can be seen with $CsPbI_3$. Having a t value of 0.81, it is prone to change into a non-perovskite (yellow) phase at room temperature.[11]

While the above section discussed the perfectly cubic perovskite, the reality of the structure is often more complex and dynamic. Perovskite crystals can exist in several structures, most notably orthorhombic, tetragonal and cubic phases. Despite being the ideal structure, the cubic phase is formed only at elevated temperature (e.g. 130 °C for $CsPbBr_3$), making it rarely observed.[3] Interestingly, the majority of early studies of perovskite nanostructures concluded that the NCs adopted a cubic structure,[8, 13-14] and attributed the retention of this phase at ambient condition to high synthesis temperature and low surface energy.[8] However, phase identification with powder X-

ray diffraction is prone to misinterpretation when analyzing nanomaterials. As the dimensions of the material decrease, the peaks broaden, complicating the analysis of the diffractograms. Second, the difference between the perovskite phases is small, and can be obscured by the broadening. By using synchrotron X-ray scattering combined with Rietveld refinement and pair distribution function analyses, the correct phase of $CsPbBr_3$ NCs at room temperature was determined to be in fact orthorhombic.[12] Octahedral tilting in the perovskite structure is also noteworthy, which occurs when the BX_6 octahedra rotate slightly along their Cartesian axis/axes, while keeping the corner-sharing properties. As a result, the X-B-X bond angle is modified, and the coordination around the A cation significantly changes (Figure 1b).

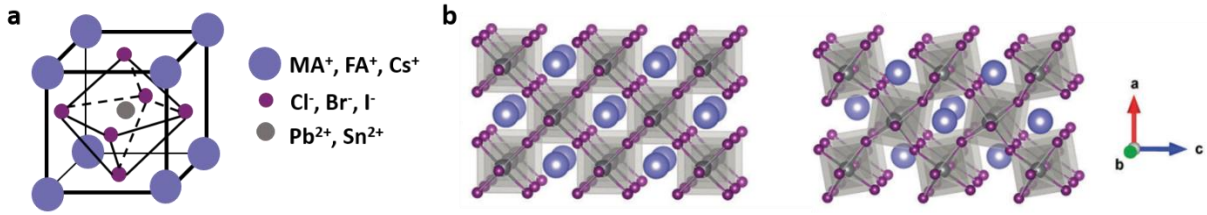

Figure 1.1. a) The crystal structure of halide perovskites, b) 3D cubic (left) and orthorhombic (right) structures. The figure was adapted from ref. [12].

The electronic structure of LHP is illustrated in Figure 1.2. The conduction band minimum (CBM) consists of Pb 6p - halide valence s and p antibonding states, while the valence band maximum (VBM) is dominated by antibonding halide p states, with minor contribution from Pb 6s states.[16] These features make the band gap very sensitive to the Pb–X bond. As such, by tuning the halide composition of LHP between pure and mixed halide, a wide emission range has been obtained.[8] Additionally, any change in the orbital overlap can shift the CBM and VBM accordingly. This is commonly observed in temperature dependent photoluminescence measurement of LHP NCs.[17-18] When the temperature is lowered, the crystal lattice contracts, leading to the increase in overlap between the orbitals of Pb and X. Since the nature of the VBM is antibonding, an increase in overlap will upshift it and decrease the overall band gap. Another source of overlap modification is the octahedral tilting of the perovskite structure.[19] In this case, the bending of the Pb-X-Pb bond decreases the overlap between the p orbitals, thus the band gap is increased.

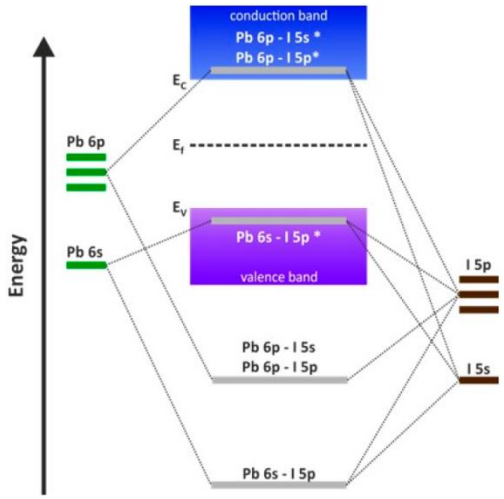

Figure 1.2. Scheme of electronic structure of lead iodide perovskite. The figure was adapted from ref. [15].

At the nanoscale, LHP exhibits properties that are quite different compared to conventional NCs. First of all, the degree of quantum confinement in $CsPbBr_3$ NCs is often only moderate. The Bohr radius of LHP (7 nm) is quite close to those of CdSe (5.3 nm) or CdTe (7.3 nm) NCsm.[8, 20] However, the most widely used synthetic procedures yield NCs with an average size of 8-12 nm, and only a few works managed to reach the strong confinement regime.[21] On the other hand, $MAPbX_3$ (X = Br, I) have much larger Bohr radii of ~20 nm, making it easier for them to display strong confinement.[22-23]

The second point of interest is the defect tolerance in LHP NCs. In general, due to their small size, NCs are comprised of a comparably small number of atoms. Compared to the bulk material, the presence of surface defects in NCs has a much more pronounced effect on the electronic structure, and subsequently, the optical properties. Cd and In-based NCs usually have very low photoluminescence quantum yield (PLQY) (<5%) due to the large number of defects within the band gap. It is necessary to fabricate a shell of a different material outside of these NCs, passivating the surface defects and increasing the QY of the NCs. This core/shell structure is often complex to realize due to the requirements of a low lattice mismatch between the core and the shell material and of an appropriate band alignment, and the high chemical sensitivity of LHP NCs.

Since the first syntheses of LHP NCs, it was found that the QY can reach very high values (>90%) without the need of a shell. This raised the possibility that the defect states in LHP are not deep in the band gap. Indeed, ab initio calculations performed on $CsPbBr_3$ have shown that most of the defects (interstitial defects, vacancies, and antisites) are shallow in nature, within 0.2 eV from the band maxima.[24] The few deep states have rather high formation energy, so their concentration in the NCs is negligible. In the case where defect sites actually quench the PL of the NCs, such as for $CsPbCl_3$ (initial QY <5%), these states can be easily passivated by post-synthetic surface treatment or by doping.[25-27] In hybrid perovskites, such as $MAPbI_3$, defect tolerance was also observed. In addition to the shallow defects being dominant,[28] the electronic structure remains robust even under compositional changes.[29] Under intense X-ray photoelectron irradiation, the ratio of I/Pb decreased to 2.5, with the formation of methylamine from MA^+, but the valence band structure was not affected.

Synthesis of lead halide perovskite nanocrystals

Currently, there are two main methods of LHP NCs synthesis: ligand-assisted reprecipitation (LARP) and hot-injection (HI). Reprecipitation of a metal salt happens when the dissolved salt experiences supersaturation, either by increasing its concentration, a change in temperature or a change in solvent polarity, typically realized by the addition of a 'bad' solvent with lower polarity than the current one. If this process is accompanied by suitable capping ligands, the size and shape of the precipitated salt can be controlled (hence the name ligand-assisted). The first LARP synthesis of LHP NCs was performed in 2015, resulting in $CH_3NH_3PbX_3$ (X = Cl, Br, I) NCs with QY up to 70%.[30] To precipitate the LHP NCs, a solution containing the precursors and long chain alkyl ligands in dimethylformamide ('good' solvent) was mixed with a weakly polar solvent (toluene, 'bad' solvent). The advantage of this synthetic route is the mild reaction condition (ambient air and room temperature) and simple process. Subsequent works focused on expanding the method to other compositions,[31-33] and improving the control over size and morphology of the NCs.[34-36] However, the high volume ratio of 'bad' to 'good' solvent limits the yield of the synthesis, and the rapid precipitation process makes it difficult to perfectly control the size distribution of the NCs.

The hot-injection (HI) method is a method originally developed to synthesize colloidal NCs of various compositions such as CdSe, InP.[37] In this method, a precursor dissolved either in a coordinating solvent or in a mixture of a non-coordinating solvent and ligands, is heated to an elevated temperature (typically 150-300 °C) before another precursor, at a lower or room temperature, is injected. Following the injection, the two precursors react and form small elementary units of the nanocrystal, the so-called nuclei. Due to a sudden drop of temperature in the flask induced by the injection, and the rapid decrease of the supersaturation due to the nucleation burst, in the following stage (ideally) only growth from solution takes place without the generation of new nuclei. In this reaction scheme, the nucleation and growth steps are thus effectively separated, which is considered a prerequisite for obtaining a narrow size distribution. In the case of a coordinating solvent (e.g., trioctylphosphine oxide, oleylamine, dodecanethiol), the latter also acts as a ligand, regulating the growth rate of the NCs, and passivating the surface of the particles. Many recent examples of the HI synthesis are using a non-coordinating solvent such as 1-octadecene (ODE) in conjunction with ligand(s) to decouple both roles.[38] This method allows the ligand concentration and nature to be varied in a wide range, which is impossible to achieve using a coordinating solvent. The concentration of the ligands can tune the reactivity of the monomers during the nucleation and growth steps. Therefore, by the careful control of the ligand concentration, small NCs (2-3 nm) with narrow size dispersion can be obtained.[38]

In 2015, Protesecu et al. were the first to report a HI synthetic route to obtain $CsPbX_3$ NCs of low size distribution.[8] However, the HI synthesis of $CsPbX_3$ NCs bears certain differences compared to that of conventional compounds such as cadmium or lead chalcogenide QDs. First of all, a separation between nucleation and growth cannot be observed due to the fast reaction kinetic. Furthermore, the temperature difference between the two precursors at the time of injection is usually less than 100 ^oC, making the temperature drop in the reaction flask rather negligible. Thus, the reaction is often stopped after only a few seconds, and in some cases just after the injection, by using an ice bath.[39] The resulting NCs, though monodisperse, usually have sizes larger than the excitonic Bohr radius (5-12 nm),[15] and tuning of the size is not easily realized.

Second, as $CsPbX_3$ is an ionic compound, the interactions with the ligands and the solvent are different. In the common synthesis, a non-coordinating solvent (ODE) is used, with oleic acid and oleylamine acting as ligands. In the reaction flask, the two ligands undergo acid-base reaction, forming $R_1\text{-}NH_3^+$ and $R_2\text{-}COO^-$ species, solubilizing the precursors and passivating the ionic surface of $CsPbX_3$. As such, the equilibrium of this acid-base reaction is the foundation of the stability of the ligand shell of $CsPbX_3$, as when the reaction is shifted to the reactant side, the ligands readily desorb from the NCs surface.[40] In contrary to the synthesis of metal chalcogenide NCs, the possibility of using a coordinating solvent has not been considered in the HI synthesis. Due to its nature, $CsPbX_3$ prefers ionic to covalent ligands, and the same can be applied to solvent. Therefore, polar organic solvents such as dimethylformamide can be used as coordinating solvents. However, they are not expected to be good passivating ligands because they are small and unbranched molecules. Additionally, their use, at least in the scope of ligand assisted re-precipitation synthesis, proves to be detrimental. Zhang et al. observed that for $MAPbI_3$, using coordinating solvents led to the formation of defective crystals, as the removal of strongly binding solvent molecules during the washing step created intrinsic iodine vacancies.[41]

Surface passivation

Before further discussion, the surface termination of $CsPbX_3$ NCs should be mentioned. There are two ways for the surface to be terminated (Figure 1.3). The first is called CsX termination, where the

$[PbX_6]^{4-}$ octahedra at the NCs surface remain intact, with Cs^+ and the X^- ions on top of the octahedra in direct contact with the ligands. In the other scenario, PbX_2 termination, the surface octahedra lose their top Br^- ion, resulting in a surface composed of planar X^- square and a Pb^{2+} ion with incomplete coordination sphere. Of the two possible surface terminations, the former appears to be more probable as the latter introduces a higher distortion to the $[PbX_6]^{4-}$ octahedra. This termination is supported by both DFT calculations,[42] and recently by solid-state NMR measurements.[43] These studies agree that when used as a ligand, alkylammonium cations substitute Cs^+ cations on the surface, while Pb^{2+} cations are stabilized by alkylammonium bromide. Passivation by oleate anions was also assumed, but this idea was disputed by De Roo et al. from the lack of interaction between oleic acid and the surface in the NMR spectra.[44] Instead, they proposed oleylammonium oleate as the ligand.

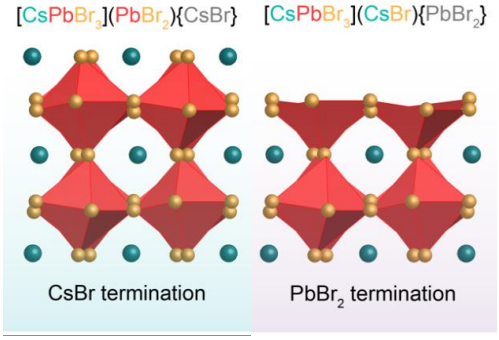

Figure 1.3. Illustration of different possible surface termination of $CsPbX_3$ NCs. The figure was adapted from ref. [43].

Ligand passivation

As discussed above, the most common ligand system for $CsPbX_3$ are oleylamine and oleic acid, or more precisely, their conjugated acid and base:

$$C_{18}H_{35}NH_2 \; + \; C_{17}H_{33}COOH \; \rightleftharpoons C_{18}H_{35}NH_3^{\,+} + \; C_{17}H_{33}COO^- \qquad \textbf{(Eq 1.1)}$$

However, the equilibrium only favors the conjugated species at low temperature. Because of this, the precursors usually precipitate from the solution upon heating to 200 °C, limiting the temperature of the synthesis. Moreover, during the washing process, the equilibrium can also shift back to the neutral molecules, destroying the ligand shell around $CsPbX_3$ NCs.

Thus, efforts have been made to shift the equilibrium to the conjugated species during synthesis. The simplest method is to add more ligands to the precursor solution.[40] In this way, the solubilization of the precursors can be achieved even at a temperature as high as 290 °C. However, it also encourages Ostwald ripening, as evidenced by the increasing size distribution with increasing ligand concentration. Ostwald ripening is observed in many colloidal syntheses and consists of the dissolution of the smallest particles in an ensemble, driven by their higher surface energy, and deposition of the dissolved matter on larger particles. As a result, Ostwald ripening leads to an increase of the mean size and a decrease of the particle concentration. Moreover, the size distribution after the ripening process is generally at least 15-20%, therefore, the reaction is generally stopped before reaching this regime. Additionally, a large excess of ligands can solubilize PbX_2 from the $CsPbX_3$ structure, resulting in 0D Cs_4PbX_6. Therefore, by tuning the ligand concentration and synthesis temperature, $CsPbBr_3$ NCs with size ranging from 4 to 16.4 nm could be obtained. Another method is to introduce other reactants into the equilibrium, as demonstrated by Thapa et al.[45] By using molecular bromine as the sole halide

source, they were able to change the behavior of the oleylamine/oleic acid (OLA/OA) system at high temperature (200 °C). Upon its introduction, Br_2 was reduced to HBr *in-situ* by the amine, which helped stabilizing the ammonium cations at high temperature. The synthesized $CsPbBr_3$ NCs possessed a lead halide rich surface with tightly bound ammonium ions, and were stable for at least 60 days under exposure to ambient air (relative humidity 50-60%).

Besides oleylamine and oleic acid, other ligands have been explored for the synthesis of $CsPbX_3$ NCs. One such ligand is aforementioned trioctylphosphine oxide (TOPO), which has been used extensively for the synthesis of CdSe NCs. Wu et al. added TOPO during the synthesis and without increasing the OLA and OA concentration, they could synthesize 14.8 nm $CsPbBr_3$ NCs at a temperature as high as 260 °C.[46] Furthermore, TOPO can completely replace OLA.[47] In this case, the solubilization of the $PbBr_2$ precursor can be handled by TOPO alone, by virtue of coordination. However, the TOPO/OA (Lewis) acid-base system still shares the same problem with the OLA/OA system: the acid-base reaction shift to the reactant side at high temperature. Furthermore, despite the observed coordination between TOPO and $PbBr_2$, no phosphorus signal was obtained on the surface of the $CsPbBr_3$ NCs, the only ligand was Cs-oleate. Another ligand closely related to TOPO is trioctylphosphine (TOP). With the absence of the oxygen atom, TOP is a soft base,[48] thus being a more favorable ligand for the soft acid Pb^{2+} than ammonium ligands. By adding TOP into the Cs-oleate injection solution, the obtained NCs showed higher stability both in ambient air and in polar solvents. Additionally, TOP can be added during a post-synthesis treatment, preserving both the colloidal stability and PLQY of the NCs after storage under ambient condition for more than 20 days.[49]

In the above works, OLA and OA are still present during the synthesis as primary ligands, meaning that the ligand chemistry still revolves around this acid-base equilibrium. Recently, some works have started to move away from this equilibrium. One of the challenges in this route is to find ligands that can also solubilize the metal precursors. Such a difficulty was demonstrated when alkylphosphonic acid was used as the only ligand.[50] For the lead acetate precursor to be completely solubilized, a pre-heating step at 220 °C was performed before the reaction step at 160 °C, which can compromise the synthesis scheme when scaled up. Aside from this disadvantage, this route could produce $CsPbBr_3$ NCs with sizes from 7 to 16.7 nm by changing the length of the alkyl chain. ^{31}P NMR and DFT analyses showed that phosphonic acid anhydride and phosphonate groups bound preferably to Pb^{2+} sites, passivating the surface (Fig. 1.4). It was also due to this preference that the synthesized NCs had a truncated octahedron shape instead of a cubic one.

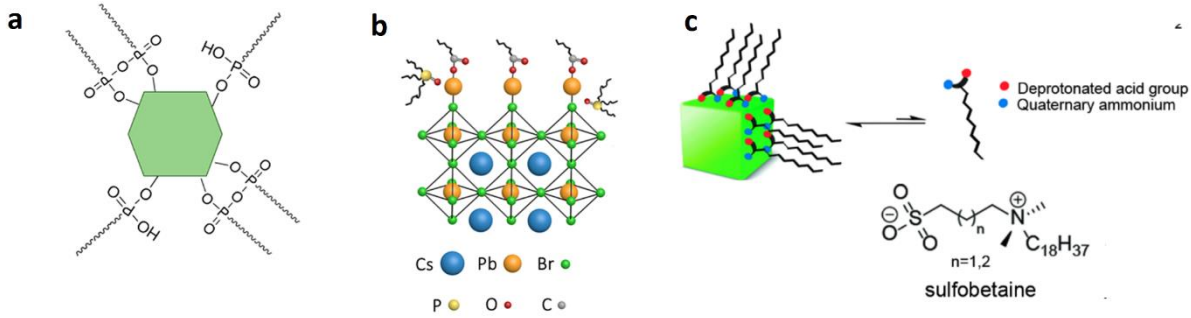

Figure 1.4. Different ligands for $CsPbX_3$ NCs: alkylphosphonic acid (a), lead stearate and TOPO (b), and zwitterionic molecules (c). The figure was adapted from refs. [50-52].

Further distancing from the use of acids, which involves protons, Liu et al. have proposed an amine- and acid-free synthetic route.[51] TOP was used to solubilize the $PbBr_2$ precursor, and no pre-heating step was required. The ligand for this synthesis came from lead stearate ($Pb(St)_2$). After being injected, $Pb(St)_2$ reacted with TOP to form TOP-St and –PbSt species, the latter acting as the primary ligand, realizing a carboxylate passivation without the direct use of acid. The NCs synthesized by this method demonstrated a high colloidal stability comparable to CdSe NCs after being washed twice with ethanol and nearly no fluorescent quenching after 30 days upon dispersion in ethanol. Adhering to the ionic nature of $CsPbX_3$, zwitterionic molecules containing both a dimethylammonium and a sulfonate head group have been used to replace both the amine and acid as ligand.[52] Despite its bulky nature, the dimethylammonium group could still fit in a cation site on the surface, as shown by DFT calculation. The calculation also showed no energetic difference between the conventional and zwitterionic passivation. However, by the chelate effect, the ligand favors binding to the surface, improving the stability of the NCs during the washing process with various antisolvents such as acetone and ethanol.

Core/shell structure

Another widely explored method of passivation of $CsPbX_3$ NCs is by encapsulating them with a shell of a different material, creating a core/shell structure. Compared to embedding NCs into glass or polymer matrices,[53-54] this method offers protection on a single particle level, making it suitable for applications where each NC is studied separately, such as bioimaging or single photon sources.[55-56] In the case of the conventional II-VI or III-V compounds, a crucial requirement for the shell material is to have the same crystal structure and low lattice mismatch compared to the core material.[57] This is to ensure that there is no strain or defect formation at the interface between the core and the shell. However, it is difficult to find such shell candidates in the case of $CsPbBrX_3$, as the materials in the perovskite family tends to be ionic, an already not favorable trait in terms of stability. Furthermore, possible anion exchange between the core and shell materials can make the situation even more complicated. Nonetheless, there has been reports on the synthesis of $CsPbBr_3$ NCs shelled by a layer of amorphous $CsPbBr_x$,[58] improving the PLQY of the NCs. Among materials with the same chemical make-up but different crystal structures, hexagonal Cs_4PbBr_6 has been shown to be a good candidate due to the low lattice mismatch.[59] $CsPbBr_3/Cs_4PbBr_6$ core/shell NCs have been successfully synthesized by rapidly switching from the formation of $CsPbBr_3$ to Cs_4PbBr_6 during the core synthesis.[60] With a larger band gap than the core, Cs_4PbBr_6 helped increase the QY of the system.

Compared to the case of II-VI or III-V core/shell NCs, the search for a shell materials for $CsPbX_3$ extends beyond those with compatible crystal structure and lattice parameters. Aside from the abovementioned difficulty in finding a satisfactory material with perovskite structure, the major reason a shell is sought for the $CsPbX_3$ core is to protect it from environmental degradation. For this purpose, materials such as oxides or binary semiconductors have been explored.

Early examples of perovskite/semiconductor core/shell structures come from two works in 2019 where a CdS shell was grown on $CsPbBr_3$ core NCs during synthesis.[61-62] In both cases, the size of the NCs increased from 12.7 – 14.6 nm (core NCs) to 21.3 – 22.1 nm (core/shell NCs), and the shell thickness was estimated to be ~2.5 nm.[62] Interestingly, the emission of the core/shell NCs blue-shifted compared to the core NCs. It was speculated that the diffusion of Cd^{2+} into $CsPbBr_3$ lattice led to this shifted emission, as similar behavior was also observed for other systems, such as CdZnS/ZnS core/shell or doped $CsPbBr_3$ NCs.[63-64] In addition to being more resistant against humidity, the $CsPbBr_3$/CdS NCs displayed nonblinking behavior, which attested to the surface passivation provided

by the CdS shell. This is explained by the strong chemical bonding between the core and the shell through S atoms, as evidenced by density of states calculations.[62] In another setup separating core and core/shell NCs syntheses, $CsPbBr_3$/ZnS NCs were fabricated.[65-66] The key of this route was enhancing the temperature stability of the core NCs for the long shell growth at high temperature, which was accomplished by treating their surface with oleylamine bromide at high temperature.[65, 67] The resulting NCs displayed a large size (average 49 nm), with an inhomogenously grown shell of a few nm in thickness. Despite this, the shell improved the stability of the NCs film in water and increased the PL lifetime due to the type II band alignment between $CsPbBr_3$ and ZnS.

The group of Li et al. fabricated a $CsPbBr_3$@TiO_2 structure by encapsulating the colloidal NCs with a TiO_2 precursor before calcinating the mixture at 300 °C.[68] The system could retain 80% of the initial QY after 12 weeks of immersion in water. Additionally, $CsPbBr_3$ NCs can undergo post-synthetic ligand exchange before the shell formation.[69] By exchanging the long-chain OLA and OA to α-amino butyric acid, a pronounced decrease in NCs size was observed, leading to both a blue-shift and an enhancement in the PLQY. Afterwards, a mixture of NCs with these two different sizes was coated with TiO_2, protecting the system against moisture. However, this approach sees some drawbacks in terms of structure and performance. First, core/shell structures at the single-particle level could not be achieved. Furthermore, most of the PLQY was sacrificed in the process. The reason was that with TiO_2 as the shell, a type II core/shell system was generated, where excited electrons from the core could delocalize into the shell, decreasing the PL. To solve the problem of single particle passivation, Zhong et al. have utilized an one-pot approach with SiO_2 as the shell material.[70] The synthesized material showed a PLQY of 90% and could retain structural integrity after 4 weeks at 75% humidity. By the same method, Sn-doped $CsPbBr_3$ NCs encapsulated with SiO_2 shell have been prepared, which displayed enhanced water stability and solubility when dispersed in an 1/4 v/v mixture of water and toluene.[71] An unconventional core/shell structure has recently been reported where $CsPbBr_3$ NCs were anchored to the inside of double-layer SiO_2 nanospheres acting as the shell (Figure 1.5).[72] This system exhibited improved UV and heat tolerance, retaining nearly 90% QY after 72 h of continuous UV irradiation and 65% after treatment at 100 °C.

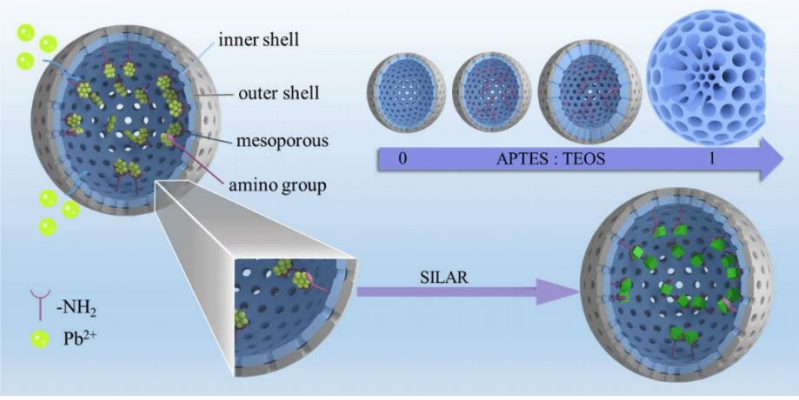

Figure 1.5. Demonstration of the $CsPbBr_3$/dual-shell hollow nanospheres system. The figure was adapted from ref. [72].

Due to the involvement of water during the shelling reaction for some inorganic oxide shells, a pre-protection strategy has been proposed, wherein the NCs are first modified before being subjected to the shelling process.[73] Doping Na^+ into the $CsPbBr_3$ structure was shown to enhance the stability of the core NCs, as evidenced by the suppressed Pb^0 nanoparticles formation during TEM measurement.

Afterwards, the particles were coated by an Al_2O_3 shell, improving their environmental stability. When dispersed in water and under ultrasonication, the QY remained nearly unchanged after 40 minutes whereas the signal of the unprotected core was almost quenched. Another approach to making the core/shell structure for $CsPbX_3$ is to synthesize the core in an organic solvent. By a sol-gel method, zinc acetate was converted into ZnO shell in the presence of LiOH in hexane.[74] Compared to the other routes, the particle size from this method greatly increased after the shelling reaction due to the high temperature (>69 °C) of the reaction facilitating thermal ripening. Nonetheless, the core/shell NCs displayed higher resistance to polar solvents.

Single photon emitters

Quantum information and photons

The idea of applying quantum mechanics to computation was discussed as early as 1980,[75] and it took 18 years for the first calculations to be carried out on a quantum computer.[76] Since then, this field of research has seen an exponential growth. As with the case of a classical computer where the working unit is a binary digit (bit), the analogue for the quantum computer is the qubit, a two-state quantum mechanical system. However, the quantum nature of the qubit allows it to be represented by a linear combination of these two states, increasing the number of possible states for certain computations compared to a bit. Furthermore, by superposition of multiple qubits, the number of states increases exponentially. Finally, any measurement (observation) done on the qubit would destroy this superposition state, similar to the example of Schrödinger's cat. This effect has a strong implication for the security of quantum communication, where an eavesdropper could be detected immediately due to this destruction.

There are many types of qubits based on different physical systems, such as ion traps or superconducting charges. Among them, the photon is an excellent choice for many applications. First of all, the propagation of photons is very fast (at the speed of light) and with little loss, and second, the current level of technology allows us a great degree of control over the properties of photons. For quantum computing and communication, single photons are often used, and the systems used to generate these single photons are single atoms/molecules, or single quantum dots, collectively named single photon emitters.[77]

Characteristics of single photon emitters

A single photon source is first and foremost characterized by the purity of the single photons it produces, or in other words, the probability that the emitted light from it contains one and only one photon. In the case of an ideal classical source (coherent source), the light can be represented by an electromagnetic field with constant amplitude, phase, and frequency. The number of photons follows a Poissonian distribution, and the probability of finding *m* photons is

$$p_m = \frac{\langle n \rangle^m}{m!} e^{-\langle n \rangle} \qquad \text{(Eq. 1.1)}$$

with $\langle n \rangle$ being the average number of photons. The standard deviation is $\Delta n = \sqrt{\langle n \rangle}$. This is the situation of a laser source. Deviated from this ideal picture is the thermal light, in which photons have different intensities due to phase variation. The number of photons is expressed by the Bose-Einstein distribution for black body radiation:

$$p_m = \frac{\langle n \rangle^m}{(1+\langle n \rangle)^{m+1}} \qquad \text{(Eq. 1.2)}$$

Figure 1.6 depicts the probability distributions for coherent and thermal sources, with $\langle n \rangle = 1$ (single photon) in comparison with a single photon source. In the former two cases, it can be seen that the chance of emitting more than 1 photon is not negligible, and in addition, at least 33% of the time, no photon is emitted.

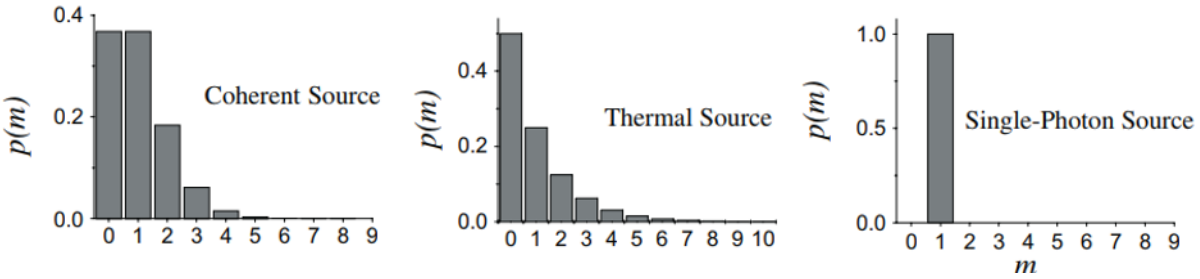

Figure 1.6. Probability distributions for different light sources. The figure is reproduced from ref. [78].

To improve these sources, a sufficiently long delay between the emission events must be introduced. This idea was realized for the first time with the fluorescence of a sodium atom beam excited by a continuous laser.[79] Due to the beam setup, only one atom may cross the laser beam and get excited at a time. By tuning the laser's power and the atoms' energy level, only one optical transition was possible. Coupled with the atomic beam setup, only the emission of single atoms was recorded. The resulting probability distribution exhibited sub-Poissonian statistics, where $\Delta n < \sqrt{\langle n \rangle}$ (Figure 1.6, right panel). This behavior where photons are emitted one by one is called antibunching.

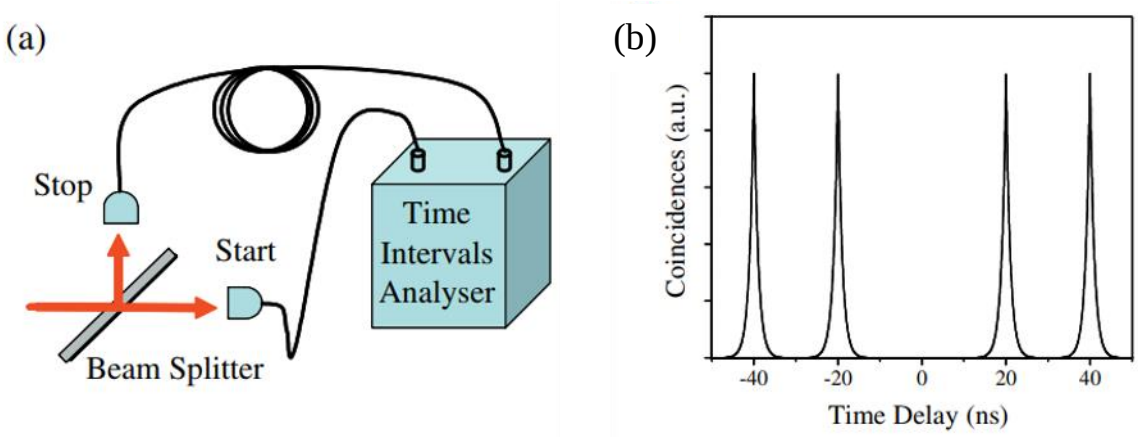

Figure 1.7. a) Illustration of the Hanbury Brown-Twiss setup, b) Second-order correlation function for a pulsed excitation. The figures are reproduced from ref. [78]

In practice, the detection of antibunching is limited by the detector's dead time. This dead time is the duration after a detection event where the detector cannot function, and can last for several nanoseconds. Hanbury Brown and Twiss found a way to circumvent this limitation by employing simultaneously two detectors.[80-81] As depicted in Figure 1.7a, the Hanbury Brown-Twiss (HBT) setup consists of a 50/50 beam splitter and two detectors. The reflected and transmitted incident lights from the photon source enter each of these detectors, and the signals they generate are characterized by a correlation function. In optics, this function is used to determine whether two waves are coherent. The first-order function, $g^{(1)}$, relates to the amplitude of the waves, while the second-order $g^{(2)}$, which is calculated in this experiment, relates to the intensity. Therefore, for coherent light, $g^{(2)}(t) = 1$. For

antibunched photons, at t = 0, since there is only one photon entering one of the detectors, $g^{(2)}(0) = 0$. This is illustrated in Figure 1.7b, in which a single photon emitter is excited by a pulsed laser. The peaks appearing at t > 0 are caused by the correlation function of the pulse excitation, which has the shape of a Dirac comb.

The other important characteristic is the indistinguishability of the emitted photons. Ideally, photons produced by a source with two energy states are indistinguishable. However, energy fluctuation of these states can slightly alter the energy of the electronic transition and thus, the energy of the photons. Two types of fluctuation are discussed in the literature, namely dephasing and spectral diffusion. Dephasing, as the name suggests, is the loss of phase correlation between two photons due to a sudden and weak perturbation in the transition energy states. It is often caused by random collision events between the emitters and the environment. On the other hand, spectral diffusion is the result of interaction between the transition states and the local environment. Hence, the fluctuation in transition energy is stronger and lasts longer than in the case of dephasing. In fields such as quantum computation, it is crucial to maintain photon indistinguishability, whereas it is less so for quantum cryptography.

Photon indistinguishability is studied by a two-photon interference experiment. In a typical setup called a Hong-Ou-Mandel interferometer, two photons 1 and 2 pass through a beam splitter from different sides before being detected by detectors a and b (Figure 1.8a).[82] There are four possibilities for detecting the photons, for example, photon 1 enters detector a. If these two photons are identical, the two detection events where each photon enters a separate detector become completely similar in nature. When the probabilities of these two events are calculated, they are equal in magnitude but have opposite signs due to the Bose-Einstein commutation properties.[83] Therefore, they cancel each other out, or in other words, interfere destructively. The only observable events are when the two photons enter the same detector. Correlation between the two detectors will result in $g^{(2)} = 0$, represented by a dip in the coincidence count as a function of the beam splitter position (Figure 1.8b). In case of dephasing, the magnitude of the dip will be reduced:

$$g^{(2)} = 1 - \frac{T_2}{2T_1} \qquad \text{(Eq. 1.3)}$$

where T_1 and T_2 are the excited state lifetime and coherence time, respectively.[84] In the case of spectral diffusion, the emission linewidth is broadened and if the time interval between the two photons is larger than the spectral diffusion time, their energies would be so different that interference is impossible. The effect of spectral diffusion can be offset by reducing the delay between the two photons arriving at the beam splitter.[85]

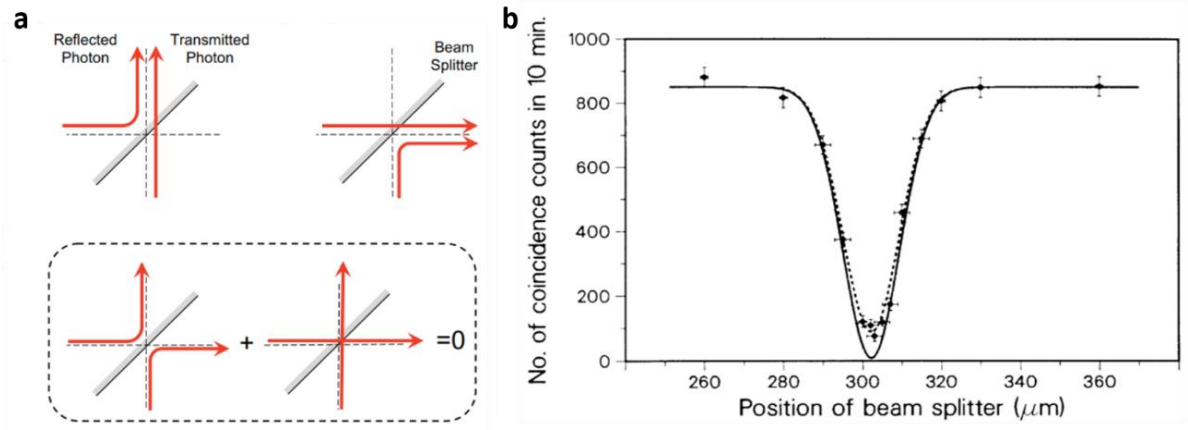

Figure 1.8. a) Illustration of the Hong-Ou-Mandel setup, b) Number of coincidence counts as a function of beam splitter displacement, measured (dashed) and theoretical (solid) curves. The figures are reproduced from refs. [78] and [82].

Examples of single photon emitters

Over the years, many systems have been investigated as single photon emitters. The manner in which they emit photons can either be probabilistic, or deterministic (on-demand). Probabilistic emitters rely on creating a pair of photons through the parametric down-conversion process.[86-88] One of the photons is used to signal the arrival of the other, and this method is called heralding. Deterministic sources, on the other hand, are usually two-level systems. For the purpose of this thesis, deterministic sources will be the focus of the discussion.

To generate single photons in an efficient manner, the emitter has to satisfy several requirements: it should be a deterministic emitter, the emission rate has to be fast, and the photons emitted have to be indistinguishable. $CsPbBr_3$ NCs automatically qualify for the first one due to the nature of their light emission. The radiative decay time of single $CsPbBr_3$ NCs was found to be ~6.4 ns at room temperature.[89] Compared to other types of NCs such as InP/ZnSe (17.5 ns) or CdSe/CdZnS (29 ns), the decay time of $CsPbB_3$ is considerably lower, which would enable faster photon emission.[90-91] This value improves when the NCs are cooled down to cryogenic temperature, reaching 0.2 – 0.28 ns.[92-93] The indistinguishability of emitted photons from $CsPbBr_3$ NCs was assessed by two-photon correlation measurements, which yield ~150 fs of coherence time at room temperature and 50 - 78 ps at 4K.[93-94] Compared to the state-of-the-art value of > 1.5 μs at 4 K with MBE-grown InGaAs,[95] the result achieved for $CsPbBr_3$ NCs is modest. However, the advantages of easy fabrication as well as the optical properties and tunability of lead halide perovskites allow the material competitive edges in future developments.

Single photon nanoantenna

Single luminescent nanocrystals, by themselves, cannot be incorporated into optical devices as emitters. First, their emission rate is rather slow, indicated by the decay time in the order of nanoseconds, potentially limiting the device speed. Second, they emit light in all directions, which is undesirable in the operation of multiple emitter arrays. The former can be addressed by coupling them with an optical cavity, whereas the latter requires a specific structure known as an antenna.

An optical cavity is a structure consisting of mirrors, which only allows certain electromagnetic modes to propagate. The cavity is often characterized by the mode volume and quality factor (Q). The quality factor describes the time the photon, and therefore the electromagnetic energy, is trapped inside the cavity. Since the energy decays with time, the decay rate is expressed as $\kappa = \frac{\omega}{2Q}$, with ω being the frequency of the photon. When an emitter is placed inside a cavity, it will give rise to a coupling between them, typically modeled as a dipole interaction between the dipole moment of the emitter and the electric field of the cavity. The maximum coupling parameter is then defined as

$$g_0 = \frac{\mu_{eg}}{\hbar}\sqrt{\frac{\hbar\omega}{2\varepsilon_0 V_{mode}}} \qquad \text{(Eq. 1.4)}$$

with μ_{eg}, ε_0, and V_{mode} being the dipole moment of the electronic transition, vacuum dielectric constant, and mode volume, respectively. In reality, if the emitter is not located at the maximum electric field density or if the dipole is not aligned with the field, the coupling parameter is reduced, and g is used instead of g_0. In the weak coupling regime ($\kappa > 2g$), the emission decay rate of the emitter has the expression $\frac{2|g|^2}{\kappa}$. As spontaneous emission is not an intrinsic property of the emitter, but rather the consequence of its interaction with the electromagnetic environment, the change in the electric

field density induced by the presence of the cavity can change the emission rate, even without strong coupling to the emitter. When the enhanced emission rate is compared to the value without the cavity (given by Einstein A coefficient), one obtains the Purcell factor:[96]

$$F = \frac{rate_{modified}}{rate_{without\ cavity}} = \frac{3}{4\pi^2}\left(\frac{\lambda}{n}\right)^3 \frac{Q}{V_{mode}} \qquad \text{(Eq. 1.5)}$$

where n is the refractive index of the medium surrounding the emitter, Q and V_{mode} are the quality factor and mode volume of the cavity, respectively. To optimize the Purcell factor, the cavity should be designed to maximize the quality factor and minimize the mode volume.

To control the direction of the electromagnetic wave, antennas have often been used. Originally developed for transmitting and receiving radio waves, these structures comprise conductors arranged in specific patterns and coupled to the emitting/receiving element. Antennas used for single photon emitters differ vastly from their traditional counterpart in two ways, the wavelength and the size. When the wavelength reduces from centimeters to nanometers, the assumption of a perfect conductor for a metal becomes invalid. Second, at the metal-insulator interface, plasmonic resonance can occur, which leads to a strong localization of the electric field in the nanoscale region inside the nanoantenna. This region provides the perfect cavity for single photon emitters, with small mode volume and directivity. Thus, by placing the emitter in the gap between plasmonic materials, a single photon nanoantenna can be realized where the emission can be accelerated and directed.

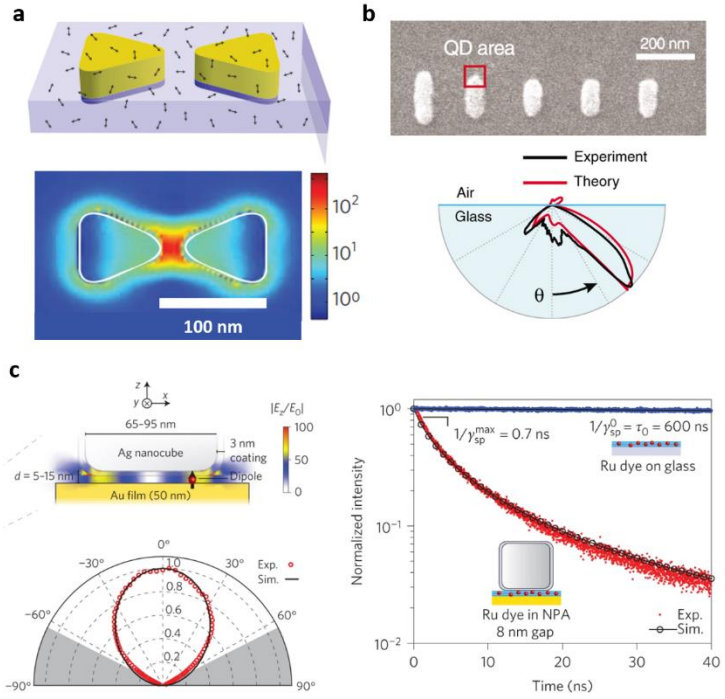

Figure 1.9. Different antenna configurations in the literature: a) Bowtie antenna (ref. [97]), b) Yagi-Uda antenna (ref. [98]), c) Nanopatch antenna (ref. [99]). In cases b and c, far-field emission diagrams illustrate the directivity of the emission.

In the literature, various antenna configurations were adapted to single photon nanoantenna. Among them, the bowtie antenna provides a good model system.[97] It consists of two gold triangles facing each other in the shape of a bowtie (Figure 1.9a), and the emitter is placed between the triangles.

Depending on the size of the gap, the emission rate for the single molecule could be enhanced by at most three orders of magnitude. However, this structure offers no directional control. It can be achieved with another system based on the Yagi-Uda antenna, as shown in Figure 1.9b.[98, 100] The emitter is placed at one of the ends of a gold nanorod, which ensures coupling with its dipole resonance. The electromagnetic wave from the emitter excites the nanorod where the emitter is located, which in turn excites the other rods of the array through dipole–dipole coupling. The distance between the rods, as well as their lengths, were optimized so that the collective radiation pattern is therefore directed along the path of the array. Despite the highly directional emission gained by this structure, the placement of the emitter does not allow the emission rate to benefit from any cavity. Therefore, the nanopatch antenna is proposed to achieve both the Purcell effect and directional control.[99, 101] Stemming from patch antenna, where the emitter is placed in the nano-sized gap between two metallic plates, the nanopatch antenna has one of the plates reduced its size to the order of nanometers (Figure 1.9c). The emission rate is enhanced due to the localized electric field density between the metals, while the small size of the metal patch only allows the effect to appear around it, and enhances the emitted light in the direction of the electric field between the two metals.

Diluted magnetic semiconductors

Diluted magnetic semiconductors (DMS) form a class of materials where a semiconductor compound is doped by magnetic elements, usually first-row transition metals. By this way, magnetic properties are introduced into the semiconductor, and the exchange interactions between charge carriers and dopants' spins results in various exciting effects such as the giant Zeeman effect or optically and electrically controlled ferromagnetism.[102] Such effects are essential in the development of spintronics, where spin-controlled charge transport can enhance the storage and transfer capacity of memory devices. Another example are spin-polarized light emitting diodes, where the incorporation of DMS instead of the undoped semiconductor allows the diode to emit circularly polarized light.[103] So far, the most studied materials are II-VI or III-V semiconductor compounds doped with Mn, and they will be the focus of discussion.

Electronic structure of DMS

As a 3d transition metal is doped into a semiconductor, its d levels can interact with the host's electronic bands in different ways. As the metal is doped by substitution, its d states are split by the crystal field into a doublet (d_{z^2} and $d_{x^2-y^2}$) and a triplet (d_{xy}, d_{yz}, and d_{xz}). The d_{xy}, d_{yz}, and d_{xz} levels can hybridize with the host's s and p bands, resulting in bonding and anti-bonding states denoted as t_b and t_a in Figure 1.10, respectively. On the other hand, the d_{z^2} and $d_{x^2-y^2}$ levels have little overlapping with the p levels and remain non-bonding (denoted as e). Second, the dopant is divalent whereas the host's cation can be either divalent (II-VI) or trivalent (III-V). In the latter case, a p-type semiconductor is realized by the doping, which has an effect on the position of the Fermi level. The relative position of the Fermi level to the d states in turn will determine the contribution of different exchange interactions to the final magnetic properties of the DMS.[104]

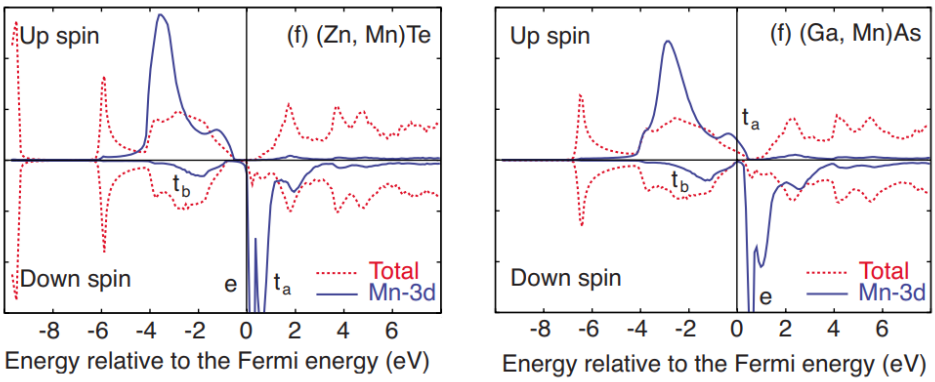

Figure 1.10. Calculated density of states of ZnTe (II-VI) and GaAs (III-V) doped with 5% Mn. The dotted lines show the average density of states (DOS) per unit cell, whereas the solid lines show the partial DOS per dopant atom at the Mn site. The figure was adapted from ref. [104]

For II-VI DMS, the dopant's d states such as t_a and e are localized within the band gap, and do not modify the semiconducting properties of the material under zero magnetic field (Figure 1.10). Due to the finite concentration of the dopant, the states broaden into bands. In III-V DMS however, the d states of the dopant can be found in the valence band. This is because the p states of five-valent anions in III-V compounds have higher energy than those of six-valent anion in II-VI compounds. As a consequence, the valence band of III-V compounds lies at higher energy and can encompass the d states of Mn. The relative energy level of the p state compared to the d states can affect the strength of hybridization as well as the position of the hybridized bonding state relative to the valence band maximum (which is also composed of the p state).

Exchange interactions in DMS

The exchange interaction in DMS can be between the d states from Mn and the host's states or between the spins of neighboring Mn dopants. The former is called sp-d exchange, and is often responsible for the ferromagnetic behavior of the system. The s-d exchange is a direct exchange of s and d electrons in the overlapping region of these orbitals. According to the Pauli exclusion principle, only electrons with antiparallel spins can participate in this exchange. Usually, the antiparallel configuration implies that the magnetic moments of these electrons are aligned in opposite directions. However, in some systems, the Landé g-factor for s and d electrons have opposite signs, causing the magnetic moments to have the same sign for antiparallel spins. Thus, the s-d exchange results in a ferromagnetic interaction. The p-d exchange is dominant in narrow-gap semiconductors, where d states are located in the valence band (Figure 1.11). In this case, hybridization with the host's p levels results in a bonding state with spin down and an antibonding state with spin up. Compared to the energy of the p states before hybridization, it can be considered that the spin-down state downshifts in energy, and vice versa for the spin-up state. The magnitude of these shifts is proportional to the p-d hybridization. The situation can be imagined as an effective magnetic field with the magnitude given by the difference between the spin up and down states, which aligns the dopant's spin antiparallel to that of the host.

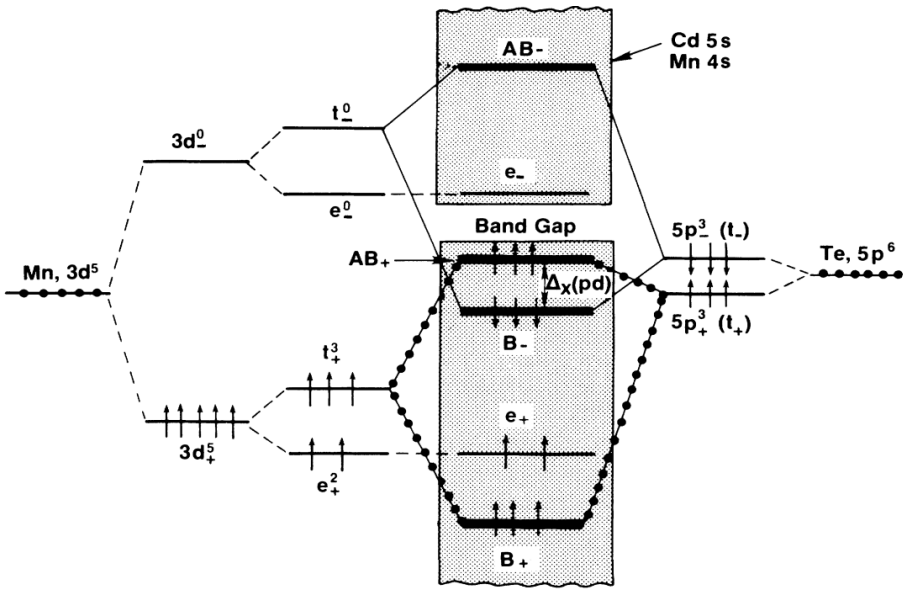

Figure 1.11. Schematic of p-d hybridization in Mn-doped CdTe. The figure was adapted from ref. [105]

The exchange interaction between the d states of the dopants does not occur through direct orbital hybridization, in contrary to dopant-host interaction. Instead, it is mediated by an anion bound to two dopant atoms (superexchange), by an electron travelling between the two dopant sites (double exchange), or by polarized carriers (Ruderman–Kittel–Kasuya–Yosida, RKKY). In the first case, electrons with antiparallel spins can delocalize on the anion, subsequently reducing the energy of the system. It is worth noting that since this is the interaction between d electrons, the resulting coupling is antiferromagnetic in nature. Double exchange was first proposed by Zener to explain the ferromagnetism in systems with mixed-valency.[106] In such systems, a virtual electron transfer can occur ($d^5 - d^4$ to $d^4 - d^5$), which does not cost energy if the spin of the dopants are parallel. In DMS, acceptor or donor doping can allow dopant ions to have multiple charged states, making double exchange a relevant interaction. In contrast to the previous exchange interactions which occur only in insulators, RKKY exchange is very efficient for semiconductors with a high density of charge carriers. The reason is that in this exchange, the magnetic moment of a Mn^{2+} ion polarizes the spin of the carrier, which in turn couples with another Mn^{2+}. This exchange results in ferromagnetic behavior at short distance, typically for the nearest neighbors. For dopant ions further apart, the exchange alternates between being ferromagnetic and antiferromagnetic.

Optical properties of DMS

The most important feature of DMS is the giant Zeeman effect. In quantum mechanics, the Zeeman effect is the splitting of the energy levels of the system under an external magnetic field by orienting the spins of electrons either parallel or antiparallel to its direction. The magnitude of the splitting is proportional to the magnetic field, and for n-type CdTe, it's approximately 4 meV at 2 T.[107] In DMS, the sp-d exchange interactions act as another magnetic field which scales with the magnetization of Mn^{2+}. This magnetic field can contribute to enhance the Zeeman effect, and for $Zn_{1-x}Mn_xSe$, the splitting can be as high as 100 meV at a few T.[108]

A consequence of the giant Zeeman effect is that the light emission becomes circularly polarized. In the classical view, light is considered as an electromagnetic wave propagating in a perpendicular direction to oscillating electric and magnetic fields. The polarization of the wave is determined by the

direction of the electric field. In the quantum mechanical view, the polarization of a photon is determined by its spin. For spin values of ±1, the photon has left (σ^+) and right (σ^-) circular polarizations, respectively. In DMS, energy levels with different total momentums are split, and transitions between states where the difference in total momentum is ±1 would involve photons in either σ^+ or σ^- polarizations. Figure 1.12 plots the scheme of band-to-band transitions, as well as the observed energy splitting associated with them. As can be seen, transitions involving different polarizations can be distinguished based on the energy shift. Furthermore, by extracting the spin polarized holes and have them recombine with non-polarized electrons at the interface of a p-n junction, only σ^+ polarized light is emitted.[109] This is the basis of a spin-polarized light-emitting diode.

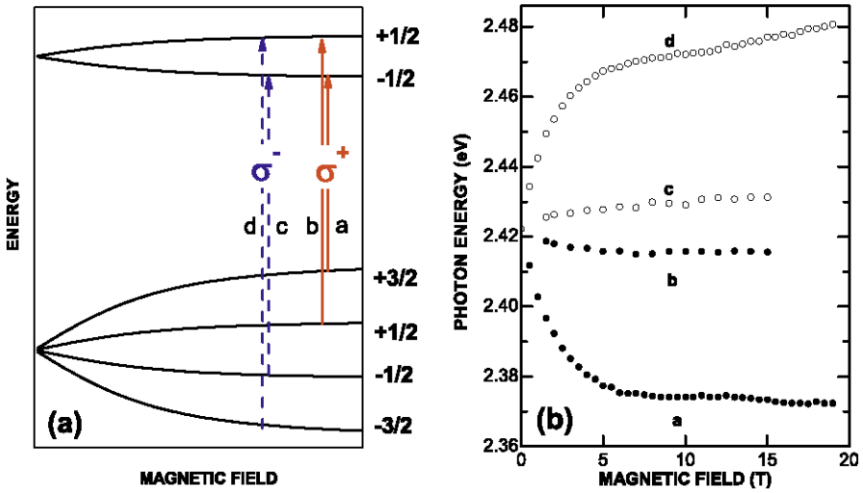

Figure 1.12. a) Scheme of band-to-band transitions with their respective polarizations. The spin states of charge carriers are denoted on the right. b) Observed energy splitting of the associated transitions in $Zn_{0.95}Mn_{0.05}Te$. The figure was reproduced from refs. [102].

Another important property of DMS is carrier-induced ferromagnetism, which is realized by RKKY exchange. As the carriers are polarized by the dopant's spins by the giant Zeeman effect, they can also polarize the spins. This mutual interaction results in the dependence of the magnetic behavior on the magnetic susceptibilities of the carriers χ_c and the dopant χ_d. Physically, when minimal energy is required to align the dopant's and carrier spins (large χ_d and χ_c), the system tends to stabilize in the ordered, ferromagnetic phase. The key to control the magnetic behavior in DMS by χ_c is through varying the carrier density. This can be easily accomplished by applying an electric field or illumination. Increasing the free carrier density allows more carrier-carrier exchange interactions, thus enhancing χ_c. In addition, some semiconductors feature both light and heavy holes as charge carriers with different spin directions. For a classical sample grown by molecular beam epitaxy, the relative lattice mismatch between the substrate and the sample induces compressive or tensile strains, resulting in heavy and light holes, respectively. The spin values of these different types of holes are anisotropic, being ±1/2 in the direction normal to the sample for heavy holes and in in-plane directions for light holes. Thus, the Curie-Weiss behavior depends on different directions of the applied magnetic field. This allows for more opportunities in tuning the magnetic response of the DMS.

References

1. Wells, H. L., Über die cäsium-und kalium-bleihalogenide. *Zeitschrift für anorganische Chemie* **1893,** *3* (1), 195-210.
2. Møller, C. K., A Phase Transition in Cæsium Plumbochloride. *Nature* **1957,** *180* (4593), 981-982.
3. Møller, C. K., Crystal Structure and Photoconductivity of Cæsium Plumbohalides. *Nature* **1958,** *182* (4647), 1436-1436.
4. Kojima, A.; Teshima, K.; Shirai, Y.; Miyasaka, T., Organometal halide perovskites as visible-light sensitizers for photovoltaic cells. *J. Am. Chem. Soc.* **2009,** *131* (17), 6050-1.
5. Kim, H. S.; Lee, C. R.; Im, J. H.; Lee, K. B.; Moehl, T.; Marchioro, A.; Moon, S. J.; Humphry-Baker, R.; Yum, J. H.; Moser, J. E.; Gratzel, M.; Park, N. G., Lead iodide perovskite sensitized all-solid-state submicron thin film mesoscopic solar cell with efficiency exceeding 9%. *Scientific reports* **2012,** *2*, 591.
6. National Renewable Energy Laboratory. Best Research-Cell Efficiency Chart. https://www.nrel.gov/pv/cell-efficiency.html (accessed Dec 22, 2022).
7. Schmidt, L. C.; Pertegas, A.; Gonzalez-Carrero, S.; Malinkiewicz, O.; Agouram, S.; Minguez Espallargas, G.; Bolink, H. J.; Galian, R. E.; Perez-Prieto, J., Nontemplate synthesis of CH3NH3PbBr3 perovskite nanoparticles. *J. Am. Chem. Soc.* **2014,** *136* (3), 850-3.
8. Protesescu, L.; Yakunin, S.; Bodnarchuk, M. I.; Krieg, F.; Caputo, R.; Hendon, C. H.; Yang, R. X.; Walsh, A.; Kovalenko, M. V., Nanocrystals of Cesium Lead Halide Perovskites (CsPbX(3), X = Cl, Br, and I): Novel Optoelectronic Materials Showing Bright Emission with Wide Color Gamut. *Nano Lett.* **2015,** *15* (6), 3692-6.
9. Goldschmidt, V. M., Die gesetze der krystallochemie. *Naturwissenschaften* **1926,** *14* (21), 477-485.
10. Kieslich, G.; Sun, S.; Cheetham, A. K., An extended Tolerance Factor approach for organic-inorganic perovskites. *Chemical science* **2015,** *6* (6), 3430-3433.
11. Eperon, G. E.; Paternò, G. M.; Sutton, R. J.; Zampetti, A.; Haghighirad, A. A.; Cacialli, F.; Snaith, H. J., Inorganic caesium lead iodide perovskite solar cells. *Journal of Materials Chemistry A* **2015,** *3* (39), 19688-19695.
12. Cottingham, P.; Brutchey, R. L., On the crystal structure of colloidally prepared CsPbBr3 quantum dots. *Chem Commun (Camb)* **2016,** *52* (30), 5246-9.
13. Bekenstein, Y.; Koscher, B. A.; Eaton, S. W.; Yang, P.; Alivisatos, A. P., Highly Luminescent Colloidal Nanoplates of Perovskite Cesium Lead Halide and Their Oriented Assemblies. *J. Am. Chem. Soc.* **2015,** *137* (51), 16008-11.
14. Zhang, D.; Eaton, S. W.; Yu, Y.; Dou, L.; Yang, P., Solution-Phase Synthesis of Cesium Lead Halide Perovskite Nanowires. *J. Am. Chem. Soc.* **2015,** *137* (29), 9230-3.
15. Shamsi, J.; Urban, A. S.; Imran, M.; De Trizio, L.; Manna, L., Metal Halide Perovskite Nanocrystals: Synthesis, Post-Synthesis Modifications, and Their Optical Properties. *Chem. Rev.* **2019,** *119* (5), 3296-3348.
16. Umebayashi, T.; Asai, K.; Kondo, T.; Nakao, A., Electronic structures of lead iodide based low-dimensional crystals. *Physical Review B* **2003,** *67* (15).
17. Shinde, A.; Gahlaut, R.; Mahamuni, S., Low-Temperature Photoluminescence Studies of CsPbBr3 Quantum Dots. *The Journal of Physical Chemistry C* **2017,** *121* (27), 14872-14878.
18. Lee, S. M.; Moon, C. J.; Lim, H.; Lee, Y.; Choi, M. Y.; Bang, J., Temperature-Dependent Photoluminescence of Cesium Lead Halide Perovskite Quantum Dots: Splitting of the Photoluminescence Peaks of CsPbBr3 and CsPb(Br/I)3 Quantum Dots at Low Temperature. *The Journal of Physical Chemistry C* **2017,** *121* (46), 26054-26062.
19. Prasanna, R.; Gold-Parker, A.; Leijtens, T.; Conings, B.; Babayigit, A.; Boyen, H. G.; Toney, M. F.; McGehee, M. D., Band Gap Tuning via Lattice Contraction and Octahedral Tilting in Perovskite Materials for Photovoltaics. *J. Am. Chem. Soc.* **2017,** *139* (32), 11117-11124.
20. Mushonga, P.; Onani, M. O.; Madiehe, A. M.; Meyer, M., Indium Phosphide-Based Semiconductor Nanocrystals and Their Applications. *Journal of Nanomaterials* **2012,** *2012*, 1-11.
21. Akkerman, Q. A.; Nguyen, T. P. T.; Boehme, S. C.; Montanarella, F.; Dirin, D. N.; Wechsler, P.; Beiglbock, F.; Raino, G.; Erni, R.; Katan, C.; Even, J.; Kovalenko, M. V., Controlling the nucleation and growth kinetics of lead halide perovskite quantum dots. *Science* **2022,** *377* (6613), 1406-1412.
22. Hirasawa, M.; Ishihara, T.; Goto, T.; Uchida, K.; Miura, N., Magnetoabsorption of the lowest exciton in perovskite-type compound (CH3NH3)PbI3. *Physica B: Condensed Matter* **1994,** *201*, 427-430.

23. Koutselas, I.; Ducasse, L.; Papavassiliou, G. C., Electronic properties of three-and low-dimensional semiconducting materials with Pb halide and Sn halide units. *J. Phys.: Condens. Matter* **1996,** *8* (9), 1217.
24. Kang, J.; Wang, L. W., High Defect Tolerance in Lead Halide Perovskite CsPbBr3. *The journal of physical chemistry letters* **2017,** *8* (2), 489-493.
25. Nenon, D. P.; Pressler, K.; Kang, J.; Koscher, B. A.; Olshansky, J. H.; Osowiecki, W. T.; Koc, M. A.; Wang, L. W.; Alivisatos, A. P., Design Principles for Trap-Free CsPbX3 Nanocrystals: Enumerating and Eliminating Surface Halide Vacancies with Softer Lewis Bases. *J. Am. Chem. Soc.* **2018,** *140* (50), 17760-17772.
26. Ahmed, G. H.; El-Demellawi, J. K.; Yin, J.; Pan, J.; Velusamy, D. B.; Hedhili, M. N.; Alarousu, E.; Bakr, O. M.; Alshareef, H. N.; Mohammed, O. F., Giant Photoluminescence Enhancement in CsPbCl3 Perovskite Nanocrystals by Simultaneous Dual-Surface Passivation. *Acs Energy Lett* **2018,** *3* (10), 2301-2307.
27. Ahmed, T.; Seth, S.; Samanta, A., Boosting the Photoluminescence of CsPbX3 (X = Cl, Br, I) Perovskite Nanocrystals Covering a Wide Wavelength Range by Postsynthetic Treatment with Tetrafluoroborate Salts. *Chem. Mater.* **2018,** *30* (11), 3633-3637.
28. Yin, W.-J.; Shi, T.; Yan, Y., Unusual defect physics in CH3NH3PbI3 perovskite solar cell absorber. *Appl. Phys. Lett.* **2014,** *104* (6), 063903.
29. Steirer, K. X.; Schulz, P.; Teeter, G.; Stevanovic, V.; Yang, M.; Zhu, K.; Berry, J. J., Defect Tolerance in Methylammonium Lead Triiodide Perovskite. *Acs Energy Lett* **2016,** *1* (2), 360-366.
30. Zhang, F.; Zhong, H.; Chen, C.; Wu, X. G.; Hu, X.; Huang, H.; Han, J.; Zou, B.; Dong, Y., Brightly Luminescent and Color-Tunable Colloidal CH3NH3PbX3 (X = Br, I, Cl) Quantum Dots: Potential Alternatives for Display Technology. *ACS nano* **2015,** *9* (4), 4533-42.
31. Li, X.; Wu, Y.; Zhang, S.; Cai, B.; Gu, Y.; Song, J.; Zeng, H., CsPbX3 Quantum Dots for Lighting and Displays: Room-Temperature Synthesis, Photoluminescence Superiorities, Underlying Origins and White Light-Emitting Diodes. *Adv. Funct. Mater.* **2016,** *26* (15), 2435-2445.
32. Weidman, M. C.; Seitz, M.; Stranks, S. D.; Tisdale, W. A., Highly Tunable Colloidal Perovskite Nanoplatelets through Variable Cation, Metal, and Halide Composition. *ACS nano* **2016,** *10* (8), 7830-9.
33. Xu, B.; Wang, W.; Zhang, X.; Cao, W.; Wu, D.; Liu, S.; Dai, H.; Chen, S.; Wang, K.; Sun, X., Bright and efficient light-emitting diodes based on MA/Cs double cation perovskite nanocrystals. *Journal of Materials Chemistry C* **2017,** *5* (25), 6123-6128.
34. Seth, S.; Samanta, A., A Facile Methodology for Engineering the Morphology of CsPbX3 Perovskite Nanocrystals under Ambient Condition. *Scientific reports* **2016,** *6*, 37693.
35. Cho, J.; Choi, Y.-H.; O'Loughlin, T. E.; De Jesus, L.; Banerjee, S., Ligand-Mediated Modulation of Layer Thicknesses of Perovskite Methylammonium Lead Bromide Nanoplatelets. *Chem. Mater.* **2016,** *28* (19), 6909-6916.
36. Huang, H.; Susha, A. S.; Kershaw, S. V.; Hung, T. F.; Rogach, A. L., Control of Emission Color of High Quantum Yield CH3NH3PbBr3 Perovskite Quantum Dots by Precipitation Temperature. *Advanced science* **2015,** *2* (9), 1500194.
37. de Mello Donega, C.; Liljeroth, P.; Vanmaekelbergh, D., Physicochemical evaluation of the hot-injection method, a synthesis route for monodisperse nanocrystals. *Small* **2005,** *1* (12), 1152-62.
38. Yu, W. W.; Peng, X., Formation of High-Quality CdS and Other II-VI Semiconductor Nanocrystals in Noncoordinating Solvents: Tunable Reactivity of Monomers. *Angew. Chem. Int. Ed.* **2002,** *41* (13), 2368-2371.
39. Imran, M.; Caligiuri, V.; Wang, M.; Goldoni, L.; Prato, M.; Krahne, R.; De Trizio, L.; Manna, L., Benzoyl Halides as Alternative Precursors for the Colloidal Synthesis of Lead-Based Halide Perovskite Nanocrystals. *J. Am. Chem. Soc.* **2018,** *140* (7), 2656-2664.
40. Almeida, G.; Goldoni, L.; Akkerman, Q.; Dang, Z.; Khan, A. H.; Marras, S.; Moreels, I.; Manna, L., Role of Acid-Base Equilibria in the Size, Shape, and Phase Control of Cesium Lead Bromide Nanocrystals. *ACS nano* **2018,** *12* (2), 1704-1711.
41. Zhang, F.; Huang, S.; Wang, P.; Chen, X.; Zhao, S.; Dong, Y.; Zhong, H., Colloidal Synthesis of Air-Stable CH3NH3PbI3 Quantum Dots by Gaining Chemical Insight into the Solvent Effects. *Chem. Mater.* **2017,** *29* (8), 3793-3799.
42. Bodnarchuk, M. I.; Boehme, S. C.; Ten Brinck, S.; Bernasconi, C.; Shynkarenko, Y.; Krieg, F.; Widmer, R.; Aeschlimann, B.; Gunther, D.; Kovalenko, M. V.; Infante, I., Rationalizing and Controlling the Surface

Structure and Electronic Passivation of Cesium Lead Halide Nanocrystals. *Acs Energy Lett* **2019,** *4* (1), 63-74.
43. Chen, Y.; Smock, S. R.; Flintgruber, A. H.; Perras, F. A.; Brutchey, R. L.; Rossini, A. J., Surface Termination of CsPbBr3 Perovskite Quantum Dots Determined by Solid-State NMR Spectroscopy. *J. Am. Chem. Soc.* **2020**.
44. De Roo, J.; Ibanez, M.; Geiregat, P.; Nedelcu, G.; Walravens, W.; Maes, J.; Martins, J. C.; Van Driessche, I.; Kovalenko, M. V.; Hens, Z., Highly Dynamic Ligand Binding and Light Absorption Coefficient of Cesium Lead Bromide Perovskite Nanocrystals. *ACS nano* **2016,** *10* (2), 2071-81.
45. Thapa, S.; Bhardwaj, K.; Basel, S.; Pradhan, S.; Eling, C. J.; Adawi, A. M.; Bouillard, J.-S. G.; Stasiuk, G. J.; Reiss, P.; Pariyar, A.; Tamang, S., Long-term ambient air-stable cubic CsPbBr3 perovskite quantum dots using molecular bromine. *Nanoscale Advances* **2019,** *1* (9), 3388-3391.
46. Wu, L.; Zhong, Q.; Yang, D.; Chen, M.; Hu, H.; Pan, Q.; Liu, H.; Cao, M.; Xu, Y.; Sun, B.; Zhang, Q., Improving the Stability and Size Tunability of Cesium Lead Halide Perovskite Nanocrystals Using Trioctylphosphine Oxide as the Capping Ligand. *Langmuir : the ACS journal of surfaces and colloids* **2017,** *33* (44), 12689-12696.
47. Almeida, G.; Ashton, O. J.; Goldoni, L.; Maggioni, D.; Petralanda, U.; Mishra, N.; Akkerman, Q. A.; Infante, I.; Snaith, H. J.; Manna, L., The Phosphine Oxide Route toward Lead Halide Perovskite Nanocrystals. *J. Am. Chem. Soc.* **2018,** *140* (44), 14878-14886.
48. Li, Y.; Wang, X.; Xue, W.; Wang, W.; Zhu, W.; Zhao, L., Highly luminescent and stable CsPbBr3 perovskite quantum dots modified by phosphine ligands. *Nano Research* **2019,** *12* (4), 785-789.
49. Cao, Y.; Zhu, W.; Li, L.; Zhang, Z.; Chen, Z.; Lin, Y.; Zhu, J. J., Size-selected and surface-passivated CsPbBr3 perovskite nanocrystals for self-enhanced electrochemiluminescence in aqueous media. *Nanoscale* **2020,** *12* (13), 7321-7329.
50. Zhang, B.; Goldoni, L.; Zito, J.; Dang, Z.; Almeida, G.; Zaccaria, F.; de Wit, J.; Infante, I.; De Trizio, L.; Manna, L., Alkyl Phosphonic Acids Deliver CsPbBr3 Nanocrystals with High Photoluminescence Quantum Yield and Truncated Octahedron Shape. *Chem. Mater.* **2019,** *31* (21), 9140-9147.
51. Liu, Y.; Li, D.; Zhang, L.; Chen, Y.; Geng, C.; Shi, S.; Zhang, Z.; Bi, W.; Xu, S., Amine- and Acid-Free Synthesis of Stable CsPbBr3 Perovskite Nanocrystals. *Chem. Mater.* **2020,** *32* (5), 1904-1913.
52. Krieg, F.; Ochsenbein, S. T.; Yakunin, S.; Ten Brinck, S.; Aellen, P.; Suess, A.; Clerc, B.; Guggisberg, D.; Nazarenko, O.; Shynkarenko, Y.; Kumar, S.; Shih, C. J.; Infante, I.; Kovalenko, M. V., Colloidal CsPbX3 (X = Cl, Br, I) Nanocrystals 2.0: Zwitterionic Capping Ligands for Improved Durability and Stability. *Acs Energy Lett* **2018,** *3* (3), 641-646.
53. Zhou, Y.; Liu, C.; Zhao, Z.; Zhang, W.; Li, K.; Ye, Y.; Zhu, C. F.; Meng, X. G., Enhanced luminescence of Mn doped CsPbCl3 and CsPb(Cl/Br)3 perovskite nanocrystals stabilized in glasses. *J. Alloys Compd.* **2020,** *827*, 154349.
54. Chen, C.; Li, D.; Wu, Y.; Chen, C.; Zhu, Z. G.; Shih, W. Y.; Shih, W. H., Flexible inorganic CsPbI3 perovskite nanocrystal-PMMA composite films with enhanced stability in air and water for white light-emitting diodes. *Nanotechnology* **2020,** *31* (22), 225602.
55. Kairdolf, B. A.; Smith, A. M.; Stokes, T. H.; Wang, M. D.; Young, A. N.; Nie, S., Semiconductor quantum dots for bioimaging and biodiagnostic applications. *Annual review of analytical chemistry* **2013,** *6*, 143-62.
56. Buckley, S.; Rivoire, K.; Vuckovic, J., Engineered quantum dot single-photon sources. *Rep. Prog. Phys.* **2012,** *75* (12), 126503.
57. Reiss, P.; Protiere, M.; Li, L., Core/Shell semiconductor nanocrystals. *Small* **2009,** *5* (2), 154-68.
58. Wang, S.; Bi, C.; Yuan, J.; Zhang, L.; Tian, J., Original Core–Shell Structure of Cubic CsPbBr3@Amorphous CsPbBrx Perovskite Quantum Dots with a High Blue Photoluminescence Quantum Yield of over 80%. *Acs Energy Lett* **2017,** *3* (1), 245-251.
59. Quan, L. N.; Quintero-Bermudez, R.; Voznyy, O.; Walters, G.; Jain, A.; Fan, J. Z.; Zheng, X.; Yang, Z.; Sargent, E. H., Highly Emissive Green Perovskite Nanocrystals in a Solid State Crystalline Matrix. *Adv. Mater.* **2017,** *29* (21).
60. Jia, C.; Li, H.; Meng, X.; Li, H., CsPbX3/Cs4PbX6 core/shell perovskite nanocrystals. *Chem Commun (Camb)* **2018,** *54* (49), 6300-6303.
61. Tang, X.; Yang, J.; Li, S.; Chen, W.; Hu, Z.; Qiu, J., CsPbBr3/CdS Core/Shell Structure Quantum Dots for Inverted Light-Emitting Diodes Application. *Frontiers in chemistry* **2019,** *7*, 499.

62. Tang, X.; Yang, J.; Li, S.; Liu, Z.; Hu, Z.; Hao, J.; Du, J.; Leng, Y.; Qin, H.; Lin, X.; Lin, Y.; Tian, Y.; Zhou, M.; Xiong, Q., Single Halide Perovskite/Semiconductor Core/Shell Quantum Dots with Ultrastability and Nonblinking Properties. *Advanced science* **2019,** *6* (18), 1900412.
63. Kwak, J.; Lim, J.; Park, M.; Lee, S.; Char, K.; Lee, C., High-Power Genuine Ultraviolet Light-Emitting Diodes Based On Colloidal Nanocrystal Quantum Dots. *Nano Lett.* **2015,** *15* (6), 3793-9.
64. van der Stam, W.; Geuchies, J. J.; Altantzis, T.; van den Bos, K. H.; Meeldijk, J. D.; Van Aert, S.; Bals, S.; Vanmaekelbergh, D.; de Mello Donega, C., Highly Emissive Divalent-Ion-Doped Colloidal CsPb1-xMxBr3 Perovskite Nanocrystals through Cation Exchange. *J. Am. Chem. Soc.* **2017,** *139* (11), 4087-4097.
65. Ravi, V. K.; Saikia, S.; Yadav, S.; Nawale, V. V.; Nag, A., CsPbBr3/ZnS Core/Shell Type Nanocrystals for Enhancing Luminescence Lifetime and Water Stability. *Acs Energy Lett* **2020,** *5* (6), 1794-1796.
66. Ren, Y.; Nie, Z.; Deng, F.; Wang, Z.; Xia, S.; Wang, Y., Deciphering the excited-state dynamics and multicarrier interactions in perovskite core-shell type hetero-nanocrystals. *Nanoscale* **2021,** *13* (1), 292-299.
67. Dutta, A.; Dutta, S. K.; Das Adhikari, S.; Pradhan, N., Phase-Stable CsPbI3 Nanocrystals: The Reaction Temperature Matters. *Angew. Chem. Int. Ed.* **2018,** *57* (29), 9083-9087.
68. Li, Z.-J.; Hofman, E.; Li, J.; Davis, A. H.; Tung, C.-H.; Wu, L.-Z.; Zheng, W., Photoelectrochemically Active and Environmentally Stable CsPbBr3/TiO2 Core/Shell Nanocrystals. *Adv. Funct. Mater.* **2018,** *28* (1), 1704288.
69. R, S.; Vishaka, H. V.; J, K.; Balakrishna, R. G., Green to Blue Light Emitting CsPbBr3 Perovskite by Ligand Exchange and its Encapsulation by TiO2 for Tandem Effect in Photovoltaic Applications. *ACS Applied Nano Materials* **2020,** *3* (6), 6089-6098.
70. Zhong, Q.; Cao, M.; Hu, H.; Yang, D.; Chen, M.; Li, P.; Wu, L.; Zhang, Q., One-Pot Synthesis of Highly Stable CsPbBr3@SiO2 Core-Shell Nanoparticles. *ACS nano* **2018,** *12* (8), 8579-8587.
71. Wang, B.; Zhang, S.; Liu, B.; Li, J.; Cao, B.; Liu, Z., Stable CsPbBr3:Sn@SiO2 and Cs4PbBr6:Sn@SiO2 Core–Shell Quantum Dots with Tunable Color Emission for Light-Emitting Diodes. *ACS Applied Nano Materials* **2020,** *3* (3), 3019-3027.
72. Qiu, L.; Yang, H.; Dai, Z.; Sun, F.; Hao, J.; Guan, M.; Dang, P.; Yan, C.; Lin, J.; Li, G., Highly Efficient and Stable CsPbBr3 Perovskite Quantum Dots by Encapsulating in Dual-Shell Hollow Silica Spheres for WLEDs. *Inorganic Chemistry Frontiers* **2020**.
73. Ji, Y.; Wang, M.; Yang, Z.; Qiu, H.; Ji, S.; Dou, J.; Gaponenko, N. V., Highly stable Na: CsPb(Br,I)3@Al2O3 nanocomposites prepared by a pre-protection strategy. *Nanoscale* **2020,** *12* (11), 6403-6410.
74. Song, P.; Qiao, B.; Song, D.; Cao, J.; Shen, Z.; Zhang, G.; Xu, Z.; Zhao, S.; Wageh, S.; Al-Ghamdi, A., Enhancing the stability and water resistance of CsPbBr3 perovskite nanocrystals by using tetrafluoride and zinc oxide as protective capsules. *Journal of Materials Science* **2020**.
75. Benioff, P., The computer as a physical system: A microscopic quantum mechanical Hamiltonian model of computers as represented by Turing machines. *Journal of Statistical Physics* **1980,** *22* (5), 563-591.
76. Chuang, I. L.; Gershenfeld, N.; Kubinec, M., Experimental Implementation of Fast Quantum Searching. *Phys. Rev. Lett.* **1998,** *80* (15), 3408-3411.
77. Eisaman, M. D.; Fan, J.; Migdall, A.; Polyakov, S. V., Invited review article: Single-photon sources and detectors. *Rev. Sci. Instrum.* **2011,** *82* (7), 071101.
78. Lounis, B.; Orrit, M., Single-photon sources. *Rep. Prog. Phys.* **2005,** *68* (5), 1129-1179.
79. Kimble, H. J.; Dagenais, M.; Mandel, L., Photon Antibunching in Resonance Fluorescence. *Phys. Rev. Lett.* **1977,** *39* (11), 691-695.
80. Brown, R. H.; Twiss, R. Q., Correlation between Photons in two Coherent Beams of Light. *Nature* **1956,** *177* (4497), 27-29.
81. Hanbury Brown, R.; Twiss, R. Q., Interferometry of the intensity fluctuations in light - I. Basic theory: the correlation between photons in coherent beams of radiation. *Proceedings of the Royal Society of London. Series A. Mathematical and Physical Sciences* **1997,** *242* (1230), 300-324.
82. Hong, C. K.; Ou, Z. Y.; Mandel, L., Measurement of subpicosecond time intervals between two photons by interference. *Phys. Rev. Lett.* **1987,** *59* (18), 2044-2046.
83. Fearn, H.; Loudon, R., Theory of two-photon interference. *Journal of the Optical Society of America B* **1989,** *6* (5), 917.

84. Bylander, J.; Robert-Philip, I.; Abram, I., Interference and correlation of two independent photons. *The European Physical Journal D* **2003,** *22* (2), 295-301.
85. Santori, C.; Fattal, D.; Vuckovic, J.; Solomon, G. S.; Yamamoto, Y., Indistinguishable photons from a single-photon device. *Nature* **2002,** *419* (6907), 594-7.
86. Pittman, T. B.; Jacobs, B. C.; Franson, J. D., Single photons on pseudodemand from stored parametric down-conversion. *Physical Review A* **2002,** *66* (4).
87. Couteau, C., Spontaneous parametric down-conversion. *Contemporary Physics* **2018,** *59* (3), 291-304.
88. Ngah, L. A.; Alibart, O.; Labonté, L.; D'Auria, V.; Tanzilli, S., Ultra-fast heralded single photon source based on telecom technology. *Laser & Photonics Reviews* **2015,** *9* (2), L1-L5.
89. Hu, F.; Zhang, H.; Sun, C.; Yin, C.; Lv, B.; Zhang, C.; Yu, W. W.; Wang, X.; Zhang, Y.; Xiao, M., Superior Optical Properties of Perovskite Nanocrystals as Single Photon Emitters. *ACS nano* **2015,** *9* (12), 12410-6.
90. Fisher, B.; Caruge, J. M.; Zehnder, D.; Bawendi, M., Room-temperature ordered photon emission from multiexciton states in single CdSe core-shell nanocrystals. *Phys. Rev. Lett.* **2005,** *94* (8), 087403.
91. Chandrasekaran, V.; Tessier, M. D.; Dupont, D.; Geiregat, P.; Hens, Z.; Brainis, E., Nearly Blinking-Free, High-Purity Single-Photon Emission by Colloidal InP/ZnSe Quantum Dots. *Nano Lett.* **2017,** *17* (10), 6104-6109.
92. Raino, G.; Nedelcu, G.; Protesescu, L.; Bodnarchuk, M. I.; Kovalenko, M. V.; Mahrt, R. F.; Stoferle, T., Single Cesium Lead Halide Perovskite Nanocrystals at Low Temperature: Fast Single-Photon Emission, Reduced Blinking, and Exciton Fine Structure. *ACS nano* **2016,** *10* (2), 2485-90.
93. Utzat, H.; Sun, W.; Kaplan, A. E. K.; Krieg, F.; Ginterseder, M.; Spokoyny, B.; Klein, N. D.; Shulenberger, K. E.; Perkinson, C. F.; Kovalenko, M. V.; Bawendi, M. G., Coherent single-photon emission from colloidal lead halide perovskite quantum dots. *Science* **2019,** *363* (6431), 1068-1072.
94. Ricci, F.; Marougail, V.; Varnavski, O.; Wu, Y.; Padgaonkar, S.; Irgen-Gioro, S.; Weiss, E. A.; Goodson, T., 3rd, Enhanced Exciton Quantum Coherence in Single CsPbBr3 Perovskite Quantum Dots using Femtosecond Two-Photon Near-Field Scanning Optical Microscopy. *ACS nano* **2021**.
95. Tomm, N.; Javadi, A.; Antoniadis, N. O.; Najer, D.; Löbl, M. C.; Korsch, A. R.; Schott, R.; Valentin, S. R.; Wieck, A. D.; Ludwig, A., A bright and fast source of coherent single photons. *Nature nanotechnology* **2021,** *16* (4), 399-403.
96. Anonymous, Proceedings of the American Physical Society. *Physical Review* **1946,** *69* (11-12), 674-674.
97. Kinkhabwala, A.; Yu, Z.; Fan, S.; Avlasevich, Y.; Müllen, K.; Moerner, W. E., Large single-molecule fluorescence enhancements produced by a bowtie nanoantenna. *Nature Photonics* **2009,** *3* (11), 654-657.
98. Curto, A. G.; Volpe, G.; Taminiau, T. H.; Kreuzer, M. P.; Quidant, R.; van Hulst, N. F., Unidirectional emission of a quantum dot coupled to a nanoantenna. *Science* **2010,** *329* (5994), 930-3.
99. Akselrod, G. M.; Argyropoulos, C.; Hoang, T. B.; Ciracì, C.; Fang, C.; Huang, J.; Smith, D. R.; Mikkelsen, M. H., Probing the mechanisms of large Purcell enhancement in plasmonic nanoantennas. *Nature Photonics* **2014,** *8* (11), 835-840.
100. Coenen, T.; Vesseur, E. J.; Polman, A.; Koenderink, A. F., Directional emission from plasmonic Yagi-Uda antennas probed by angle-resolved cathodoluminescence spectroscopy. *Nano Lett.* **2011,** *11* (9), 3779-84.
101. Hoang, T. B.; Akselrod, G. M.; Mikkelsen, M. H., Ultrafast Room-Temperature Single Photon Emission from Quantum Dots Coupled to Plasmonic Nanocavities. *Nano Lett.* **2016,** *16* (1), 270-5.
102. Cibert, J.; Scalbert, D., Diluted Magnetic Semiconductors: Basic Physics and Optical Properties. In *Spin Physics in Semiconductors*, Dyakonov, M. I., Ed. Springer Berlin Heidelberg: Berlin, Heidelberg, 2008; pp 389-431.
103. Holub, M.; Bhattacharya, P., Spin-polarized light-emitting diodes and lasers. *J. Phys. D: Appl. Phys.* **2007,** *40* (11), R179-R203.
104. Sato, K.; Bergqvist, L.; Kudrnovský, J.; Dederichs, P. H.; Eriksson, O.; Turek, I.; Sanyal, B.; Bouzerar, G.; Katayama-Yoshida, H.; Dinh, V. A.; Fukushima, T.; Kizaki, H.; Zeller, R., First-principles theory of dilute magnetic semiconductors. *Reviews of Modern Physics* **2010,** *82* (2), 1633-1690.
105. Wei, S. H.; Zunger, A., Total-energy and band-structure calculations for the semimagnetic Cd1-xMnxTe semiconductor alloy and its binary constituents. *Physical review. B, Condensed matter* **1987,** *35* (5), 2340-2365.

106. Zener, C., Interaction between thed-Shells in the Transition Metals. II. Ferromagnetic Compounds of Manganese with Perovskite Structure. *Physical Review* **1951,** *82* (3), 403-405.
107. Simmonds, P. E.; Stradling, R. A.; Birch, J. R.; Bradley, C. C., Zeeman Splitting and Chemical Shifts for the Shallow Donor States in CdTe. *physica status solidi (b)* **1974,** *64* (1), 195-203.
108. Twardowski, A.; von Ortenberg, M.; Demianiuk, M.; Pauthenet, R., Magnetization and exchange constants in Zn1−xMnxSe. *Solid State Commun.* **1984,** *51* (11), 849-852.
109. Ohno, Y.; Young, D. K.; Beschoten, B.; Matsukura, F.; Ohno, H.; Awschalom, D. D., Electrical spin injection in a ferromagnetic semiconductor heterostructure. *Nature* **1999,** *402* (6763), 790-792.

Chapter 2: Synthesis and characterization of $CsPbBr_3/AlO_x$ core/shell nanocrystals

Introduction

The ultimate goal of shell passivation of lead halide perovskite NCs is to preserve their optical properties and structural integrity against moisture and air. To this end, various core/shell structures have been investigated,[1-14] and two types of shell materials are prominently shown: binary semiconductor compounds and oxides. The growth of binary compounds (e.g., ZnS, CdS) can be seamlessly incorporated into the synthesis of the $CsPbBr_3$ core, as they share many reaction conditions typical for NC synthesis.[2-3, 11] However, due to low formation energy, the core NCs inevitably grow during the shell synthesis. Therefore, control of the shell thickness is coupled to the control of the particle size, making shell thickness optimization difficult to achieve. On the other hand, oxide shells are usually grown on pre-synthesized core NCs, allowing the shell thickness to be modified independently.[13-14] Furthermore, oxides are hydrophilic in nature, which theoretically can improve the dispersibility of the NCs in polar solvents such as water.[7] The main concern with oxide shells is that the synthesis of these shells is based in most cases on the sol-gel approach. The polycondensation reaction requires water to trigger and releases alcohol as a side product, the two most "dangerous" chemicals the unprotected $CsPbBr_3$ NCs can be in contact with. In addition, the reaction rate can be very fast, resulting in a sudden increase of alcohol concentration in the reaction mixture, and an amorphous shell that is not densely packed, compromising its ability to efficiently passivate the surface. Improving the crystallinity of the shell is not a viable option, as the only method is calcination, which can drastically reduce the performance of the core/shell structure.[9]

To improve the oxide shell growth, finding a synthetic method that can reduce the impact of water and alcohol in the system is preferable. Loiudice et al. presented a non-sol-gel reaction scheme for AlO_x, avoiding the presence of polar solvents while achieving great control over the shell thickness.[13] This reaction involves trimethylaluminum and oxygen, which were introduced to the surface of $CsPbBr_3$ NCs sequentially to form the shell in a layer-by-layer fashion. Despite such fine control over the shell, the reactant used was highly pyrophoric, which made it less appealing for large-scale production of core/shell NCs. In addition, the ALD-type growth (atomic layer deposition), in which at each reaction step one single Al layer is deposited and then oxidized, is time-consuming and requires the precise knowledge of the amount of precursors to be used in each step. We propose instead a novel non-hydrolytic sol-gel reaction route, which eliminates the use of water and regulates the rate of alcohol production, resulting in $CsPbBr_3/AlO_x$ NCs with high PLQY and improved photostability.

Materials and Methods

$CsPbBr_3$ NC synthesis

$CsPbBr_3$ NC synthesis followed the three-precursor method reported by Imran et al.[15] Briefly, in a 50 mL round-bottom flask, 76 mg (0.19 mmol) of lead acetate trihydrate ($Pb(OAc)_2.3H_2O$, 99.99+%, Sigma-Aldrich) and 16 mg (0.05 mmol) of cesium carbonate (Cs_2CO_3, 99.95%, Sigma-Aldrich) were added to 5 mL of 1-octadecene (ODE, 90%, Acros Organics), followed by the addition of 0.3 mL (0.95 mmol) of oleic acid (OA, 90%, Sigma-Aldrich) and 1 mL (3 mmol) of oleylamine (OLA, ≥98%, Sigma-Aldrich). The mixture was degassed under a primary vacuum at 120°C for 1 hour. Then the reaction flask was backfilled with Ar, and the temperature was raised to 170°C. 0.1 mL (0.85 mmol) of benzoyl bromide (97%, Sigma-Aldrich) was injected into the flask and the reaction was quenched immediately

with an ice bath. The obtained product was centrifuged at 7500 rpm for 6 minutes and the precipitate was redispersed in 5 mL of degassed toluene. The dispersion underwent another centrifugation cycle at 2000 rpm for 5 minutes and the small amount of precipitate, containing aggregated nanocrystals, was discarded. Following Refs. 16-17, the concentration of the NC colloidal solutions was estimated based on the Beer-Lambert law. [16-17] The absorption spectrum of each sample was taken at 500-fold dilution. The absorbance at 335 nm and 400 nm were used for calculation, and the molar absorption coefficients were obtained from the aforementioned works. Since this parameter changes with the size of the NC, an average size of 8 nm was used, based on TEM images. This procedure was repeated for the dilution factors of 167 and 250, and the obtained values were averaged. Next, assuming a cubic structure with a lattice parameter of 5.845 Å for the ease of calculation (from Le Bail refinement using the cubic structure), each NC contains 2564 Pb atoms. This value is multiplied by the concentration of NCs to yield the estimated molar amount of Pb in a given sample, which served as the base for the Al/Pb feed ratio calculations.

$CsPbBr_3/AlO_x$ NC synthesis with $Pb(OA)_2$ and $AlBr_3$

Lead oleate ($Pb(OA)_2$) was synthesized with the procedure from Ruan et al.[18] 36.38 mg (0.16 mmol) of PbO (99.999% trace metal basis, Sigma-Aldrich) and 0.15 mL of OA were added to 8 mL of toluene (For analysis, Carlo Erba) in a 50 mL round bottom flask and heated to 100°C for 1 hour. The solution was then stored in the dark until used. Initially, the concentration of $Pb(OA)_2$ was 0.02 M. After some time, it started to form a white precipitate and had to be prepared again.

The growth of the AlO_x shell was based on the reaction from Acosta et al.[19] 1 mL dispersion of 2.8 µM core NCs in toluene was first treated with 0.18 µmol of $Pb(OA)_2$ for 30 minutes before 150 µmol of $AlBr_3$ in toluene were added, followed by 30 minutes of stirring. Then, the dispersion was washed with 1 mL of methyl acetate to remove excess $AlBr_3$, and 150 µmol of aluminum isopropoxide ($Al(IPA)_3$, 99.99%, Sigma Aldrich) was added dropwise at a rate of 2 mL/hr. When the addition was finished, the dispersion was precipitated with methyl acetate (volume ratio of MeOAc : dispersion = 2:1) at 12000 rpm for 10 minutes and redispersed in 1 mL of toluene.

$CsPbBr_3/AlO_x$ NC synthesis with $AlBr_3/CH_2Br_2$

We utilized the same shell growth reaction but with two types of aluminum bromide solutions. The first is obtained by dissolving 26.7 mg aluminum bromide powder ($AlBr_3$, 99.99%+, Sigma-Aldrich) in 5 mL of anhydrous toluene. After the dissolution was complete, the solution turned yellow. The second was obtained by diluting 0.1 mL $AlBr_3/CH_2Br_2$ solution (1M, Sigma-Aldrich) in 4.9 mL of anhydrous toluene. The two solutions were then mixed with a volume ratio of 1:1 to obtain the final $AlBr_3$ precursor solution used in the synthesis. The $Al(IPA)_3$ solution was prepared by dissolving 20.4 mg $Al(IPA)_3$ powder in 5 mL anhydrous toluene.

For a thin shell of AlO_x, 2 mL of 2.4 µM $CsPbBr_3$ NCs were precipitated from the stock solution using methyl acetate, then redispersed in 4 mL of anhydrous toluene and added to a 50 mL round-bottom flask. Then, 5 µL of oleic acid and 1.2 mL of $Al(IPA)_3$ and $AlBr_3$ precursor solutions prepared above were added to the flask using two separate syringe pump with the same rate of 1 mL/h. Immediately after the addition, the product was precipitated with anhydrous MeOAc (volume ratio of MeOAc : toluene = 2:1). It was then redispersed in 2 mL of anhydrous toluene and centrifuged at 5000 rpm for 5 minutes, and the precipitate was discarded. The shell growth was then repeated once more to obtain a thicker AlO_x shell. However, after the addition is completed, the suspension was allowed to react for

one hour before being purified with MeOAc. The shell growth using $AlBr_3/CH_2Br_2$ as the sole $AlBr_3$ precursor was performed with all conditions being identical except for the reaction time. In this case, the addition time was 3 hours, then the mixture was allowed to react for one more hour before being stopped.

Characterization

Scanning electron microscopy (SEM) measurements were performed on a ZEISS Ultra 55 FE scanning electron microscope equipped with a Bruker QUANTAX EDS system, and transmission electron microscopy (TEM) images were collected with an FEI Tecnai F20 microscope. For powder X-ray diffraction (XRD), the samples were drop-cast on a disoriented silicon substrate, and the measurements were performed with a PANalytical X'pert Pro powder diffractometer equipped with a copper anode (λK_α=1.5406 Å) and an X' Celerator 1D detector. HighScore Plus software was used for the Le Bail refinement of the crystal lattice. Fourier-transform infrared spectroscopy (FTIR) measurements were carried out with a Perkin Elmer Paragon 500 spectrometer in attenuated total reflection (ATR) mode. ICP-AES measurements were performed on a Shimadzu 9000 spectrometer. Standard solutions of Pb and Al were prepared by diluting the ICP standards of the two metal ions with Milli-Q water containing HNO_3 10% (v/v). Subsequently, calibration curves were established for the concentration range relevant to our samples. The detection wavelength for each element was 405.783 nm (Pb), and 396.153 nm (Al). X-ray photoelectron spectroscopy (XPS) analyses were carried out with a Versa Probe II spectrometer (ULVAC-PHI) equipped with a monochromated Al Kα source (hv = 1486.6 eV). The core-level peaks were recorded with a constant pass energy of 23.3 eV. The XPS spectra were fitted with CasaXPS 2.3 software using Shirley background. Binding energies (BEs) are referenced with respect to adventitious carbon (C 1s BE = 284.8 eV). For UV-vis and PL measurements, a Hewlett Packard 8452A diode-array spectrophotometer and a Hitachi F-4500 fluorescence spectrophotometer were used, respectively. Time-resolved photoluminescence measurements were peformed with a Fluorolog-3 spectrofluorometer (Jobin-Yvon), using a 455 nm nanoLED laser diode for excitation (repetition rate 1 MHz). The decay data were analyzed with the Decay Analysis software from Horiba Scientist. Measurements of the absolute photoluminescence quantum yield (PLQY) were performed on the same spectrometer equipped with an integrating sphere, using an R928 PMT detector, and a 450 W Xenon lamp as the excitation source. The excitation wavelength was 420 nm and the optical density of the samples at this wavelength was adjusted between 0.1 and 0.2.

Stability measurement

The stability test was performed by irradiating a monolayer film of NCs on a silicon substrate with a laser. To prepare the film, silicon wafers were cut into 5mm x 5mm substrates, washed twice with acetone and then once with isopropanol in an ultrasonic bath. The substrates were then dried and finally treated with UV-ozone for 15 minutes. The deposition method differed depending on whether the NCs were of core or core/shell type. For core NCs, 5 µL of a 1 nM suspension was drop casted on the substrate and dried under ambient conditions. Core/shell NCs (5 µL, 3 µM) were instead spin-coated at 2000 rpm (500 rpm/s) for 60 s. The signal was then collected by a Horiba iHR-550 spectrometer coupled with a Princeton Instrument CCD camera. The irradiation source was provided by a continuous wave 405 nm semiconductor laser with a power density of 154 W/cm^2. To calculate the laser spot size, images of the laser spot with unsaturated intensity and a patterned Si substrate were taken with the CCD camera. The sizes of the spot and the patterns were measured in pixels. Then, the pattern's size was measured in µm with the SEM. The size of the spot was converted from

pixel to µm using the values of the pattern. The obtained conversion was 0.77 µm/pixel, and the corresponding laser spot diameter and area were 2.3 µm and 4.2 μm^2, respectively.

Results and Discussion

$CsPbBr_3$ core NCs

The synthesis of the $CsPbBr_3$ NCs has been well established in the literature. So far, the most widely used method is the original hot-injection synthesis with two precursors reported by Protesecu et al.[20] However, this method has two drawbacks. First, $PbBr_2$ is used as the common precursor for both lead and bromine, limiting the tunability of the amount of each element. This is especially important considering that the PLQY and stability of $CsPbBr_3$ NCs is directly related to the amount of Br^- present.[21] Second, the synthesis relies on injecting pre-prepared cesium oleate (Cs-oleate) at 100°C into the reaction medium. Increasing the temperature is required for this precursor due to its insolubility in 1-octadecene at room temperature. As soon as the precursor is loaded into the syringe for the injection, it starts to cool down, causing a slight variation in the amount actually injected. This is a source of irreproducibility, given the fact that the reaction is highly sensitive even to subtle changes. Cs-oleate can be made soluble by adding an excess of OA during its preparation,[22] but the excess acid can interfere with the other reagents and modify the outcome of the synthesis. On the other hand, the three-precursor method reported by Imran et al.[15] can circumvent both limitations by injecting the halide precursor at room temperature to the reaction mixture containing the lead and cesium precursors. By separating the lead and halide precursors, the amount of each element can be tuned independently. Additionally, the use of cesium oleate is avoided, reducing the number of steps and the problems associated with this precursor. For these reasons, we chose to use the three-precursor method in all our preparation of $CsPbBr_3$ NCs.

The obtained NCs have a size of 7.60 ± 1.20 nm, with an orthorhombic structure (ICDD 04-014-9676) (Figure 2.1). The excitonic and photoluminescence peaks of the NCs are at 499 nm and 509 nm, respectively. These values change slightly between batches but generally vary within a narrow range of 5 nm. The luminescence decay curve features two components with lifetimes of 1.80 ns (91%) and 10.0 ns (9%). The percentages in parentheses refer to the relative amplitude of each component. These lifetime components correspond to the decay of free and localized charge carriers, respectively.[23-24]

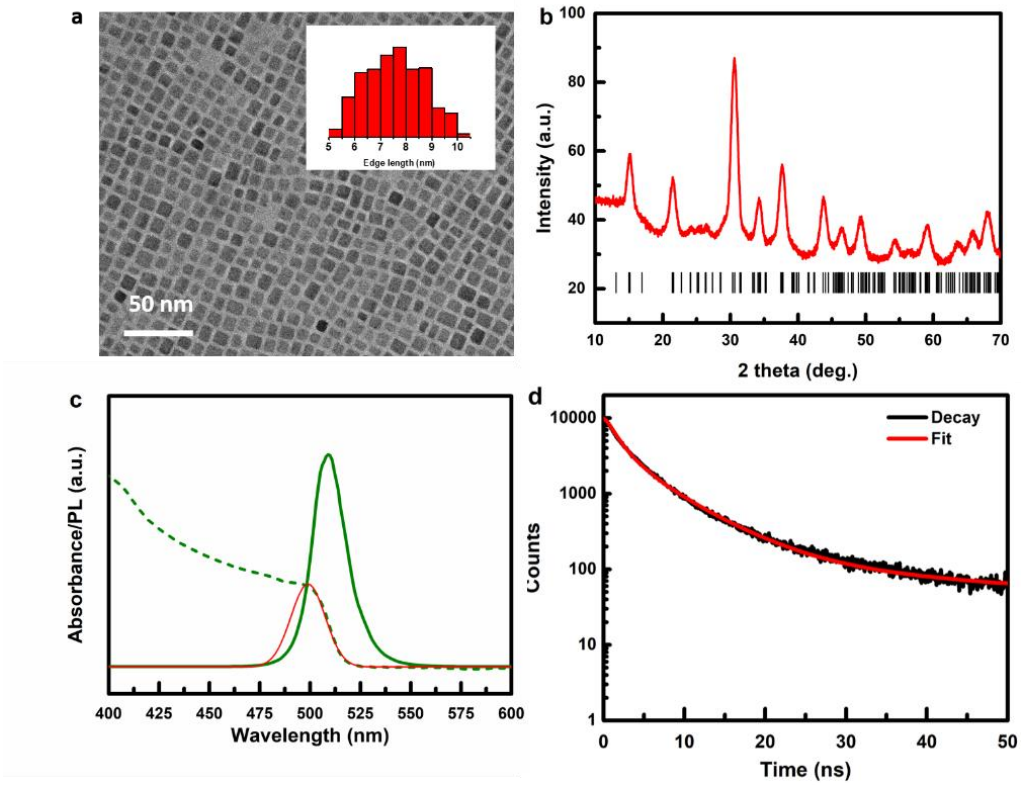

Figure 2.1. Basic characterization of the synthesized $CsPbBr_3$ nanocubes, featuring a TEM image with the corresponding size distribution (a), the XRD pattern, with the black bars indicating the peak positions of the orthorhombic $CsPbBr_3$ reference patterns (ICDD 04-014-9676) (b), the absorption and emission spectra (c), and the time-resolved photoluminescence spectrum (d) taken at the emission wavelength of 509 nm.

At the single particle level, $CsPbBr_3$ NCs feature a much narrower linewidth (~1 meV) compared to an ensemble of NCs (35 meV) (Figure 2.2), which is in good agreement with the published literature.[25] As the synthesized NCs have a certain size dispersion and are with 7-8 nm in the weak confinement regime, the effect of quantum confinement on the band gap energy of each nanocrystal varies slightly. When an ensemble of NCs is excited, the emitted photons carry these energy variations, contributing to the broadening of the emission spectra. This type of broadening is termed inhomogeneous broadening. Reducing the number of particles measured would also reduce the degree of this broadening. In our case, however, the emission spectra of several NCs were still recorded simultaneously. This is because the laser's spot size is 2.3 µm, while the distance between particles is only a few hundred nm (Figure 2.2a). Nevertheless, this distance is still long enough for the spectra of different particles to be well resolved.

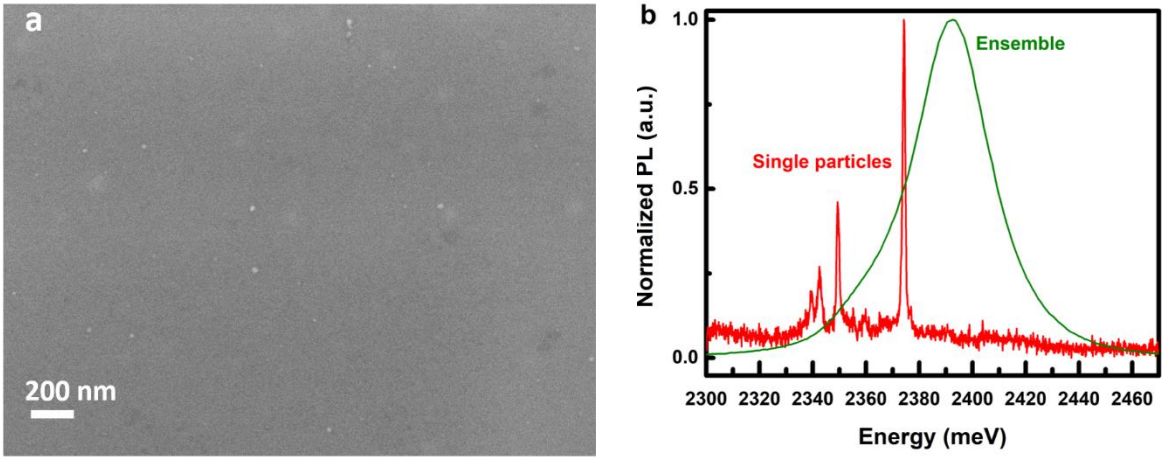

Figure 2.2. a) SEM image of $CsPbBr_3$ NCs (white dots) deposited on a Si substrate, b) Emission spectra of an ensemble and single particles recorded at 14.6 K.

The linewidth of the NCs is affected not only by the inhomogeneity in size but also by intrinsic exciton–phonon interactions within each of them (homogeneous broadening). This interaction can involve either acoustic or optical phonons, and the linewidth broadening is generally modeled as:

$$W(T) = W(0) + A_{ac}T + B_{op}n_{LO}(T) \qquad \text{(Eq. 2.1)}$$

where the first term refers to the broadening due to structural defects, the second accounts for acoustic phonon broadening, and the third is the longitudinal optical (LO) phonon contribution and is dependent on LO phonons density n_{LO}.[26] The expression of n_{LO} is $n_{LO}(T) = (\exp\left(\frac{E_{LO}}{k_bT}\right) - 1)^{-1}$, based on the Bose-Einstein distribution function for phonons. In our case, E_{LO} is chosen to be 18 meV due to the excitation conditions.[27] The resulting A_{ac} and B_{op} are -6 ± 38 μeV/K and 49 ± 8 meV, respectively. The large margin of error for A_{ac} comes from the weak contribution of acoustic phonons. Despite the error, the order of magnitude of each contribution is consistent with reported values.[28] Since $CsPbBr_3$ is an ionic compound, out-of-phase movements of adjacent atoms (optical phonons) create electrical dipoles, which have a strong Coulombic interaction with excited charge carriers.[27, 29] This explains the major contribution of LO phonons in the interaction with excitons we observed in the measurements.

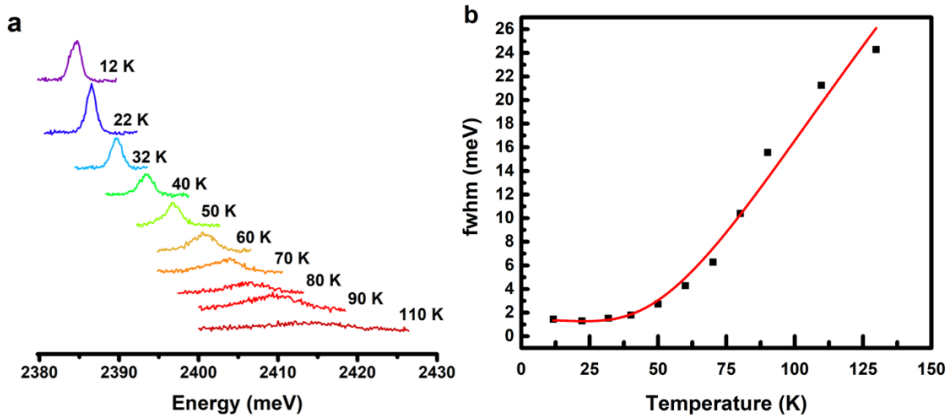

Figure 2.3. a) Evolution of the emission linewidth with the temperature for a single $CsPbBr_3$ nanocrystal. b) The fitted linewidth values using Equation 2.1 as the model.

$CsPbBr_3/AlO_x$ core/shell NCs

Core/shell synthesis with $Pb(OA)_2$

Surface functionalization of the core NCs is a crucial synthesis consideration to ensure that the shell can properly grow on the core NCs, while avoiding their ripening. As mentioned in the introduction, our study is based on the non-hydrolytic generation of AlO_x starting from $AlBr_3$ and $Al(IPA)_3$ (Figure 2.4a).[19] As a strong electrophile, $AlBr_3$ reacts with the alkoxide groups. Nuleophilic attack of Br^- at either aluminum (1) or carbon (2) atom can occur, giving rise to the exchange between Br^- and alkoxide groups and the formation of Al—O—Al bond. In our case, we are interested in the latter, which initiates the shell growth.

In principle, $AlBr_3$ could anchor on the surface of the core by occupying Br^- vacancies in a similar manner to other metal halides,[30] triggering the desired heterogeneous nucleation of the shell. However, since the nonhydrolytic sol-gel reaction between $Al(IPA)_3$ and $AlBr_3$ is rapid, there is a non-negligible possibility for AlO_x to nucleate homogeneously without coating the $CsPbBr_3$ NCs. Initial syntheses with only $AlBr_3$ dissolved in toluene were unsuccessful: AlO_x formed as amorphous aggregates of several hundred nm in size. It has been shown that adding $Pb(OA)_2$ to a suspension of $CsPbBr_3$ NCs reduced the Br/Pb ratio, presumably due to the introduction of Br vacancies.[18] These vacancies can potentially provide more binding sites for $AlBr_3$. Therefore, we treated the $CsPbBr_3$ NCs with $Pb(OA)_2$ before growing the shell.

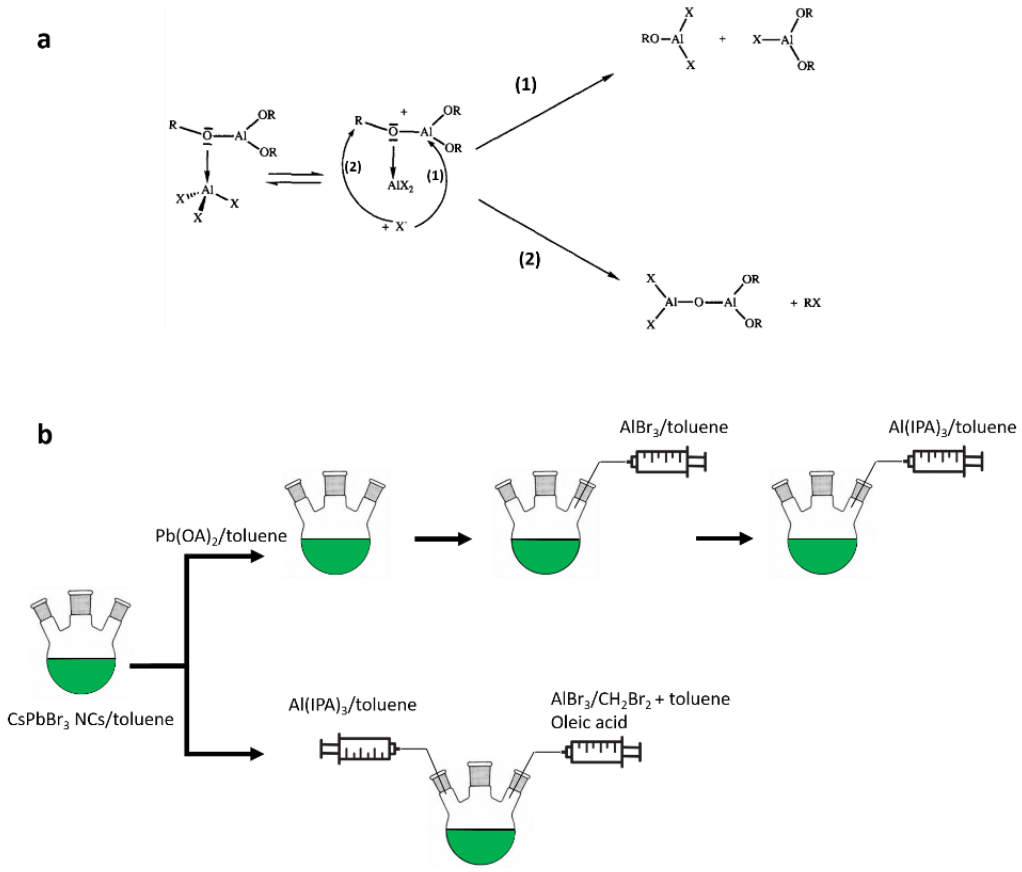

Figure 2.4. a) Scheme of the non-hydrolytic sol-gel reaction between aluminum halide and aluminum alkoxide, taken from ref. [19], b) The two approaches towards growing an AlO_x shell in this chapter, $Pb(OA)_2$ pre-treatment (above) and $AlBr_3/CH_2Br_2$ (below).

We found instead that a new doublet (137.1 eV, here and below referenced to the Pb $4f_{7/2}$ peak) appeared in the Pb 4f XPS spectrum upon the addition of $Pb(OA)_2$ (Figure 2.5 a, b). Before this addition, only the signals of Pb^{2+} species bonded with Br^- (138.2 eV) and Pb^0 (136.2 eV) were recorded.[31] The latter is often observed as a consequence of the degradation of $CsPbBr_3$ under intense X-ray irradiation, and its intensity relative to the Pb^{2+} signal varies between measurements.[32-33] The energy of the new doublet is intermediate between the two previously mentioned ones, indicating that it belongs to a Pb^{2+} species, likely Pb^{2+} bonded with O^{2-}.[31] As oleate is the only other group capable of forming such a bond with Pb^{2+} in the colloidal solution, we tentatively assign this signature to Pb-OA binding. Quantitative comparison with the doublet from $CsPbBr_3$ shows that $Pb(OA)_2$ accounts for 34% of the total Pb signal, despite the initial amount of $Pb(OA)_2$ added being much smaller. We assume that this is because XPS only probed surface and near-surface atoms. Therefore, the signal of the surface ligand $Pb(OA)_2$ was counted entirely, while the signal from the inorganic part of the NCs was only counted partially. Additionally, the prepared $Pb(OA)_2$ contained unreacted oleic acid (~33% of the amount reacted),[34] which could also form Pb-OA bonds with subsurface Pb atoms.

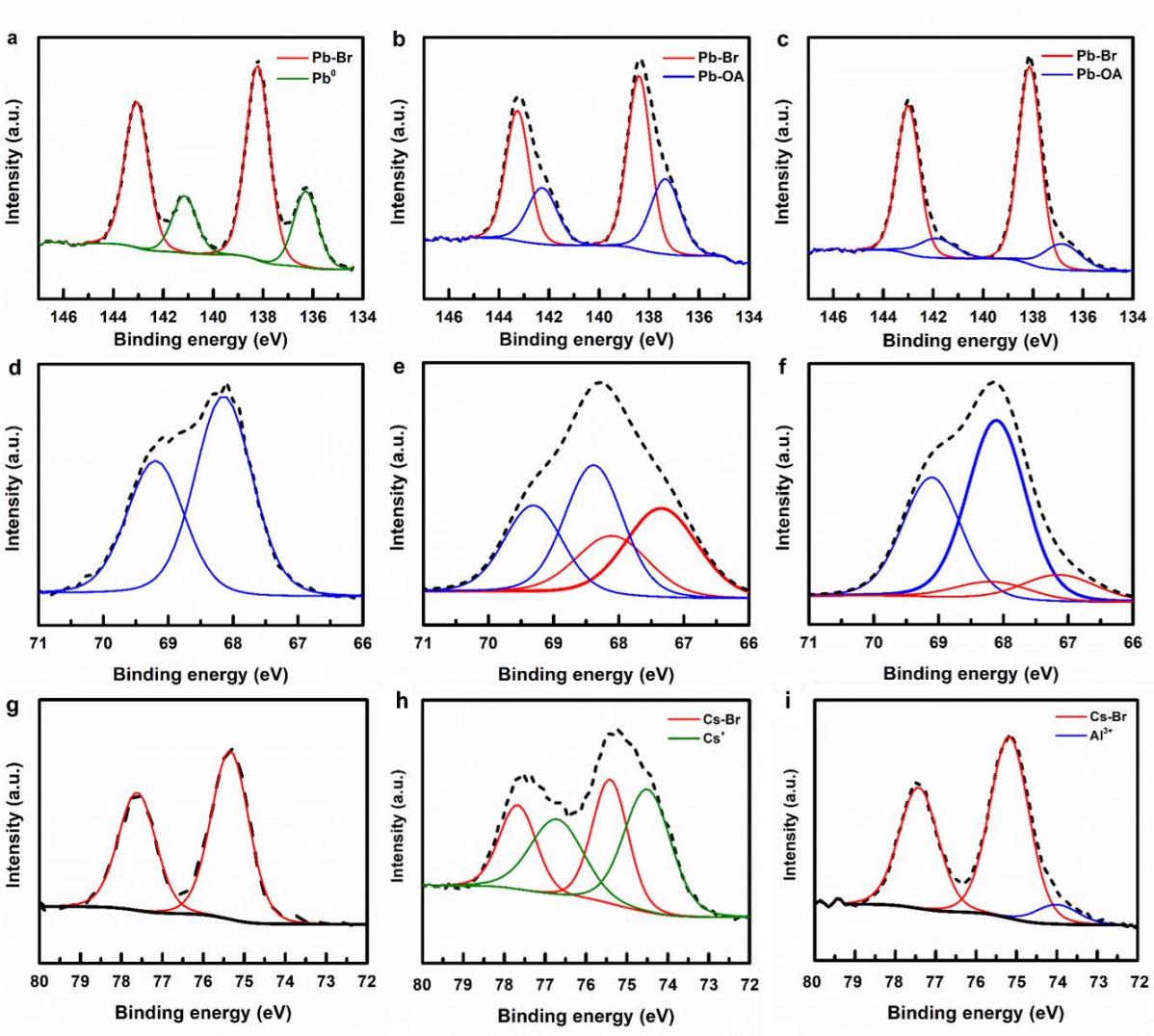

Figure 2.5. Pb 4f (a-c), Br 3d (d-f), and Cs 4d (g-i) XPS spectra of $CsPbBr_3$ core NCs (a, d, g), core NCs treated with $Pb(OA)_2$ (b, e, h), and core NCs treated with $Pb(OA)_2$ and then $AlBr_3$ (c, f, i).

Furthermore, the addition of $Pb(OA)_2$ resulted in the appearance of a new doublet (at 67.1 and 68.1 eV) in the Br 3d spectrum in addition to the one initially present at 68.1 and 69.1 eV (Figure 2.5d, e). This new downshifted doublet could be associated with surface Br^- ions close to $Pb(OA)_2$ molecules. The electrons of these ions experience an increased charge repulsion compared to those of bulk Br^- due to the electrons of $Pb(OA)_2$ (charge screening). Hence, they can be more easily ejected from the core levels under X-ray irradiation, represented by the lower binding energy observed in the spectrum. In Cs 4d spectra, the same behavior was observed with the downshifted doublet at 74.5 and 76.7 eV (Figure 2.55h).

The addition of $AlBr_3$ to the pretreated core NCs reduced the relative intensity of the Pb-OA doublet to the Pb-Br doublet from 51.2% to 22.0%, and slightly shifted it to lower binding energy (from 137.1 to 136.9 eV) (Figure 2.5c). Moreover, in Br 3d spectrum, the doublet at lower energy also reduced in intensity from 85.5% to 19.3% (Figure 4f). Moreover, in the Br 3d spectrum, the doublet at lower energy also reduced in intensity (Figure 2.5f), and an Al 2p peak corresponding to Al^{3+} was detected in the Cs 4d spectrum (Figure 2.5i). Taken together, the data imply that the effect of lead oleate on the Pb 4f and Br 3d spectra was reduced in the presence of $AlBr_3$. Two possible explanations can be given: $Pb(OA)_2$ complexes on the surface of $CsPbBr_3$ were partially replaced with $AlBr_3$, or the Pb–OA bond on the surface was substituted by a Pb–Br one. Overall, this analysis proves that lead oleate plays an important role in immobilizing $AlBr_3$ on the surface of the core NCs.

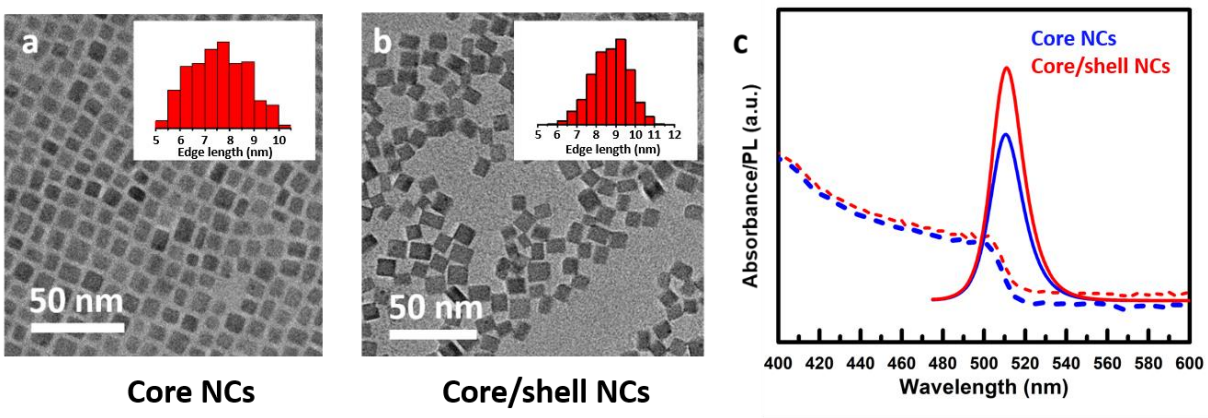

Figure 2.6. TEM images of a) core NCs, b) core/shell NCs, c) absorption (dashed lines) and emission (solid lines) spectra of the core and core/shell NCs.

After the shell growth, the NCs show an increase in size from 7.56 ± 1.12 nm to 8.71 ± 1.02 nm (Figure 2.6a, b). It is worth noting that the core NCs are tightly packed in an ordered fashion, while the core/shell NCs are less organized. As this organization is strongly related to the surface chemistry of the NCs, this low degree of ordering seen in Figure 2.6b could be due to the influence of the shell. The absorption spectra show no difference between the core and core/shell NCs. This is expected because the oxide shell is supposed to be both thin and amorphous, which does not exert as much strain on the lattice of the core NCs as in the usual cases of core/shell structures.[35] However, the shell is expected to help passivate the Br vacancies on the surface of the core NCs thanks to the use of the $AlBr_3$ precursor. We observed an increase of 1.4 times in the emission intensity of the core/shell NCs compared to the core, which can be explained by the aforementioned passivation effect.

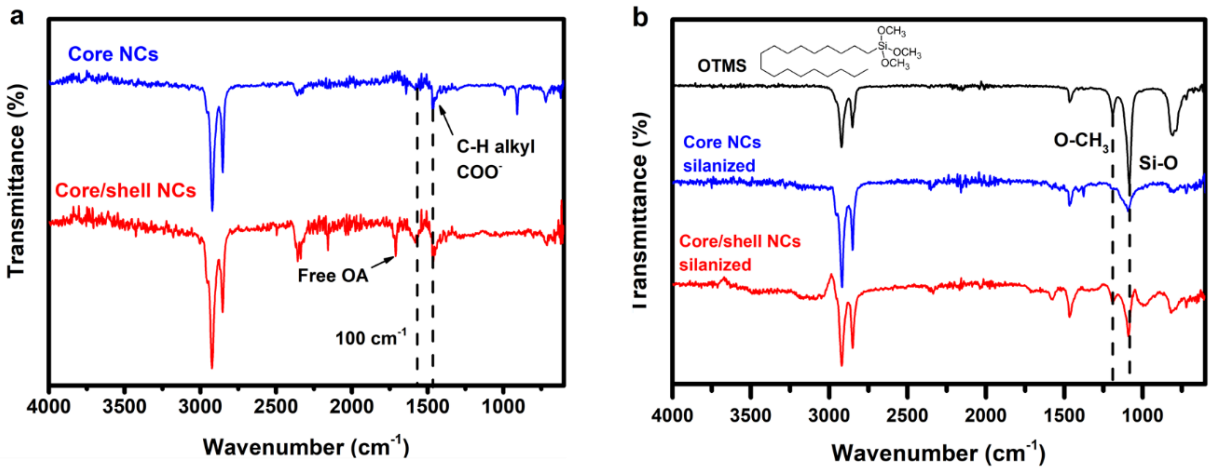

Figure 2.7. FTIR spectra of a) as-synthesized core and core/shell NCs, b) core and core/shell NCs after being treated with octadecyltrimethoxysilane (OTMS).

In Figure 2.7a, the FTIR spectra of core and core/shell NCs are presented. Below 1000 cm^{-1}),[36] no spectroscopic signal of the core/shell sample could be assigned to the vibration of the Al-O bond.[1] The only difference between the two samples is the strong presence of a peak at 1711 cm^{-1}, corresponding to the C=O vibration of free oleic acid molecules. This peak likely originated from the oleic acid residue in $Pb(OA)_2$.[34] To ascertain the presence of AlO_x in the core/shell NCs, we used the molecule octadecyltrimethoxysilane (OTMS) as a surface probe. When the molecule comes into contact with hydroxyl groups, it quickly reacts to form methanol and silanol groups, which can easily bind to oxygen-containing surfaces through a hydrolysis reaction. In this case, if the oxide shell is present, it would present an oxygen-rich surface and provide OTMS with hydroxyl groups, in contrast to core NCs, where the surface is made up of Cs^+ and Br^- ions. As shown in Figure 2.7b, the FTIR spectrum of pure OTMS displays the sharp characteristic peak of the methoxysilane Si–O vibration at 1085 cm^{-1}.[37] Upon interaction with the core/shell NCs, this peak shifted to 1091 cm^{-1}, while in the case of the core NCs, treated similarly, a small shoulder at ~1135 cm^{-1} appeared. This shoulder is likely the signal of silanol groups that underwent auto-condensation to form Si–O–Si bonds. The absence of such a shoulder in the case of the core/shell NCs can be interpreted that the OTMS molecules bound efficiently to the surface of the NCs, preventing them from cross-linking with each other.

The most important property of the $CsPbBr_3$/oxide core/shell structure is enhanced environmental stability. In the literature, there are several types of stability tests for core/shell LHP NCs. The most common one is bringing the NCs into contact with water.[3, 7, 9, 13] Ideally, the NCs should be completely dispersed in water to give the most reliable result. However, the core NCs already have an organic ligand shell surrounding them, and most of the core/shell NCs share the same characteristic. When introduced into water, the particles tend to aggregate, and particles inside this aggregate will receive better protection against water than if there are no aggregates. Thus, the stability of the system is improved, but not by having a shell. Another strategy involves creating a biphasic mixture of water and the dispersion of NCs in organic solvent, which can avoid the problem of NCs dispersibility.[12-13] But the interaction of NCs with water is also dictated by the interface between the organic solvent and water, further complicating the test. Therefore, the results from these studies are difficult to quantify and to compare between different publications.

Another type of test involves monitoring the PL of the NCs under continuous illumination, for example with UV light.[38] As LHP NCs are mostly used in optical devices, including single photon emitters, moisture is less of an issue thanks to the encapsulation provided during the device fabrication. Nonetheless, the ability of core/shell structures to better resist against light-induced damages is highly valuable. Practically, the NCs are deposited as a thin film for the test. Using different deposition methods (e.g., spin- or dip-coating), the density and thickness of the film can be easily controlled, giving a clearer view over the particle–particle interactions. The parameter irradiation power on a given sample surface can also be standardized, allowing better comparison between different works. Due to these advantages, we decided to perform the stability test on core and core/shell NCs deposited on silicon substrates.

We first investigated the effect of the environment on the photostability of the core NCs by performing the test under vacuum and at 1 bar (Figure 2.8a). It can be seen that oxygen and moisture did not play as important a role as the irradiation in degrading $CsPbBr_3$ NCs. This observation is further corroborated by the measurements on core/shell NCs (Figure 2.8b and c). Furthermore, in all cases, no visible enhancement in stability can be seen for the core/shell NCs. The result of this measurement questions about the passivation effect of the shell. The shell was expected to be a monolayer, which realistically would mean a submonolayer. At this level of thickness, the AlO_x shell would not be able to fully passivate the surface, leading to the observed lack of photostability enhancement.

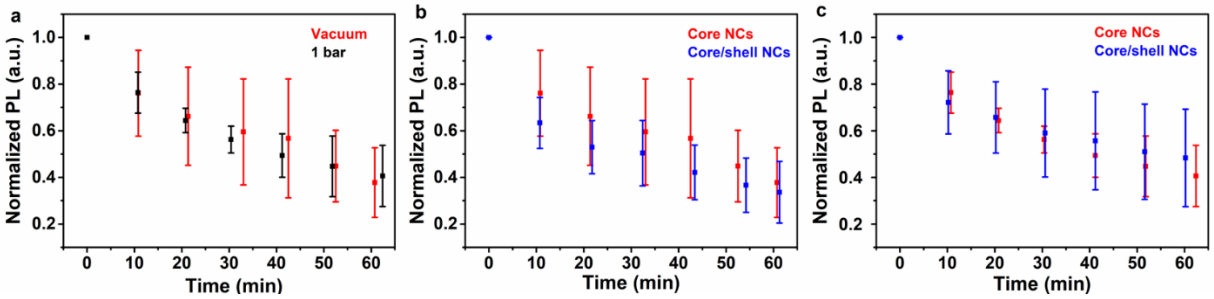

Figure 2.8. Photostability tests of core and core/shell NCs under different conditions: a) Core NCs, under vacuum and at 1 bar; b) core and core/shell NCs under vacuum; c) core and core/shell NCs at 1 bar.

The measurements were also subject to varying margins of error, obtained by averaging over 3 random points on each sample. The standard deviation typically ranges from 20% to 40% of the mean value, and in some cases, the error varies with irradiation time. We hypothesize that the thickness of the film is an important cause of this complication. Typically, the nanocrystal films for this test were obtained by spin coating, with a thickness in the range of tens of nm (determined by reflectometry). This translates to several layers of NCs, as the size of each nanocrystal combined with the gap between them is ~10 nm. At this thickness and compactness, the topmost layer can protect those below from oxygen and moisture penetration even after it has been degraded, which probably explains the insensitivity of the film to the presence of air.

In summary, we treated the surface of $CsPbBr_3$ core NCs with $Pb(OA)_2$ molecules before growing the AlO_x shell by reacting $AlBr_3$ with $Al(IPA)_3$. The XPS spectra supported that $Pb(OA)_2$ facilitates the anchoring of $AlBr_3$ on the core NCs, which was essential for forming the shell. Characterizations by FTIR also showed indications of the presence of the AlO_x shell. However, the amount of shell deposited was too low to be detectable with FTIR, and the photostability of the $CsPbBr_3$ NCs did not improve

after the shell growth. Despite further optimizations required for the test itself, it is safe to conclude that the treatment with $Pb(OA)_2$ followed by $AlBr_3$ and $Al(IPA)_3$ does not yield an oxide shell of sufficient thickness and/or homogeneity to passivate the core NCs. Considering the ineffectiveness of the shell growth process, we decided not to grow a thicker shell with this method and instead focus on another method in which $AlBr_3/CH_2Br_2$ was used in place of $Pb(OA)_2$ as a primer for the NC surface.

Core/shell synthesis with $AlBr_3/CH_2Br_2$

In a separate study, we found that $AlBr_3$ dissolved in toluene did not bind to the $CsPbBr_3$ NCs, while dissolved in dibromomethane (DBM, CH_2Br_2), it quickly doped Al^{3+} into the perovskite lattice. Doping results in NCs showing a blue-shifted emission spectrum and slightly reduced PLQY. This effect will be further elaborated on in Chapter 4. For now, the effect means that $AlBr_3$/DBM can be used to bind $AlBr_3$ to the surface of $CsPbBr_3$ for the eventual shelling. However, because $AlBr_3$ would quickly diffuse into the core NCs instead of staying on the surface, the sequential introduction of $AlBr_3$ followed by $Al(IPA)_3$ would not be possible. Therefore, we decided to inject the two precursors at the same time. Despite of this strategy, the emission of the NCs still blueshifted with the addition of the precursors (Figure 2.9a). This trend only stopped when no more $AlBr_3$ was introduced, but the QY still reduced to 40.2% after 3 hours and continued to decrease in the last hour to 21.5%. The shell, if it was formed, protected the core poorly as it did not stop Al^{3+} from incorporating into $CsPbBr_3$ and shifting the emission.

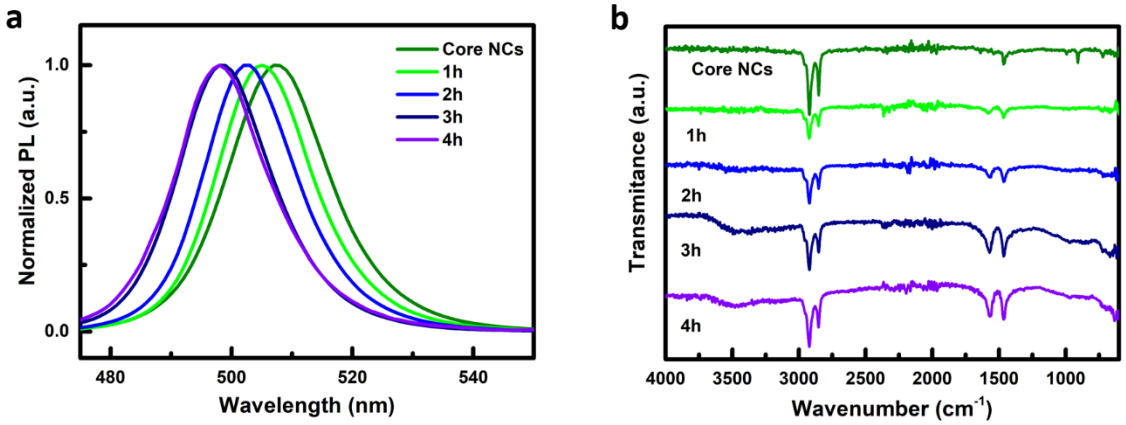

Figure 2.9. Photoluminescence spectra (a) and FTIR spectra (b) of core/shell NCs synthesized using $AlBr_3$/DBM and $Al(IPA)_3$ as precursors.

The FTIR spectrum of the supposed core/shell NCs presents several distinct features compared to the core NCs (Figure 2.9b). First, several broad peaks appear below 1000 cm^{-1} that are enhanced with prolonged reaction time. These peaks can be attributed to the vibrations of Al–O bonds.[1] Above 3000 cm^{-1}, peaks corresponding to the stretching of hydroxyl groups can be observed as well. The broadness of these peaks can be explained by considering the amorphous nature of AlO_x: due to the short-range order, the vibration energy of Al–O and O–H bonds will experience local variations, which results in the broadening of the observed peaks in the spectrum. Finally, a doublet at 1569 cm^{-1} and 1458 cm^{-1} appears. It has been known that the oleate has several coordination modes to metal cations, and each mode would have its signature peak(s) in FTIR.[34] In our case, the peak-to-peak separation accounts for approximately 100 cm^{-1}, indicating that the binding motif is either chelating,[1] or bridging with a hydroxyl-poor surface.[39] It is noteworthy that without oleic acid addition during the shell growth, the resulting nanocrystals possess poor colloidal stability and readily precipitate.

As using $AlBr_3$/DBM as the sole precursor for the core NC surface treatment prior to the shell growth was not sufficient, we used a mixture of $AlBr_3$/toluene and $AlBr_3$/DBM with the idea that due to the lower concentration of $AlBr_3$/DBM in the reaction medium, the diffusion rate is reduced. TEM images of the core and core/shell NCs are shown in Figure 2.10a and b. The core NCs have a size of 7.6 ± 1.2 nm, which increases to 10.1 ± 0.9 nm upon shell growth. However, the Al/Pb ratio determined by ICP/AES was only 0.35, which corresponds to roughly one monolayer of AlO_x (more details will be given below). Therefore, the observed size increase cannot be fully attributed to the shell addition, but to a large extent to the ripening of the core particles during the shell growth. The UV-vis and PL spectra display no discernable difference between the two samples (Figure 2.10c). This is strong evidence that Al^{3+} was not incorporated into $CsPbBr_3$, otherwise, the spectra would have blueshifted (vide supra). Additionally, we recorded an enhancement of the photoluminescence intensity of the NCs, with the PLQY of the core increasing from 84.5% to 94.1% upon AlO_x shelling. The FTIR spectrum of the core/shell NCs shows the expected signals of AlO_x, similar to the previous experiment.

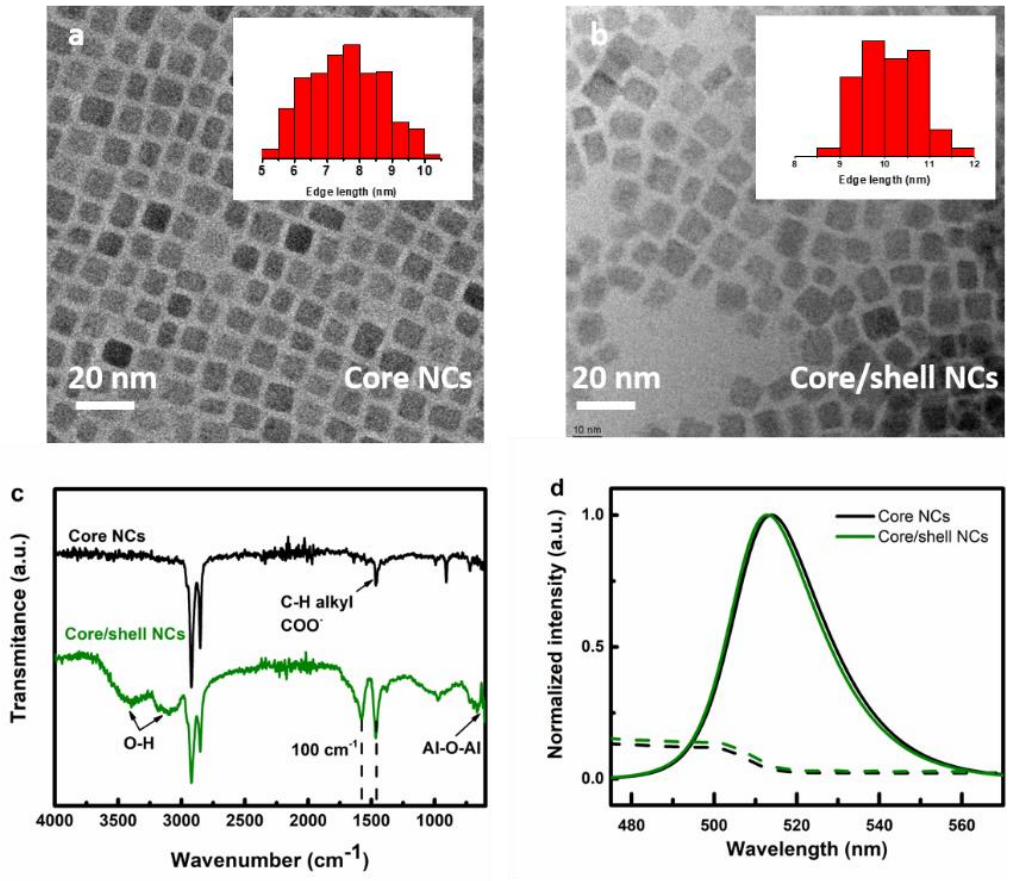

Figure 2.10. TEM images (a,b), infrared spectra (c), absorption and photoluminescence spectra (d) of the core and core/shell NCs using a mixed precursor of $AlBr_3$/DBM and $AlBr_3$/toluene and $Al(IPA)_3$ during the shell synthesis.

We next investigated the ratio of the two $AlBr_3$ precursors to find the optimized conditions. The $AlBr_3$/DBM : $AlBr_3$/toluene molar ratio was varied from 1/8 over 1/4 to 1/1. The FTIR spectra show that all core/shell samples display the peaks characteristic for the presence of AlO_x (Figure 2.11a). The photoluminescence spectra, on the other hand, reveal distinct differences depending on the ratio (Figure 2.11b). In all cases, no blue-shift was observed for the core/shell NCs produced using the mixture, as opposed to the case where only $AlBr_3$/DBM was used. This is a clear sign of the suppression

of Al^{3+} diffusion and doping of the $CsPbBr_3$ core. On the contrary, for the 1/1 ratio a red-shift of 2 nm is observed, which is attributed to the core particles increasing in size. Furthermore, the PLQY improved when the ratios of 1/4 and 1/1 were used, reaching 94.7% and 94.1%, respectively. This contrasts with the ratio of 1/8, which yielded only 60% QY.

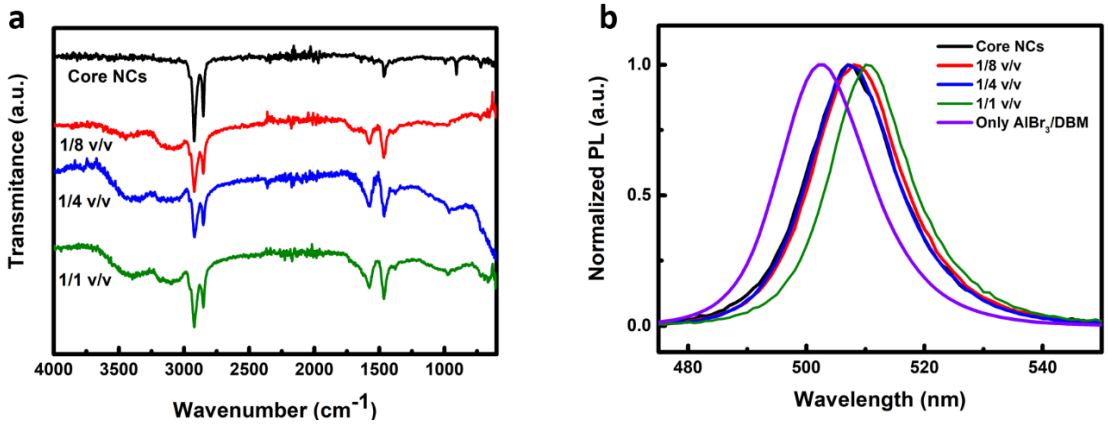

Figure 2.11. FTIR (a) and photoluminescence spectra (b) of core/shell NCs synthesized using mixtures of $AlBr_3$/DBM and $AlBr_3$/toluene with varying molar ratios as the precursor during the shell growth.

These differences can be understood when comparing the morphology of the NCs after shell growth. Several large rectangular structures can be seen alongside core/shell NCs when the ratio of 1/8 was used (Figure 2.12b). At this ratio, the high amount of $AlBr_3$/toluene likely caused uncontrollable growth of AlO_x, forming excess alcohol that damaged the ligand shell of the core NCs. These damaged NCs then aggregated and grew into the larger structures observed in SEM, explaining their rectangular shape and the lower overall QY of the sample. On the contrary, with 1/4 and 1/1 ratios, the reaction rate possibly decreased, creating less alcohol and keeping the integrity of the core NCs. The core/shell NCs obtained with these conditions do not show the presence of large aggregates (Figure 2.12c, d).

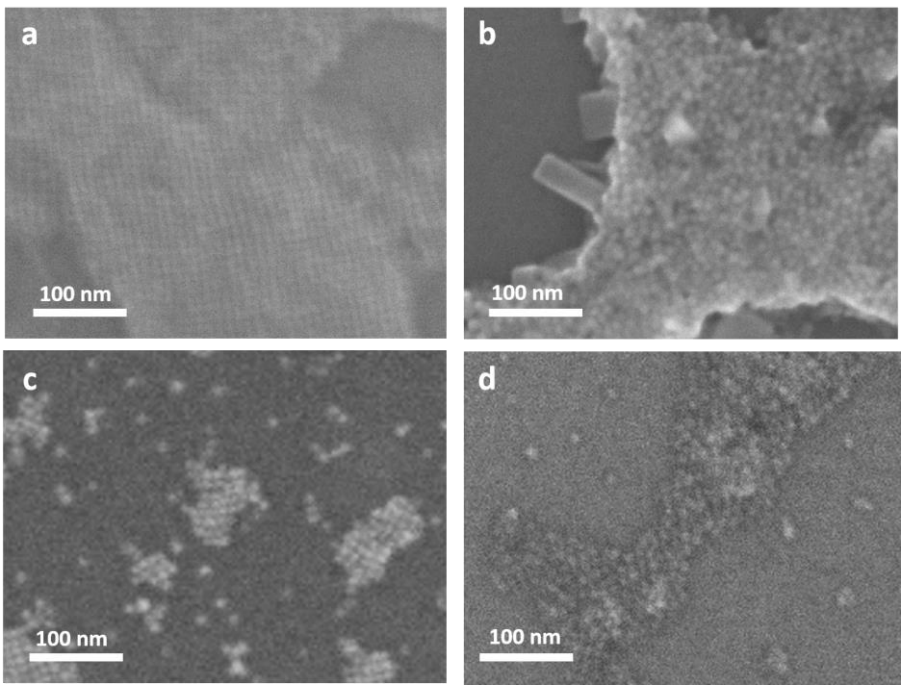

Figure 2.12. SEM images of the core NCs (a) and core/shell NCs synthesized using mixtures of $AlBr_3$/DBM and $AlBr_3$/toluene with varying molar ratios: 1/8 (b), 1/4 (c), and 1/1 (d).

One important aspect of core/shell NCs syntheses in general is the ability to control the thickness of the shell, as it ties directly to the optical properties and stability of the NCs.[35] Elemental analysis by ICP-AES shows an Al/Pb ratio of 0.3-0.4. From the average core NCs size obtained by TEM and the $CsPbBr_3$ lattice parameter (assumed to be cubic for the ease of calculation), we can estimate that the ratio $Pb_{surface}/Pb_{total}$ is 0.44, which means that there is roughly one Al atom per surface Pb atom, and the shell is therefore estimated to be a submonolayer (assuming the shell is cubic Al_2O_3 with a = 8.98 Å). This thickness is much lower than the value expected from the amount of shell precursors used, indicating that nearly 90% of them were not deposited. We then tried to grow a thicker shell by increasing the reaction time to 4 hours. After the reaction, the product still showed green luminescence, but the colloidal stability degraded. Further inspection by SEM reveals that large aggregates have appeared alongside the core/shell NCs (Figure 2.13a). The excess of unreacted precursors seemed to have triggered homogeneous AlO_x growth with prolonged reaction time. As a consequence, the core/shell NCs were first purified before an additional shell growth step was attempted. We managed to avoid uncontrollable AlO_x growth (Figure 2.13c, d), and the Al/Pb ratio increased to 1.75 after this step, corresponding to a shell thickness of ~2.4 nm.

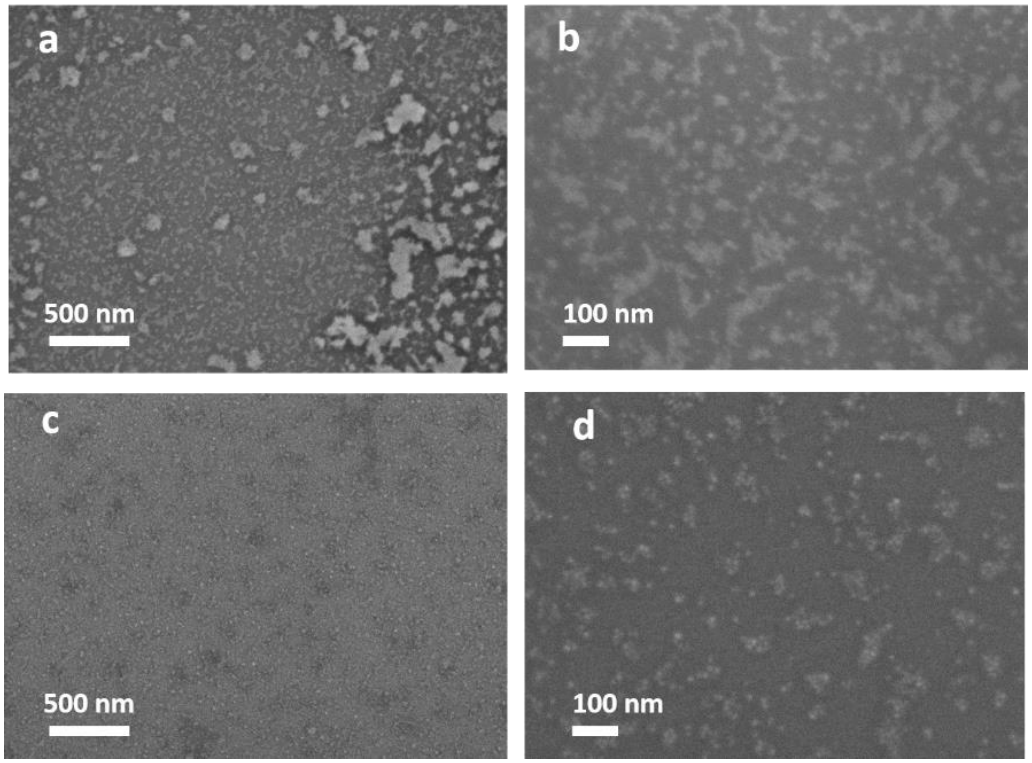

Figure 2.13. SEM images of the core/thick shell NCs synthesized without (a, b) and with (c, d) prior purification of the core/thin shell NCs.

TEM measurement demonstrates that the core/thick shell NCs have similar size to core/thin shell NCs (10 ± 0.87 nm and 10.1 ± 0.9 nm, respectively) (Figure 2.14a, b). On one hand, we could not observe the increase in shell thickness previously estimated from the elemental analysis. As the shell is made from light elements while the core consists of heavy metals, the strong contrast in the TEM image prevents the thin shell from being resolved. This can also explain the failure to distinguish the AlO_x shell in previous works.[1,13] On the other hand, the similar sizes is the evidence that the increase in size after shell growth is caused by particle ripening. During the formation of the thin shell, the interaction between $AlBr_3$ and the surface of $CsPbBr_3$ NCs likely triggered the size defocused growth of the core

NCs. However, once the thin shell was formed, the surface of the core NCs is passivated, leading to no further particle growth. In terms of optical properties, the thick shell does not cause any shift in the emission spectrum of the core NCs (Figure 2.14c).

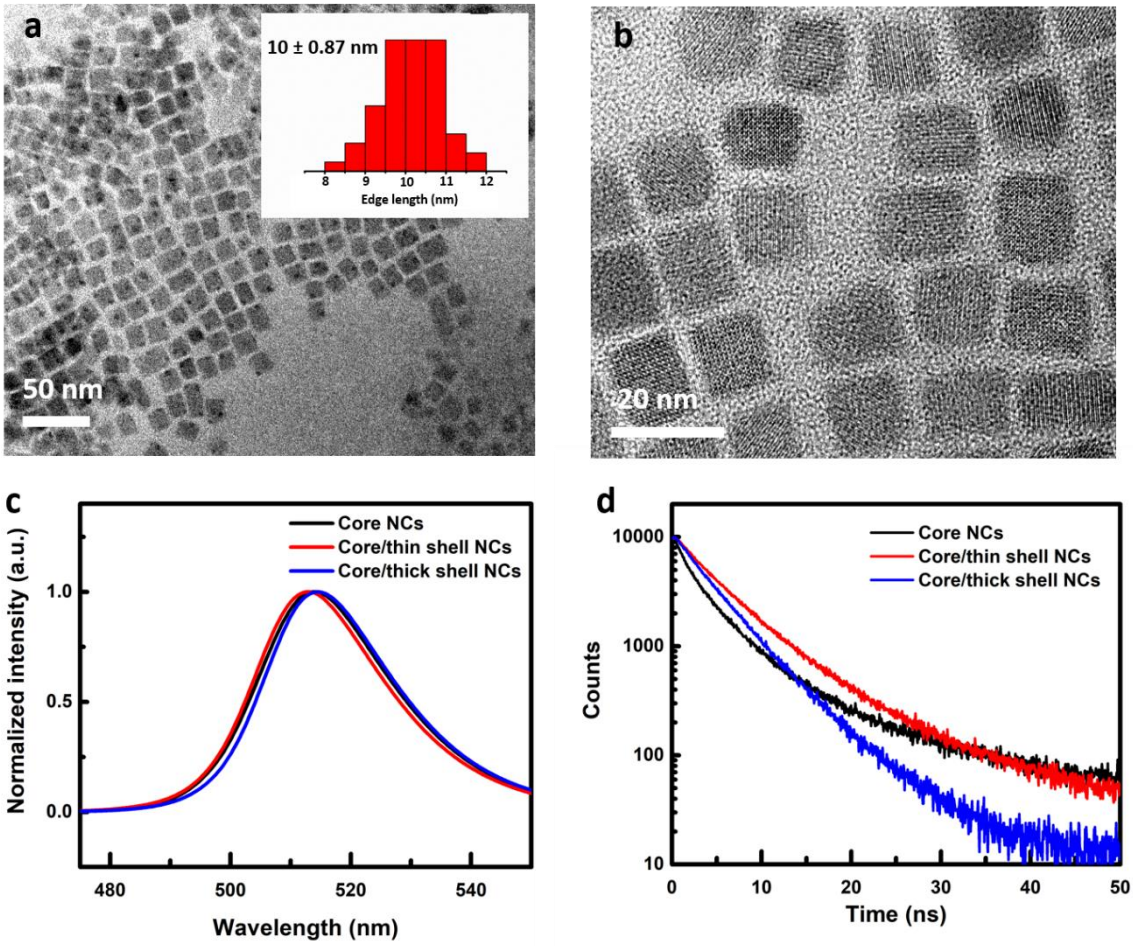

Figure 2.14. a, b) TEM images of the core/thick shell NCs, including the size distribution (inset), c) PL emission spectra and d) PL decay curves of the core and the core/shell NCs with different thicknesses.

As mentioned above, the shell growth altered the surface of the core NCs, leading to particle growth. This process could potentially form surface defects, which are detriment to the optical properties of the NCs. Therefore, time-resolved photoluminescence study was performed to assess the change in carrier dynamics of the system (Figure 2.14d). The luminescence decay curve of core NCs features two components with lifetimes of 1.80 ns (91%) and 10.0 ns (9%), with the numbers in parentheses indicating their relative amplitudes. If surface defects formed during the shell growth, the contribution of the slow component would increase in the core/shell NCs. Fortunately, we observed no such change in the slow component. It remained mostly similar, 11.0 ns (10%) and 9.70 ns (10%) for thin and thick shells, respectively. The only difference was that the fast component lifetimes increased to 3.70 ns (90%) for both types of shell. The increase in excited state lifetime of free carriers has been attributed to the effective suppression of surface defects in a number of studies,[21, 24, 40] especially in the work on AlO_x shell grown by colloidal atomic layer deposition by Loiudice et al.[13]

Having obtained a thick shell surrounding the $CsPbBr_3$ NCs, we were interested in investigating whether the thickness of the shell can affect the crystalline properties of the core NCs (Figure 2.15).

Overall, the diffractograms of the core and core/shell NCs are similar as the amorphous shell does not produce any additional diffraction peaks. Nonetheless, the influence of the shell can still be observed by the strain it imposes on the surface of the core NCs, resulting in lattice contraction or expansion. Typically, these effects can be seen from a change in the strain-induced broadening of the diffraction peaks, as well as a direct change in the lattice parameter, though this change is harder to spot. The broadening of the peaks is consistent for the three types of nanocrystals. Le Bail refinement of the $CsPbBr_3$ Pbnm orthorhombic structure was performed to determine the lattice parameters of the core and core/shell NCs. The result shows that they have comparable lattice parameters, within the margin of error (Table 2.1). It confirms that even with a thicker shell, AlO_x still does not exert strain on the core NCs.

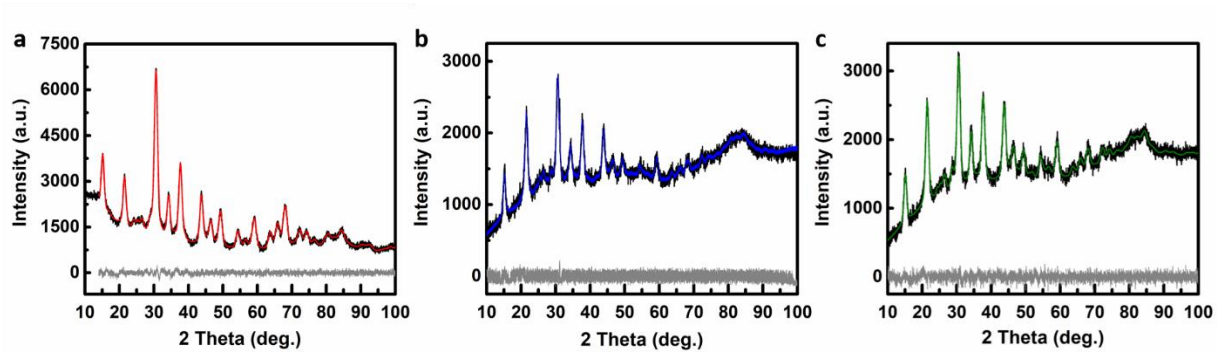

Figure 2.15. XRD patterns (black) and Le Bail refinement results (colored) of core NCs (a), core/thin shell NCs (b), and core/thick shell NCs (c). (In gray: residual intensity)

Table 2.1. Lattice parameters obtained by Le Bail refinement of the $CsPbBr_3$ Pbnm orthorhombic structure for the core and core/shell NCs:

Types of nanocrystals	a (Å)	b (Å)	c (Å)
Core	8.12(8)	8.29(1)	11.69(1)
Core/thin shell	8.13(4)	8.28(3)	11.69(1)
Core/thick shell	8.11(8)	8.26(3)	11.67(2)

To assess the passivation effect of the thick shell, we performed a photostability test on thin films of core and core/shell NCs. Taking the previous measurements into consideration, we controlled the concentration of the NCs to obtain a film with a single layer (Figure 2.16a). In the SEM images, the NCs exist as clusters instead of a complete layer, which would profit the test more due to the increased surface for interaction with the environment. The test was done directly in air. In these conditions, it was found that the laser power density used previously quickly degraded the particles, reducing the PL intensity to almost zero within a few minutes of exposure. This fact further emphasizes the effect of interparticle interaction and layer thickness on the stability of the sample. To be able to track the degradation of the film, we reduced the power density from ~1100 W/cm^2 to 154 W/cm^2. We observed that the PL intensity of all the spots investigated decayed in a near-exponential manner (Figure 2.16b). Despite our effort to minimize interparticle interaction, the margin of error for this measurement is still 20-40% of the mean value. This could mean that either the different morphologies of the obtained NC clusters lead to a different passivation behavior, or that there are still other factors unaccounted

for. Nevertheless, within the margin of error, the core/shell structure demonstrated unambiguously an enhanced photostability. The PL intensity of the core NCs dropped to about 17% of the initial value after 30 min of irradiation, whereas that of the core/shell NCs retained 44%. Even after 1 hour, the PL value of the core/shell NCs was still higher than that of the core NCs at 30 minutes.

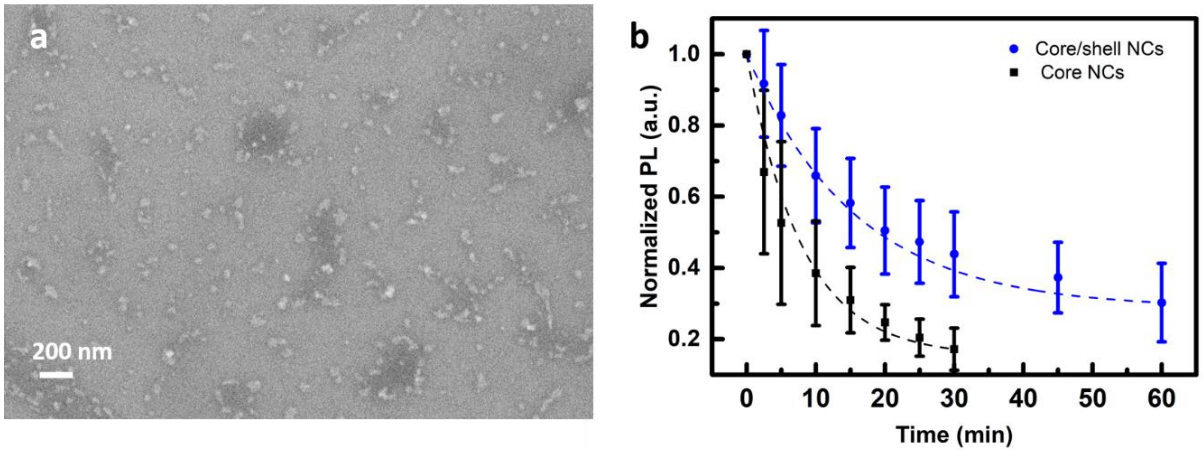

Figure 2.16. a) Typical SEM image of a nanocrystal film used for the photostability test, b) Comparison of the photostability of the core and core/shell NCs.

Conclusion

$CsPbBr_3$ nanocrystals were synthesized by a hot-injection method using three precursors instead of the common method where lead bromide was used as the common precursor for both lead and bromine. The synthesized core NCs possess identical structural as well as optical properties as the ones in the literature. We then grew an AlO_x shell on the core NCs by a non-hydrolytic sol-gel reaction at room temperature, using two approaches to anchor the aluminum precursor on the surface of the core. First, we treated the surface of the core NCs with $Pb(OA)_2$ before sequentially adding the aluminum precursors ($AlBr_3$/$Al(IPA)_3$). While this method proved to be effective in binding the $AlBr_3$ precursor on the core NCs, it ultimately failed to produce a complete AlO_x layer capable of enhancing the photostability of the NCs. In the second approach, we employed a mixture of $AlBr_3$ dissolved in toluene and CH_2Br_2 as the primary aluminum precursor. Despite no direct proof of the AlO_x shell grown on top of the $CsPbBr_3$ core, indirect evidence suggests that the shell was indeed formed and improved the optical properties of the $CsPbBr_3$ NCs. The PLQY increased up to 94.1% along with an increase in the photoluminescence lifetime, both being the result of efficient surface defect passivation. In addition, we optimized the synthesis of the shell to produce a thicker AlO_x shell, demonstrating the ability to control the shell thickness using this synthetic route. With this thick shell compared to the core-only NCs, the core/shell NCs possess a significantly enhanced photostability at the single particle level under 405 nm laser irradiation.

References

1. Segura Lecina, O.; Hope, M. A.; Venkatesh, A.; Bjorgvinsdottir, S.; Rossi, K.; Loiudice, A.; Emsley, L.; Buonsanti, R., Colloidal-ALD-Grown Hybrid Shells Nucleate via a Ligand-Precursor Complex. *J. Am. Chem. Soc.* **2022,** *144* (9), 3998-4008.

2. Tang, X.; Yang, J.; Li, S.; Chen, W.; Hu, Z.; Qiu, J., CsPbBr3/CdS Core/Shell Structure Quantum Dots for Inverted Light-Emitting Diodes Application. *Frontiers in chemistry* **2019,** *7*, 499.

3. Ravi, V. K.; Saikia, S.; Yadav, S.; Nawale, V. V.; Nag, A., CsPbBr3/ZnS Core/Shell Type Nanocrystals for Enhancing Luminescence Lifetime and Water Stability. *Acs Energy Lett* **2020,** *5* (6), 1794-1796.
4. Jia, C.; Li, H.; Meng, X.; Li, H., CsPbX3/Cs4PbX6 core/shell perovskite nanocrystals. *Chem Commun (Camb)* **2018,** *54* (49), 6300-6303.
5. Qiu, L.; Yang, H.; Dai, Z.; Sun, F.; Hao, J.; Guan, M.; Dang, P.; Yan, C.; Lin, J.; Li, G., Highly Efficient and Stable CsPbBr3 Perovskite Quantum Dots by Encapsulating in Dual-Shell Hollow Silica Spheres for WLEDs. *Inorganic Chemistry Frontiers* **2020**.
6. Bhaumik, S.; Veldhuis, S. A.; Ng, Y. F.; Li, M.; Muduli, S. K.; Sum, T. C.; Damodaran, B.; Mhaisalkar, S.; Mathews, N., Highly stable, luminescent core-shell type methylammonium-octylammonium lead bromide layered perovskite nanoparticles. *Chem Commun (Camb)* **2016,** *52* (44), 7118-21.
7. Zhong, Q.; Cao, M.; Hu, H.; Yang, D.; Chen, M.; Li, P.; Wu, L.; Zhang, Q., One-Pot Synthesis of Highly Stable CsPbBr3@SiO2 Core-Shell Nanoparticles. *ACS nano* **2018,** *12* (8), 8579-8587.
8. Wang, S.; Bi, C.; Yuan, J.; Zhang, L.; Tian, J., Original Core–Shell Structure of Cubic CsPbBr3@Amorphous CsPbBrx Perovskite Quantum Dots with a High Blue Photoluminescence Quantum Yield of over 80%. *Acs Energy Lett* **2017,** *3* (1), 245-251.
9. Li, Z.-J.; Hofman, E.; Li, J.; Davis, A. H.; Tung, C.-H.; Wu, L.-Z.; Zheng, W., Photoelectrochemically Active and Environmentally Stable CsPbBr3/TiO2 Core/Shell Nanocrystals. *Adv. Funct. Mater.* **2018,** *28* (1), 1704288.
10. Wang, B.; Zhang, C.; Huang, S.; Li, Z.; Kong, L.; Jin, L.; Wang, J.; Wu, K.; Li, L., Postsynthesis Phase Transformation for CsPbBr3/Rb4PbBr6 Core/Shell Nanocrystals with Exceptional Photostability. *ACS applied materials & interfaces* **2018,** *10* (27), 23303-23310.
11. Tang, X.; Yang, J.; Li, S.; Liu, Z.; Hu, Z.; Hao, J.; Du, J.; Leng, Y.; Qin, H.; Lin, X.; Lin, Y.; Tian, Y.; Zhou, M.; Xiong, Q., Single Halide Perovskite/Semiconductor Core/Shell Quantum Dots with Ultrastability and Nonblinking Properties. *Advanced science* **2019,** *6* (18), 1900412.
12. Wang, B.; Zhang, S.; Liu, B.; Li, J.; Cao, B.; Liu, Z., Stable CsPbBr3:Sn@SiO2 and Cs4PbBr6:Sn@SiO2 Core–Shell Quantum Dots with Tunable Color Emission for Light-Emitting Diodes. *ACS Applied Nano Materials* **2020,** *3* (3), 3019-3027.
13. Loiudice, A.; Strach, M.; Saris, S.; Chernyshov, D.; Buonsanti, R., Universal Oxide Shell Growth Enables in Situ Structural Studies of Perovskite Nanocrystals during the Anion Exchange Reaction. *J. Am. Chem. Soc.* **2019,** *141* (20), 8254-8263.
14. Song, W.; Wang, Y.; Wang, B.; Yao, Y.; Wang, W.; Wu, J.; Shen, Q.; Luo, W.; Zou, Z., Super stable CsPbBr3@SiO2 tumor imaging reagent by stress-response encapsulation. *Nano Research* **2020,** *13* (3), 795-801.
15. Imran, M.; Caligiuri, V.; Wang, M.; Goldoni, L.; Prato, M.; Krahne, R.; De Trizio, L.; Manna, L., Benzoyl Halides as Alternative Precursors for the Colloidal Synthesis of Lead-Based Halide Perovskite Nanocrystals. *J. Am. Chem. Soc.* **2018,** *140* (7), 2656-2664.
16. De Roo, J.; Ibanez, M.; Geiregat, P.; Nedelcu, G.; Walravens, W.; Maes, J.; Martins, J. C.; Van Driessche, I.; Kovalenko, M. V.; Hens, Z., Highly Dynamic Ligand Binding and Light Absorption Coefficient of Cesium Lead Bromide Perovskite Nanocrystals. *ACS nano* **2016,** *10* (2), 2071-81.
17. Maes, J.; Balcaen, L.; Drijvers, E.; Zhao, Q.; De Roo, J.; Vantomme, A.; Vanhaecke, F.; Geiregat, P.; Hens, Z., Light Absorption Coefficient of CsPbBr3 Perovskite Nanocrystals. *The journal of physical chemistry letters* **2018,** *9* (11), 3093-3097.
18. Ruan, L. J.; Tang, B.; Shu, A.; Qin, C.; Ma, Y., Self-Passivation of CsPbBr3 Nanocrystals through Introducing Bromide Vacancies and Ultraviolet Irradiation. *The Journal of Physical Chemistry C* **2020,** *125* (1), 1010-1017.
19. Acosta, S.; Corriu, R. J. P.; Leclercq, D.; Lefèvre, P.; Mutin, P. H.; Vioux, A., Preparation of alumina gels by a non-hydrolytic sol-gel processing method. *J. Non-Cryst. Solids* **1994,** *170* (3), 234-242.

20. Protesescu, L.; Yakunin, S.; Bodnarchuk, M. I.; Krieg, F.; Caputo, R.; Hendon, C. H.; Yang, R. X.; Walsh, A.; Kovalenko, M. V., Nanocrystals of Cesium Lead Halide Perovskites (CsPbX(3), X = Cl, Br, and I): Novel Optoelectronic Materials Showing Bright Emission with Wide Color Gamut. *Nano Lett.* **2015,** *15* (6), 3692-6.
21. Bodnarchuk, M. I.; Boehme, S. C.; Ten Brinck, S.; Bernasconi, C.; Shynkarenko, Y.; Krieg, F.; Widmer, R.; Aeschlimann, B.; Gunther, D.; Kovalenko, M. V.; Infante, I., Rationalizing and Controlling the Surface Structure and Electronic Passivation of Cesium Lead Halide Nanocrystals. *Acs Energy Lett* **2019,** *4* (1), 63-74.
22. Lu, C.; Wright, M. W.; Ma, X.; Li, H.; Itanze, D. S.; Carter, J. A.; Hewitt, C. A.; Donati, G. L.; Carroll, D. L.; Lundin, P. M.; Geyer, S. M., Cesium Oleate Precursor Preparation for Lead Halide Perovskite Nanocrystal Synthesis: The Influence of Excess Oleic Acid on Achieving Solubility, Conversion, and Reproducibility. *Chem. Mater.* **2018,** *31* (1), 62-67.
23. Dey, A.; Rathod, P.; Kabra, D., Role of Localized States in Photoluminescence Dynamics of High Optical Gain CsPbBr3Nanocrystals. *Advanced Optical Materials* **2018,** *6* (11), 1800109.
24. Nenon, D. P.; Pressler, K.; Kang, J.; Koscher, B. A.; Olshansky, J. H.; Osowiecki, W. T.; Koc, M. A.; Wang, L. W.; Alivisatos, A. P., Design Principles for Trap-Free CsPbX3 Nanocrystals: Enumerating and Eliminating Surface Halide Vacancies with Softer Lewis Bases. *J. Am. Chem. Soc.* **2018,** *140* (50), 17760-17772.
25. Raino, G.; Nedelcu, G.; Protesescu, L.; Bodnarchuk, M. I.; Kovalenko, M. V.; Mahrt, R. F.; Stoferle, T., Single Cesium Lead Halide Perovskite Nanocrystals at Low Temperature: Fast Single-Photon Emission, Reduced Blinking, and Exciton Fine Structure. *ACS nano* **2016,** *10* (2), 2485-90.
26. Rudin, S.; Reinecke, T. L.; Segall, B., Temperature-dependent exciton linewidths in semiconductors. *Physical review. B, Condensed matter* **1990,** *42* (17), 11218-11231.
27. Iaru, C. M.; Geuchies, J. J.; Koenraad, P. M.; Vanmaekelbergh, D.; Silov, A. Y., Strong Carrier-Phonon Coupling in Lead Halide Perovskite Nanocrystals. *ACS nano* **2017,** *11* (11), 11024-11030.
28. Ramade, J.; Andriambariarijaona, L. M.; Steinmetz, V.; Goubet, N.; Legrand, L.; Barisien, T.; Bernardot, F.; Testelin, C.; Lhuillier, E.; Bramati, A.; Chamarro, M., Exciton-phonon coupling in a CsPbBr3 single nanocrystal. *Appl. Phys. Lett.* **2018,** *112* (7), 072104.
29. Miyata, K.; Meggiolaro, D.; Trinh, M. T.; Joshi, P. P.; Mosconi, E.; Jones, S. C.; De Angelis, F.; Zhu, X. Y., Large polarons in lead halide perovskites. *Science advances* **2017,** *3* (8), e1701217.
30. van der Stam, W.; Geuchies, J. J.; Altantzis, T.; van den Bos, K. H.; Meeldijk, J. D.; Van Aert, S.; Bals, S.; Vanmaekelbergh, D.; de Mello Donega, C., Highly Emissive Divalent-Ion-Doped Colloidal CsPb1-xMxBr3 Perovskite Nanocrystals through Cation Exchange. *J. Am. Chem. Soc.* **2017,** *139* (11), 4087-4097.
31. Pederson, L. R., Two-dimensional chemical-state plot for lead using XPS. *J. Electron. Spectrosc. Relat. Phenom.* **1982,** *28* (2), 203-209.
32. Svanstrom, S.; Garcia Fernandez, A.; Sloboda, T.; Jacobsson, T. J.; Rensmo, H.; Cappel, U. B., X-ray stability and degradation mechanism of lead halide perovskites and lead halides. *Phys. Chem. Chem. Phys.* **2021,** *23* (21), 12479-12489.
33. McGettrick, J. D.; Hooper, K.; Pockett, A.; Baker, J.; Troughton, J.; Carnie, M.; Watson, T., Sources of Pb(0) artefacts during XPS analysis of lead halide perovskites. *Mater. Lett.* **2019,** *251*, 98-101.
34. Cass, L. C.; Malicki, M.; Weiss, E. A., The chemical environments of oleate species within samples of oleate-coated PbS quantum dots. *Anal. Chem.* **2013,** *85* (14), 6974-9.
35. Reiss, P.; Protiere, M.; Li, L., Core/Shell semiconductor nanocrystals. *Small* **2009,** *5* (2), 154-68.
36. Liu, Y.; Li, D.; Zhang, L.; Chen, Y.; Geng, C.; Shi, S.; Zhang, Z.; Bi, W.; Xu, S., Amine- and Acid-Free Synthesis of Stable CsPbBr3 Perovskite Nanocrystals. *Chem. Mater.* **2020,** *32* (5), 1904-1913.
37. De Palma, R.; Peeters, S.; Van Bael, M. J.; Van den Rul, H.; Bonroy, K.; Laureyn, W.; Mullens, J.; Borghs, G.; Maes, G., Silane Ligand Exchange to Make Hydrophobic Superparamagnetic Nanoparticles Water-Dispersible. *Chem. Mater.* **2007,** *19* (7), 1821-1831.

38. Hu, H.; Wu, L.; Tan, Y.; Zhong, Q.; Chen, M.; Qiu, Y.; Yang, D.; Sun, B.; Zhang, Q.; Yin, Y., Interfacial Synthesis of Highly Stable CsPbX3/Oxide Janus Nanoparticles. *J. Am. Chem. Soc.* **2018,** *140* (1), 406-412.
39. van den Brand, J.; Blajiev, O.; Beentjes, P. C.; Terryn, H.; de Wit, J. H., Interaction of anhydride and carboxylic acid compounds with aluminum oxide surfaces studied using infrared reflection absorption spectroscopy. *Langmuir : the ACS journal of surfaces and colloids* **2004,** *20* (15), 6308-17.
40. Uddin, M. A.; Mobley, J. K.; Masud, A. A.; Liu, T.; Calabro, R. L.; Kim, D.-Y.; Richards, C. I.; Graham, K. R., Mechanistic Exploration of Dodecanethiol-Treated Colloidal CsPbBr3 Nanocrystals with Photoluminescence Quantum Yields Reaching Near 100%. *The Journal of Physical Chemistry C* **2019,** *123* (29), 18103-18112.

Chapter 3: Fabrication and characterization of $CsPbBr_3$-based nanopatch antenna

Introduction

The nanopatch antenna configuration for single photon emitters has established itself as a high performance system with Purcell factors reaching several orders of magnitude. On the other hand, it also allows a certain degree of control over the direction of the emitted light. Early works on the configuration demonstrated both these properties for emitter embedded between a gold plate and micrometer-sized gold disk.[1-2] However, the Purcell factor was at best 80, which was modest. Efforts were then focused on different morphologies of the resonator. As a result, Ag nanocubes were proposed to replace gold disks.[3-5] One key advantage of the nanocubes is that the resonance wavelength depends on the cubes' size, which can be controlled well with different synthesis methods. Nanopatch antennas were fabricated, incorporating single or ensemble of emitters, and showed Purcell factors up to 2000, achieving benchmark performance.

Among other types of quantum dots, $CsPbBr_3$ nanocrystals have been incorporated into the nanopatch antenna as the emitter. A Purcell factor of 300 has been recorded, and the maximum value was estimated to be 4000.[6] Nonetheless, the question of stability for $CsPbBr_3$ NCs under high excitation power (up to 7.5 kW/cm^2) remains. As shown in the previous chapter, even at a power density of hundreds of W/cm^2, the photoluminescence of ensembles of $CsPbBr_3$ NCs decays to 17% within 30 minutes. For single particles, this interval is likely even shorter as interparticle interaction plays a major role in the photostability. Therefore, we aim to address this issue by using $CsPbBr_3/AlO_x$ core/shell NCs as the emitter in the nanopatch antenna due to their better performance and photostability.

Materials and Method

Ag nanocube synthesis

The synthesis of Ag nanocubes was performed based on the reported works from Xia et al.[7-8] Following the general synthesis considerations, solutions of 282 mM CF_3COOAg (98%, Sigma – Aldrich), 20 mg/mL poly (vinyl pyrrolidone) (PVP, average MW 55000, Sigma-Aldrich), 3 mM $NaHS.xH_2O$ (≥90%, Sigma – Aldrich), and 3 mM HCl (ACS Reagent, 37%, Sigma – Aldrich) were prepared in ethylene glycol (EG, 99.8% anhydrous, Sigma-Aldrich). To avoid contaminations, the solutions were prepared in disposable glassware, and glass pipettes were used in place of a metal spatula. For NaHS molecular weight, the formula was assumed to be $NaHS.H_2O$ (74 g/mol). 5 mL of EG was first added to a 25 mL round bottom flask in an oil bath preset to 150°C, and the flask was covered with glass stoppers. After the temperature is stable, 0.06 mL of the NaHS solution was quickly added, followed by 0.5 mL of the HCl and 1.25 mL of the PVP solutions after 2 min. After another 2 min, 0.4 mL of the CF_3COOAg solution was added drop-wise. The addition of all the solutions was performed using micropipettes of appropriate volume. The growth of the nanocubes was monitored by UV-vis spectroscopy, and when the cubes grew to the desired size, the reaction was quenched with a water bath. Acetone (twice the volume of the reaction mixture) was added to the solution, followed by centrifugation at 8000 rpm for 10 min. The supernatant was carefully discarded with a glass micropipette. Afterward, 2 mL of water was added to the precipitate and it was centrifuged at 12000 rpm for 5 min. The precipitate was collected and the process was repeated 3 more times to remove excess PVP. Finally, the precipitate was dispersed and stored in water.

Nanopatch antenna fabrication

Patterned Si wafers were used as substrates for the deposition of $CsPbBr_3$ NCs film, and their purpose will be detailed in the Result and Discussion section. The wafers were patterned by depositing a 100 nm thick SiO_2 layer on top of Si, then etching the layer by reactive-ion etching with SF_6. The resist AZ5214 was used as the mask, and the pattern is shown in Figure 3.1. Some of the wafers were then coated with a 10 nm titanium + 50 nm gold layer by sputtering. Before deposition, the wafers were cut into 5 mm x 5 mm squares and cleaned by 15-minute ultrasonication in acetone (twice) and then 1-isopropanol (once), and 15-minute UV-ozone treatment. After the cleaning step, some substrates were treated with (3-aminopropyl)triethoxysilane (APTES, Sigma-Aldrich) by immersing them in an anhydrous solution of 0.5 M APTES in toluene for 1 hour.

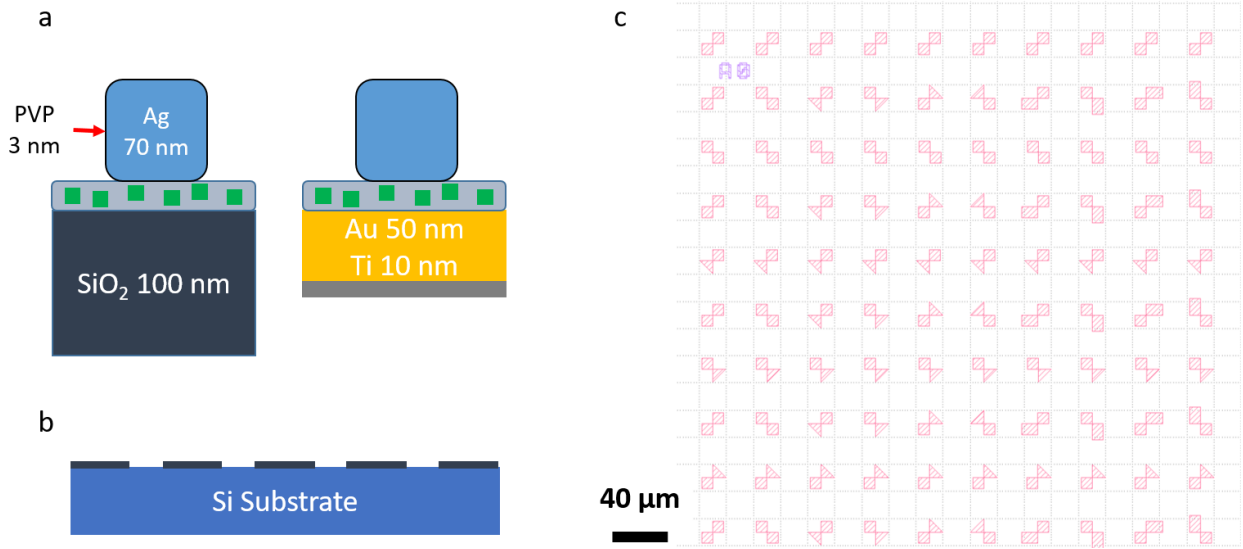

Figure 3.1. Illustrations of the targeted nanostructure (a), patterned Si substrate side view (b) and top view (c).

The suspension for deposition was obtained by mixing 10 µL of a 2.4 µM $CsPbBr_3$ NCs dispersion in toluene with 10 µL of 4 g/L poly(methyl methacrylate) (PMMA, MW ~120 000). The suspension was then spin-coated on the Si substrate at 4000 rpm for 60 s (4000 rpm/s), using a SPIN150 spin coater. The suspension was dropped onto the substrate before the spin coating was initiated. To deposit single particles, the same process was used, but the NCs were diluted by 1000 times. Afterward, Ag nanocubes were deposited on the film by spin coating 5 µL of the nanocubes suspension (1.15 g/L) at 2000 rpm for 60 s. The rotating speed was then increased to 4000 rpm for 10 s to remove the residual water on the film surface.

Characterization

Scanning electron microscopy (SEM) measurements were performed on a ZEISS Ultra 55 FE scanning electron microscope equipped with a Bruker QUANTAX EDS system. A Hewlett Packard 8452A Diode-Array Spectrophotometer was used for UV-vis measurements. Atomic force microscopy (AFM) measurements were performed on a Bruker ICON AFM. The thickness of the deposited films was probed by a Nanocalc reflectometer and DEKTAK 6M mechanical profilometer. Steady-state photoluminescence spectra of $CsPbBr_3$ NCs were collected by a Horiba iHR-550 spectrometer coupled with a Princeton instrument CCD camera. The irradiation source was provided by a continuous wave 405 nm semiconductor laser.

Time-resolved photoluminescence spectroscopy was performed in a confocal system. Continuous wave (CW) excitation was provided by a 405 nm laser diode, focused through a microscope objective with a numerical aperture of 0.55. The 0.46 m spectrometer was equipped with a 1200 grooves/mm grating providing a resolution of around 0.7 meV with a slit width of 0.2 mm, and slightly less than 0.2 meV with the smallest slit width (0.05 mm). For the detection, we used a CCD camera of 1024×256 pixels (26 µm/pixel). Pulsed excitation was provided by a near infra-red picosecond Titanium-Sapphire laser, doubled in frequency to 440 nm (2.82 eV) using a frequency doubling βBaB2O4 crystal. The pulse frequency was 76 MHz, resulting in a repetition time of 13.1 ns. For time-resolved data, the detection was provided by single-photon avalanche photodiodes (APD) id100-50 from id-Quantique, mounted on the side exit of the spectrometer. The diameter of the active area of the APD was 50 µm. The spectrometer was equipped with 1200 grooves/mm grating.

Results and Discussion

Ag nanocube synthesis

There are various synthetic routes to obtain Ag nanocubes in the literature, and this synthesis is chosen due to its ability to control the particle size in the range of 30 – 70 nm. The emission peak of $CsPbBr_3$ NCs is approximately 510 nm, which is separated from the plasmonic resonance of Ag nanocubes at 30 nm (Figure 3.2). On the other hand, the resonance shoulder of 70 nm nanocubes coincides with the NCs emission, which can cause the nanocubes to absorb the light emitted by the NCs. It is therefore interesting to compare the effect of the size of Ag nanocubes on the performance of the nanopatch antenna.

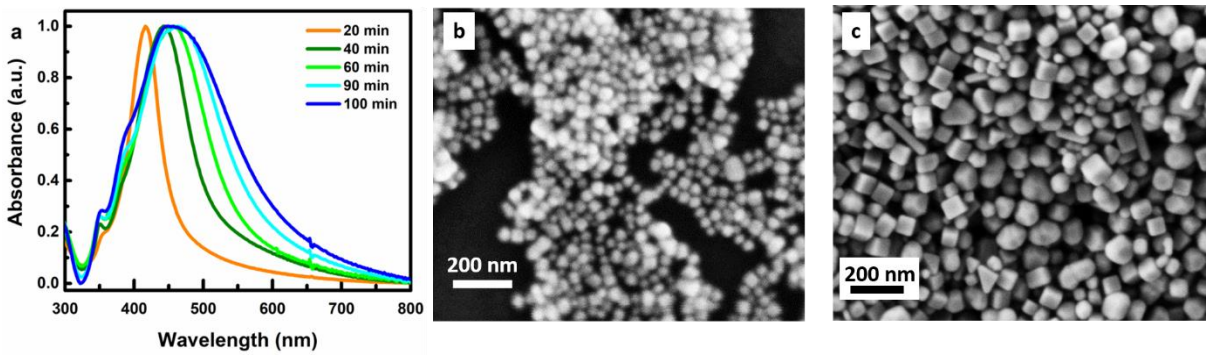

Figure 3.2. a) UV-vis spectra of Ag nanocubes at different reaction times, and SEM images of the resulting nanocubes at b) 20 min, and c) 100 min.

Figure 3.2a shows the UV-vis extinction spectra of the Ag nanocubes at different reaction time intervals. After 20 min, a sharp peak at 416 nm is observed alongside a small shoulder at 354 nm. This peak corresponds to the localized surface plasmon resonance (LSPR) due to dipole excitation of Ag particles ~30 nm in size, while the shoulder represents specific resonances of the cubic geometry.[9] With time, the main resonance peak shifts to a higher wavelength as the cubes grow larger. However, after 60 min, the shift becomes slower while the linewidth increases. Notably, after 100 min, the cubes grow to 70-80 nm in size (Figure 3.2c), but the absorption peak is at 446 nm instead of the expected value of 475 nm.[7] This is because at this size, the contribution of quadrupole excitation on the LSPR spectrum becomes non-negligible.[10] The result is a peak at roughly 450 nm. In addition, the large size dispersion (71 ± 13 nm) of Ag nanocubes causes the main peak to broaden, further decreasing its visibility. Moreover, the SEM image of the sample after 100 min of reaction shows the coexistence of triangles, spheres, and rods along with cubes (Figure 3.2c). As mentioned in the original paper, the

concentrations of NaHS and HCl play a crucial role in controlling the final morphology of the particles. We also notice that the fast addition of CF_3COOAg to the reaction mixture can cause the synthesis to fail. These parameters can be optimized to yield Ag nanocubes with high quality. For our study, we only need nanocubes of the desired size to be the dominant product, therefore we did not optimize this synthesis further.

$CsPbBr_3$ film deposition

Although there are many works in the literature with $CsPbBr_3$ NCs thin films and single particles, the details of the deposition process were not always stated clearly.[11-14] Therefore, we investigated the different parameters, namely the concentration of NCs, the concentration of PMMA, and the spin coating speed, to optimize the NCs film.

In the early stage of development, we functionalized the Si substrates with APTES molecules to provide better binding sites to the $CsPbBr_3$ NCs capped with hydrophobic ligands. To efficiently resolve the emission spectra of single particles with our optical setup (probe area ~4 μm^2), the particle density should be on the order of 1 NC per 10 μm^2. With the original NCs concentration of 3 µM and 95% material loss during spin coating,[15] an approximately 24000-fold dilution is necessary. This figure is coherent with the dilution factor of 40000 used to prepare single particles on a glass substrate.[13] We used this as the starting value, and varied the dilution from 100-fold to 40000-fold, fixing the rotation speed at 3000 rpm for 60 s (500 rpm/s).

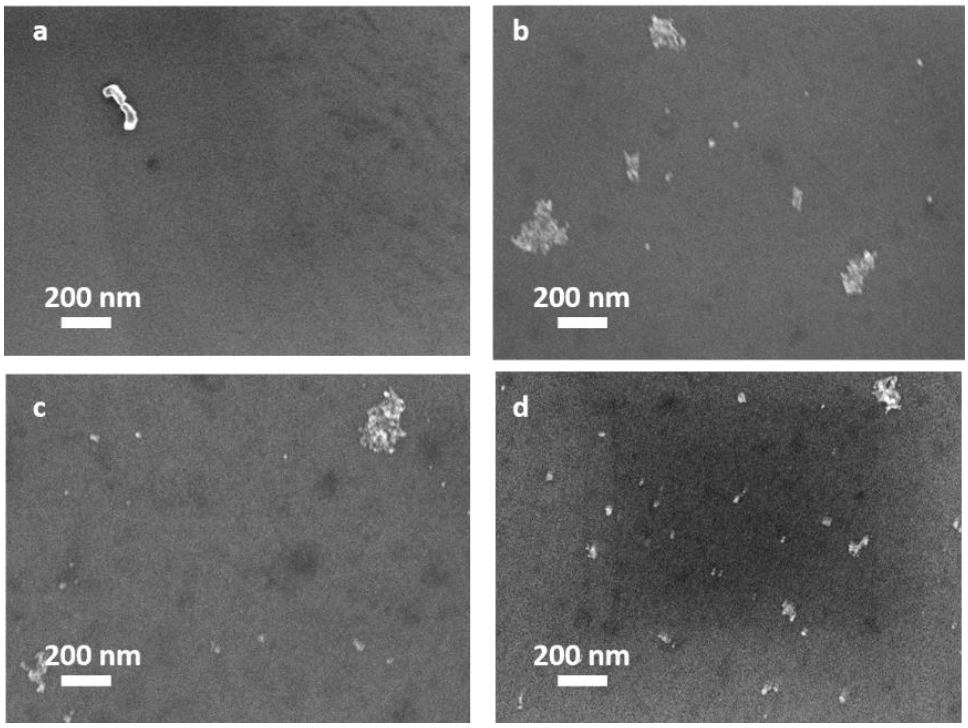

Figure 3.3. SEM images of the NCs film with different dilution factors for the NCs: a) 40000-fold, b) 5000-fold, c) 500-fold, and d) 100-fold.

At the highest dilution factor, we could not identify the particles (Figure 3.3a). As the dilution factor decreased, we started to observe the particles (Figure 3.3b-d). However, instead of distributing equally on the surface, most NCs tended to aggregate, and this tendency was stronger at higher dilution factors. As $CsPbBr_3$ NCs were surrounded by a labile ligand shell, as the NCs were diluted, more ligands would desorb from the surface.[16] Without a proper ligand shell to stabilize the NCs, they would form

large clusters as seen in the SEM images. At 100-fold dilution, the average interparticle distance was a few hundred nm, and the NCs were dispersed more evenly on the surface. For this reason, we chose to use the dilution factor at 100-fold for subsequent steps, unless stated otherwise.

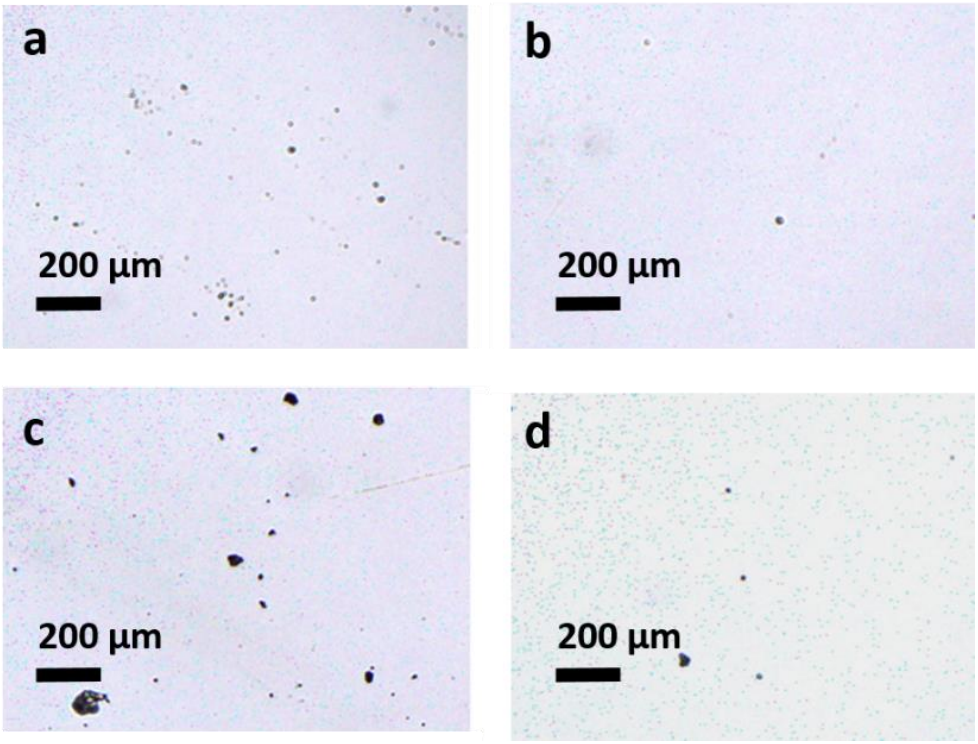

Figure 3.4. Optical microscopy image of the Si substrate with different surface treatment stages: a) initial surface, b) cleaned with acetone and isopropanol, c) functionalized with unfiltered APTES, d) functionalized with filtered APTES.

However, the use of APTES required precautions. First, despite the initial cleaning steps removing most of the surface impurities on the wafers, the functionalization step reintroduced some of them (Figure 3.4). This was rather unexpected as the solution was stored in a glove box, and the wafers were always washed with toluene after being functionalized to remove surface impurities. However, these impurities could be explained considering APTES's chemical nature. This molecule is highly susceptible to polymerization in the presence of water. Even in the inert storage condition, occasional exposure to moisture could cause polymer chains to form inside the chemical bottle, which subsequently deposited on the Si substrate. As a consequence, filtering the APTES solution with a 0.2 µm PTFE filter (VWR) before immersing the Si wafers eliminated most of these impurities (Figure 3.4d). Second, even without functionalization, the substrate managed to retain $CsPbBr_3$ NCs, which formed smaller clusters (Figure 3.5b). The distribution of the NCs in this manner was very suitable for single particle spectroscopy. On the other hand, the use of APTES, especially coupled with a low rotation speed, favored the formation of monolayer islands (Figure 3.5c), which could be advantageous for studies involving thin layers of $CsPbBr_3$ NCs. Therefore, depending on the purpose of the studies, the functionalization step was added to or removed from the process.

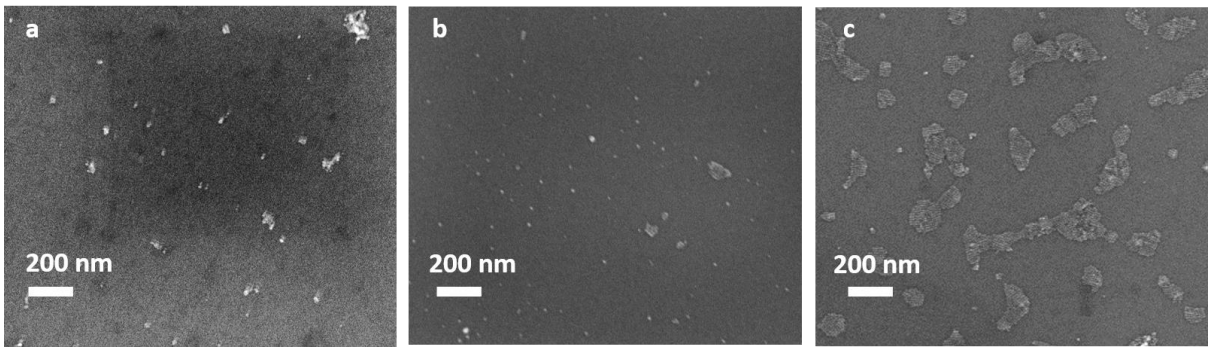

Figure 3.5. SEM image of the NCs film at different spin coating parameters: a) functionalized substrate, 3000 rpm, b) nonfunctionalized substrate, 3000 rpm, c) functionalized substrate, 2000 rpm.

The next objective was finding a concentration of PMMA suitable for mixing with $CsPbBr_3$ NCs. Since the surface of $CsPbBr_3$ NCs is not entirely stable even with ligands, and these ligands do not have good affinity with the side chain of PMMA,[13] controlling the amount of PMMA is important to ensure that the polymer can properly encapsulate the NCs without segregating or damaging the particles. To better observe the effects of PMMA on the NCs, we used $CsPbBr_3$ NCs in the thin layer configuration, leading to the use of the functionalized substrate. At first, we used a 2wt% PMMA/ethyl lactate solution (AR-P 679.02, Allresist), but this solvent was detrimental to the photostability of the NCs. Hence, we precipitated the polymer and redispersed it in toluene. From here on, the unit g/L will be used for the concentration of the PMMA solution instead of wt% (1 wt% PMMA/toluene is equal to 0.9 g/L PMMA/toluene).

PMMA/NCs blends with different PMMA concentrations were spin-coated on functionalized wafers at 2000 rpm (Figure 3.6). At high concentrations of 16 g/L and 40 g/L, $CsPbBr_3$ NCs and PMMA did not mix. $CsPbBr_3$ NCs would form a monolayer as observed previously, whereas PMMA formed either a web-like network or micron-size particles. At 8 g/L, however, no such structure was observed, but there was an additional layer appearing beneath the NCs layer. It was uncertain whether this layer represented PMMA, but the lack of PMMA microstructure indicated a better mixing of PMMA and the NCs at lower concentrations of PMMA.

Before further optimizing the process, we replaced the PMMA used for the deposition. The process of switching solvents demanded a long drying time to obtain accurate PMMA weight, and light exposure was inevitable, risking the degradation of the polymer. Therefore, PMMA powder (MW ~120 000) dissolved in toluene was used instead. First, this approach significantly reduced the preparation time and increased the reliability of PMMA concentration. More importantly, reducing the chain length of PMMA (MW 950 000 to 120 000) could allow better interaction between PMMA and the NCs due to the lowered degree of intramolecular interaction in PMMA with a shorter chain length. The wafers used were also not functionalized to reduce the competitive binding between the surface and the NCs, and the $CsPbBr_3$ NCs were not diluted to maintain the density of the NCs film.

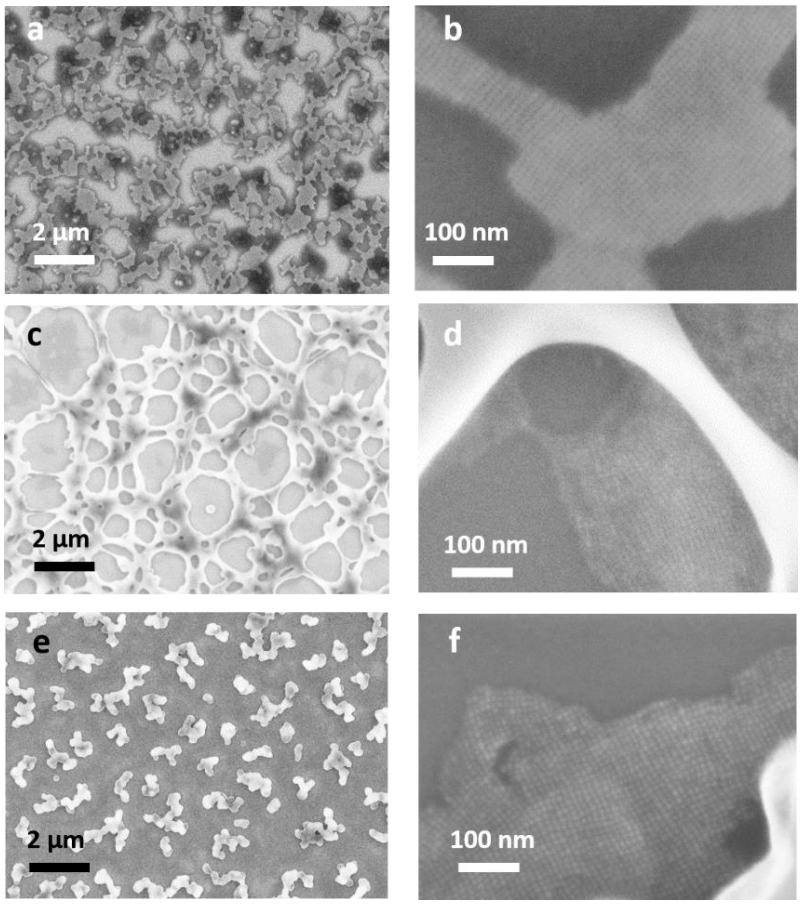

Figure 3.6. SEM images of NCs/PMMA films with different PMMA concentrations: 8 g/L (a, b), 16 g/L (c, d), 40 g/L (e, f).

Next, we investigated the relationship between the concentration of PMMA and the film thickness. Our goal is to reach a 15-20 nm thick film. As the average size of $CsPbBr_3$ NCs is 8-10 nm, this film thickness is just enough for PMMA to encapsulate a maximum of one NCs layer. At the rotation speed of 3000 rpm, as the concentration of PMMA decreased from 8 g/L to 4 g/L, the thickness of the film dropped from 86.4 nm to 57.7 nm (Table 3.1). As this thickness was not satisfactory, we further optimized the rotation speed at a PMMA concentration of 4 g/L. The rotation speed was increased from 3000 rpm to 4000 rpm and 6000 rpm, and a marked decrease in thickness was observed, from 57.7 nm at 3000 rpm to 19.3 nm and 15.9 nm at 4000 rpm and 6000 rpm, respectively. Comparing the increase in rotation speed versus the film thickness, 15.9 nm was likely near the limit we could reach with 4 g/L PMMA. Considering that at 4000 rpm, the thickness was in the range of our goal, and a higher rotation speed did not improve this figure much while stressing the system, we decided to use 4000 rpm and 4 g/L PMMA for subsequent film depositions.

Table 3.1. PMMA film thickness in nm with different PMMA concentrations and rotation speeds

PMMA conc. (g/L) \ Rotation speed	2000	3000	4000	6000
8		86.4		
4	58.1	57.7	19.3	15.9

Since the polymer layer could not be resolved well with SEM, atomic force microscopy measurements were performed to verify the encapsulation of $CsPbBr_3$ NCs by the polymer. The thin films for this measurement were obtained by spin coating a mixture of 4 g/L PMMA and 4 µM $CsPbBr_3/AlO_x$ NCs at 3000 rpm and 6000 rpm. The NCs were used without dilution to compensate for the lack of APTES. At these rotation speeds, one film was expected to be 60 nm thick (3000 rpm), and the other 16 nm thick (6000 rpm). As the film thickness was always higher than the size of individual particles, a well-encapsulated NCs film would show a smooth surface (roughness smaller than the edge length of a particle). Furthermore, the topography image would not show any NC, easily identified by their cubic shape. In both samples, we observed a similarly smooth surface, with an average roughness of 3.71 nm and 3.17 nm for the thick and thin films, respectively (Figure 3.7a, c). The topography images, however, recorded NCs on the surface of the film, but the density is low (Figure 3.7b, d). They also appeared to be the region with the highest Z-level in the image. If a complete layer of NCs was present on the surface, the topography image would show square-shaped objects arranged in a rather organized fashion, much like what was observed in the TEM images of the NCs. From these results, it can be concluded that in both the thick and thin films, most of the NCs were encapsulated by PMMA. Some of them partially protruded from the film, with an average exposed height of 3 - 4 nm.

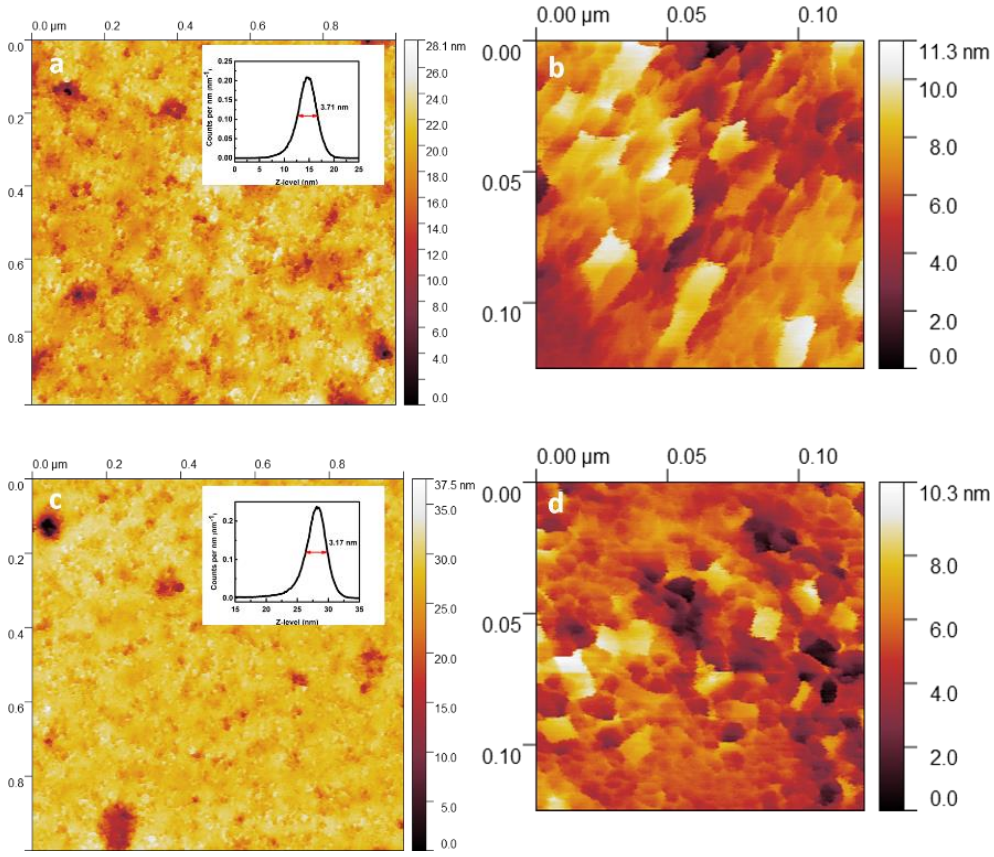

Figure 3.7. AFM images of NCs/PMMA film prepared with different rotation speeds: 3000 rpm (a, b), 6000 rpm (c, d). The scan range (in-plane) was 1 µm for images a and b, and 300 nm for images c and d. The insets are distributions of Z-level per nm.

Having obtained the desired thin film where the perovskite core or core/shell NCs were embedded in PMMA, we proceeded to deposit Ag nanocubes on the film. We tried to optimize the distribution of

Ag nanocubes through the solvent used for deposition. Water and ethanol are both good solvents to disperse the nanocubes while being incapable of dissolving PMMA. These properties ensure that the perovskite/polymer layer is not washed away during the nanocubes deposition process. We confirmed the presence of both $CsPbBr_3$ NCs and Ag nanocubes with SEM (Figure 3.8).

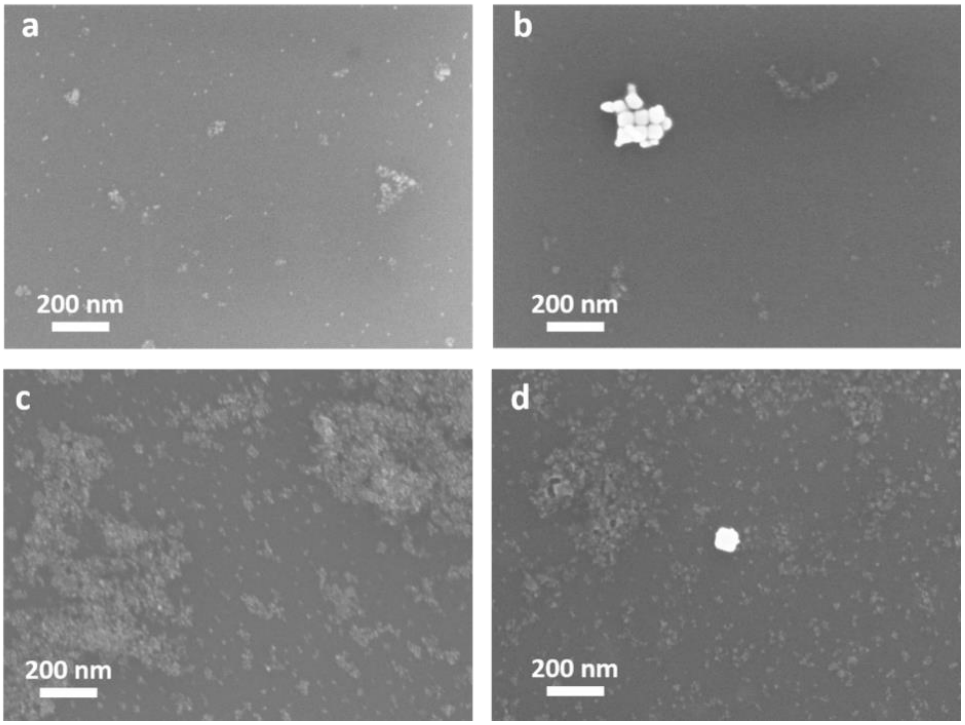

Figure 3.8. SEM images of the NCs/PMMA film before and after Ag nanocubes deposition with ethanol (a, b), and with water (c, d).

With both solvents, small clusters and single nanocubes distributed on the film with an average distance of a few µm. This distance is ideal for the optical measurement since it is large enough so that no two nanocubes can be measured at the same time while it is short enough to ensure we could quickly move from one cube to the other. However, the nanocubes tended to form aggregates when spin-coated using ethanol. It is likely that due to the faster evaporation of ethanol compared to water during the spin coating process, nanocubes in the droplet did not have sufficient time to settle on the surface and were pulled together instead. This explanation is further supported by the appearance of extremely large (micrometer-sized) aggregates when the spin coating rotation speed was doubled. In contrast, most nanocubes deposited using water were situated separately on the film.

AFM measurements suggested that the surface of the film was modified after Ag nanocubes were spin-coated. We managed to record the topography of Ag nanocubes deposited on the $CsPbBr_3$ NCs (Figure 3.9a, b). Though the corners of the cube were not resolved well due to the cantilever's state, the cube's edge length was in the range determined by SEM and spectroscopic data. As for the film, in the Z-level distribution, a new peak was displayed with a lower average height compared to the original peak (Figure 3.9d). Additionally, this peak had a larger linewidth of 6.5 nm. Taken together, the data implies that after the deposition, pinholes started to form on the surface. As the deposition involved water, it was highly possible that the water degraded and washed away some of the exposed $CsPbBr_3$ NCs, leaving pinholes in their places.

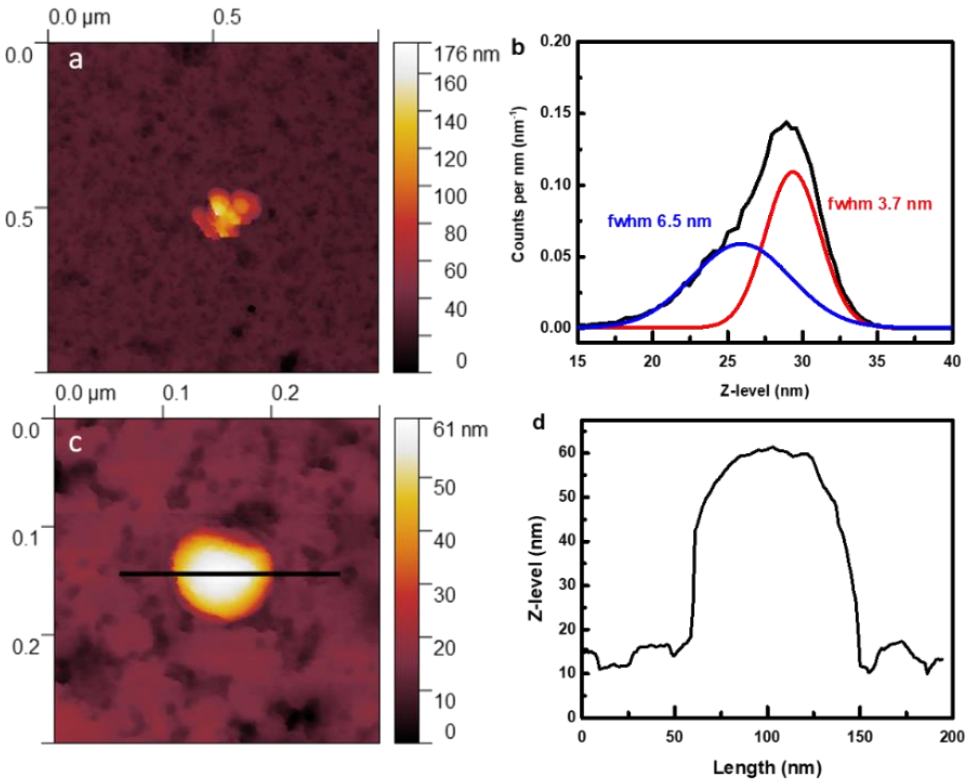

Figure 3.9. a) AFM images of the NCs/PMMA film with Ag nanocubes, b) the histogram of surface roughness, c) AFM image of a single Ag nanocube and its corresponding height profile (d).

Optical characterization

SEM was used to locate the positions of the nanoantennas with respect to the patterns on the substrate. Afterward, with the CCD camera coupled to the spectroscopy system, we managed to move the laser spot to these antennas for optical characterization. Then we moved the laser spot slightly away from these points and performed the control measurement. The PL spectra of the two points were mostly similar, except for a slight difference in the linewidth (Figure 3.10). The lifetimes of the NCs decreased compared to the values recorded in toluene. Since the NCs were closely packed in the film, interparticle charge transfer became possible and caused excited electrons to decay faster, like in the case of CdSe NCs.[17] In comparison to spots without the antennas, spots with antennas displayed no enhancement in decay rate, with the fast component's lifetime being 0.57 ± 0.09 ns (29 ± 9%) and 0.54 ± 0.11 (28 ± 7%) ns for the spots with and without the nanoantennas, respectively.

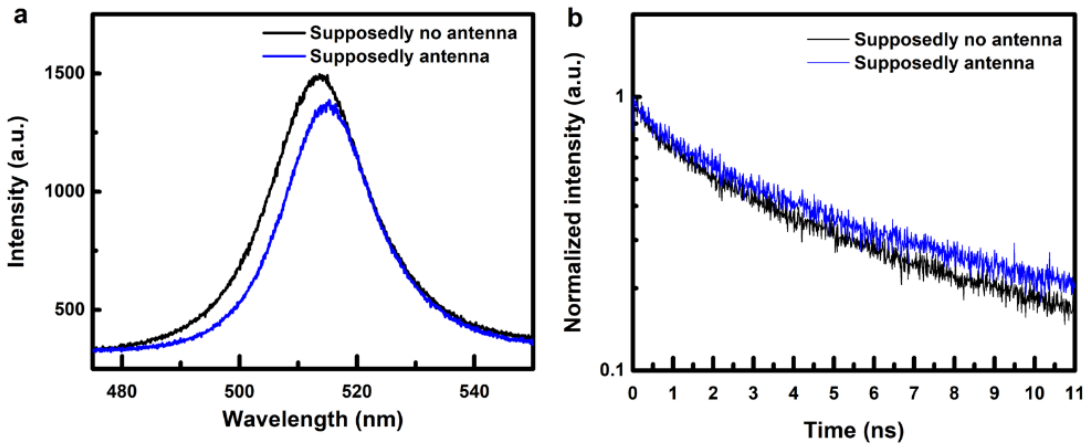

Figure 3.10. Emission (a) and photoluminescence decay (b) spectra of the nanopatch antenna fabrication on Si/SiO_2 surface.

During the measurement, it was difficult for us to be sure of the positions of the antennas. Despite being able to locate them with SEM, the low spatial resolution of the confocal setup made it hard to reliably direct the laser beam to the desired spots. We tried to record the scattering signal of the surface using a side excitation (405 nm CW laser). As the size of the Ag nanocubes was much larger than $CsPbBr_3$ NCs, strong scattering could be expected. By locating the spots where such a phenomenon occurred, we would be able to determine the position of the nanoantennas. However, the signal we detected consisted of both surface scattering and emission from $CsPbBr_3$. Though we managed to separate these signals by using a 500 nm shortpass filter, the scattering signal's reliability was reduced to a certain degree. Since the thin film deposition proceeded outside of the cleanroom, this allowed micron-size dust particles to settle on the film and scattered the side excitation. Moreover, attempts to distinguish the nanoantenna by emission enhancement on NCs were not successful. The distance between the two reflective planes (Ag and Si) in this configuration was roughly 200 nm. As the laser spot was much larger than the size of the antenna, the emission from surrounding NCs also contributed to background noise, obscuring the enhancement from the antenna.

To increase the chance of spotting the antennas, we adapted the configuration of Hoang et al., where the NCs were directly deposited on a gold substrate.[4] The emission of NCs near the metal can be quenched by a combination of energy transfer to the metal,[18] and the fact that the NCs now lie at the node of the standing wave created when light is reflected from the substrate. In contrast, NCs situated between the Au layer and the Ag nanocubes will have their emission enhanced due to the cavity's effect.

As we scanned the substrate surface, we observed that the emission intensity decreased by a factor of 8, and sometimes completely, in accordance with the quenching effect. However, we still observed bright areas, which were later confirmed by SEM to be aggregates of NCs (Figure 3.11a). Because of this incomplete quenching, we had the same problem as previously when trying to determine the position of the antennas. Therefore, we prepared an identical NCs film without Ag nanocubes, which acted as the control sample. In both samples, the dark spots tended to decay faster, with the fast component contributing more to the photoluminescence decay (Figure 3.11 b and d). This trend represents the effect of the metal layer on the NCs. Regardless of the emission intensity, the sample with Ag antennas showed reduced decay times compared to the control sample (Table 3.2, the errors

were obtained by averaging over three random points). In addition, the contribution from the fast component also increased in this sample. Though this increase could be attributed to the coupling with Ag antennas, the emission from surrounding particles was still an issue in this measurement. Therefore, better luminescence quenching should be achieved to resolve the effect of the resonance structure.

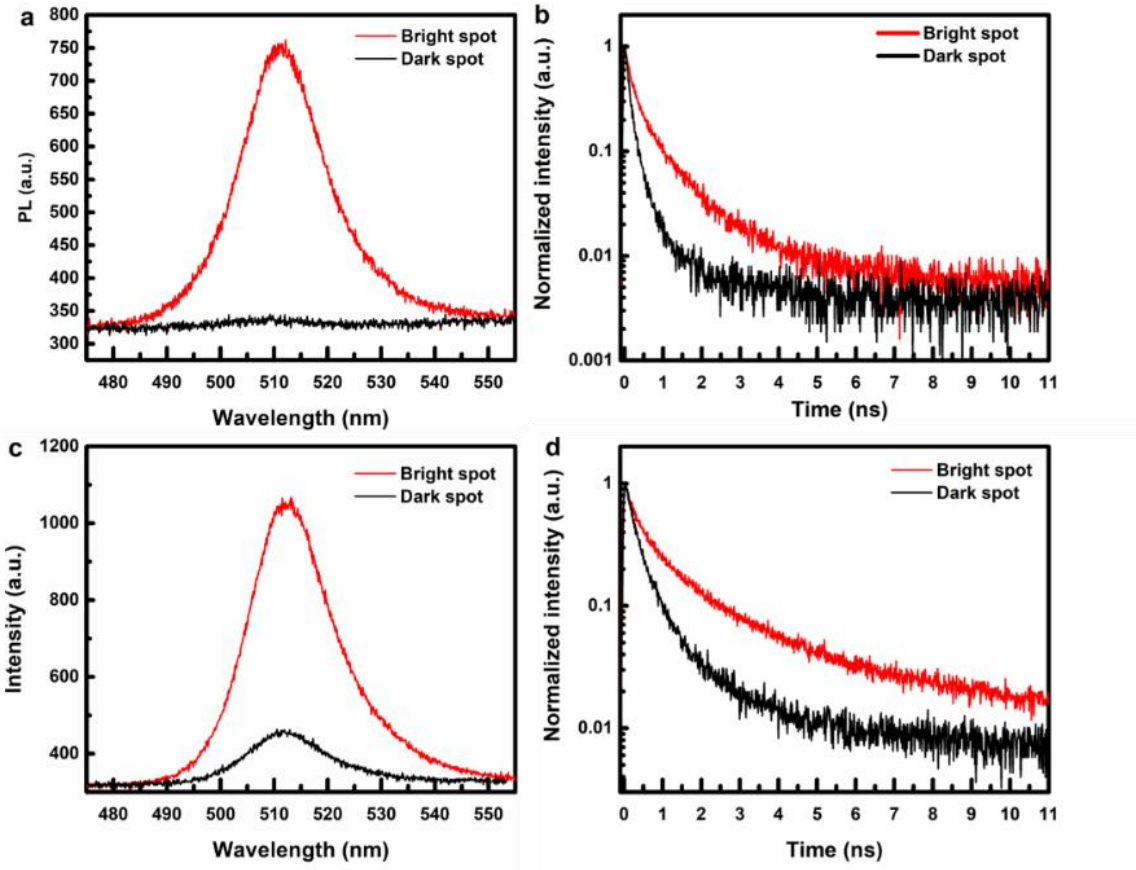

Figure 3.11. Emission and photoluminescence decay spectra of the nanopatch antenna (a, b) and NCs/PMMA film (c, d) fabricated on $Si/SiO_2/Au$ surface.

Table 3.2. Parameters of the photoluminescence decay fit, with the errors given in brackets.

		τ_1 (ns)	A_1	τ_2 (ns)	A_2
Without antenna	Bright spot	0.28 (0.01)	0.62 (0.01)	1.57 (0.08)	0.38 (0.01)
	Dark spot	0.24 (0.01)	0.77 (0.05)	0.93 (0.02)	0.23 (0.05)
With antenna	Bright spot	0.13 (0.03)	0.76 (0.04)	0.67 (0.17)	0.24 (0.04)
	Dark spot	0.11 (0.02)	0.87 (0.04)	0.56 (0.09)	0.13 (0.04)

Conclusion

In conclusion, we have fabricated a nanopatch antenna consisting of a layer of $CsPbBr_3/AlO_x$ NCs encapsulated in PMMA in-between a gold-coated substrate and silver nanocubes of approximately 70 nm in size. The concentration of NCs, substrate functionalization and spin coating speed were found

to be crucial in controlling the density of the NCs, from a monolayer to clusters. The mixture of PMMA and NCs had to be optimized in terms of composition to achieve the ideal film thickness. Finally, the deposition of Ag nanocubes was found to wash away perovskite NCs on the surface of the film, highlighting the role of PMMA in protecting the NCs. We observed an increased decay rate by a factor of 2 on the sample with nanoantenna compared to the control sample. However, the two samples did not show much difference in terms of emission intensity, and we could not locate the exact position of the Ag nanocubes on the sample. Therefore, we could not readily conclude that we observed the enhancement from the nanopatch antenna. Further works will be done to clarify the aforementioned point, and to compare the performance and stability of the device using $CsPbBr_3$ and $CsPbBr_3/AlO_x$ NCs.

References

1. Esteban, R.; Teperik, T. V.; Greffet, J. J., Optical patch antennas for single photon emission using surface plasmon resonances. *Phys. Rev. Lett.* **2010,** *104* (2), 026802.
2. Belacel, C.; Habert, B.; Bigourdan, F.; Marquier, F.; Hugonin, J. P.; de Vasconcellos, S. M.; Lafosse, X.; Coolen, L.; Schwob, C.; Javaux, C.; Dubertret, B.; Greffet, J. J.; Senellart, P.; Maitre, A., Controlling spontaneous emission with plasmonic optical patch antennas. *Nano Lett.* **2013,** *13* (4), 1516-21.
3. Akselrod, G. M.; Argyropoulos, C.; Hoang, T. B.; Ciracì, C.; Fang, C.; Huang, J.; Smith, D. R.; Mikkelsen, M. H., Probing the mechanisms of large Purcell enhancement in plasmonic nanoantennas. *Nature Photonics* **2014,** *8* (11), 835-840.
4. Hoang, T. B.; Akselrod, G. M.; Argyropoulos, C.; Huang, J.; Smith, D. R.; Mikkelsen, M. H., Ultrafast spontaneous emission source using plasmonic nanoantennas. *Nature communications* **2015,** *6*, 7788.
5. Hoang, T. B.; Akselrod, G. M.; Mikkelsen, M. H., Ultrafast Room-Temperature Single Photon Emission from Quantum Dots Coupled to Plasmonic Nanocavities. *Nano Lett.* **2016,** *16* (1), 270-5.
6. Hsieh, Y. H.; Hsu, B. W.; Peng, K. N.; Lee, K. W.; Chu, C. W.; Chang, S. W.; Lin, H. W.; Yen, T. J.; Lu, Y. J., Perovskite Quantum Dot Lasing in a Gap-Plasmon Nanocavity with Ultralow Threshold. *ACS nano* **2020,** *14* (9), 11670-11676.
7. Zhang, Q.; Li, W.; Wen, L. P.; Chen, J.; Xia, Y., Facile synthesis of Ag nanocubes of 30 to 70 nm in edge length with CF(3)COOAg as a precursor. *Chemistry* **2010,** *16* (33), 10234-9.
8. Skrabalak, S. E.; Au, L.; Li, X.; Xia, Y., Facile synthesis of Ag nanocubes and Au nanocages. *Nature protocols* **2007,** *2* (9), 2182-90.
9. Sosa, I. O.; Noguez, C.; Barrera, R. G., Optical Properties of Metal Nanoparticles with Arbitrary Shapes. *The Journal of Physical Chemistry B* **2003,** *107* (26), 6269-6275.
10. Zhou, F.; Li, Z.-Y.; Liu, Y.; Xia, Y., Quantitative Analysis of Dipole and Quadrupole Excitation in the Surface Plasmon Resonance of Metal Nanoparticles. *The Journal of Physical Chemistry C* **2008,** *112* (51), 20233-20240.
11. Utzat, H.; Sun, W.; Kaplan, A. E. K.; Krieg, F.; Ginterseder, M.; Spokoyny, B.; Klein, N. D.; Shulenberger, K. E.; Perkinson, C. F.; Kovalenko, M. V.; Bawendi, M. G., Coherent single-photon emission from colloidal lead halide perovskite quantum dots. *Science* **2019,** *363* (6431), 1068-1072.
12. Tang, X.; Yang, J.; Li, S.; Liu, Z.; Hu, Z.; Hao, J.; Du, J.; Leng, Y.; Qin, H.; Lin, X.; Lin, Y.; Tian, Y.; Zhou, M.; Xiong, Q., Single Halide Perovskite/Semiconductor Core/Shell Quantum Dots with Ultrastability and Nonblinking Properties. *Advanced science* **2019,** *6* (18), 1900412.
13. Raino, G.; Landuyt, A.; Krieg, F.; Bernasconi, C.; Ochsenbein, S. T.; Dirin, D. N.; Bodnarchuk, M. I.; Kovalenko, M. V., Underestimated Effect of a Polymer Matrix on the Light Emission of Single CsPbBr3 Nanocrystals. *Nano Lett.* **2019,** *19* (6), 3648-3653.
14. Raino, G.; Nedelcu, G.; Protesescu, L.; Bodnarchuk, M. I.; Kovalenko, M. V.; Mahrt, R. F.; Stoferle, T., Single Cesium Lead Halide Perovskite Nanocrystals at Low Temperature: Fast Single-Photon Emission, Reduced Blinking, and Exciton Fine Structure. *ACS nano* **2016,** *10* (2), 2485-90.
15. Sahu, N.; Parija, B.; Panigrahi, S., Fundamental understanding and modeling of spin coating process: A review. *Indian Journal of Physics* **2009,** *83* (4), 493-502.
16. Nenon, D. P.; Pressler, K.; Kang, J.; Koscher, B. A.; Olshansky, J. H.; Osowiecki, W. T.; Koc, M. A.; Wang, L. W.; Alivisatos, A. P., Design Principles for Trap-Free CsPbX3 Nanocrystals: Enumerating and

Eliminating Surface Halide Vacancies with Softer Lewis Bases. *J. Am. Chem. Soc.* **2018,** *140* (50), 17760-17772.
17. Kagan, C. R.; Murray, C. B.; Nirmal, M.; Bawendi, M. G., Electronic energy transfer in CdSe quantum dot solids. *Phys. Rev. Lett.* **1996,** *76* (9), 1517-1520.
18. Ruppin, R., Decay of an excited molecule near a small metal sphere. *The Journal of Chemical Physics* **1982,** *76* (4), 1681-1684.

Chapter 4: Synthesis and characterization of $CsPbBr_3$ nanocrystals doped with metal cations

Introduction

The most common way of tuning the emission wavelength of lead halide perovskite (ABX_3) nanocrystals (NCs) is by varying the halide composition.[1-3] However, mixed halide perovskites ($ABCl_{3-x}Br_x$, $ABBr_{3-x}I_x$) tend to segregate into the individual single-halide components ($ABCl_3$, $ABBr_3$, ABI_3) under illumination or applied electrical current due to halide migration within the ionic lattice.[4-6] Although this process can be reversed in the dark, it strongly limits the applicability of mixed halide perovskite NCs in light-emitting devices.[7] Cation doping of halide perovskite NCs represents a potential alternative strategy to achieve tunable and stable photoluminescence (PL).[8-9] As an example, Mn^{2+}-doping of $CsPbBr_3$ NCs induces a new emission band due to the intrinsic electronic transition of the dopant ions and can also improve the PL efficiency and photostability.[10-11] Aside from Mn^{2+}, other divalent metal cations have been explored, such as Cd^{2+}, Zn^{2+}, and Sn^{2+},[12-13] which led to a blueshift of the emission wavelength and maximum achievable doping levels for the method reported of 16 at. % (Cd^{2+}), 10 at. % (Sn^{2+}), and 5 at. % (Zn^{2+}).[13] Finally, doping of perovskite NCs with trivalent ions has been investigated.[14-16] In this case, when Pb^{2+} and the dopant ions share similar sizes, the optical properties are mostly affected by the extra charge from the dopant. While Bi^{3+} generates trap states deeper below the conduction band, reducing the photoluminescence quantum yield (PLQY) with increasing dopant concentration,[15, 17] Ce^{3+} creates shallow defects of a radiative nature, which can lead to QY enhancement.[14, 18] In contrast to these examples, Al^{3+} is a trivalent ion with a significantly smaller size (54 pm) than Pb^{2+} (119 pm). Nonetheless, Al^{3+} could be successfully doped into $CsPbBr_3$ NCs by adding $AlBr_3$ to the reaction precursors at the beginning of the synthesis.[19] Once again, a blueshift of the absorption and emission spectra was observed, which was attributed to a change in the electronic structure of the doped NCs. Theoretical calculations indicated the widening of the band gap when Al^{3+} was introduced into the host lattice, with only a minor contribution of crystal lattice contraction.

Not only can metal doping alter the emission of halide perovskite, but it also can introduce magneto-optical properties to the compound. Based on the established research on diluted magnetic semiconductors, lead halide perovskites with various compositions have been doped with Mn^{2+}. In $CH_3NH_3PbI_3$, substituting 10% of Pb by Mn turns the material into ferromagnetic (T_C = 25 K) due to superexchange interaction between the Mn^{2+} ions.[20] Furthermore, under illumination, more conduction electrons are generated and RKKY exchange is enhanced, disturbing the spin ordering from superexchange. In 2D Ruddlesden – Popper perovskites doped with 1% Mn, the emission of dark excitons considerably increases with the strength of the applied magnetic field, a process called magnetic brightening. At the nanoscale, Mn-doped $CsPbBr_3$ NCs show the formation of exciton magnetic polarons, in which excitons induce a ferromagnetic ordering of Mn^{2+} spins.[21] As a result, giant Zeeman splitting as well as brightening of the dark state have been observed to increase with the doping level.

Here, we performed post-synthetic room-temperature doping of $CsPbX_3$ (X = Br, I) NCs with Al^{3+} and Mn^{2+} for a wide range of doping levels, with the former being a completely original approach. For Al-doped $CsPbBr_3$ NCs, we correlate doping-induced changes in the lattice parameter with the PL emission energy, revealing a linear relationship with the opposite sign of the slope than that observed in bulk $CsPbBr_3$, i.e., an increase of the PL energy with decreasing lattice parameter. In addition, we attempted to investigate the magneto-optical properties of Mn-doped $CsPbX_3$ NCs with different

compositions. As the band edges of the host NCs are tuned by varying the halides, we expected to be able to control the magnitude of the sp–d exchange, and thus the resulting giant Zeeman splitting.

Materials and Methods

Doped $CsPbBr_3$ NC synthesis

The undoped $CsPbBr_3$ NCs were synthesized as reported in Chapter 2. Post-synthetic doping of aluminum consists of the dropwise addition of the dopant precursor solution (1 M $AlBr_3$ in CH_2Br_2, Sigma-Aldrich) diluted in anhydrous toluene to a colloidal solution of 2.4 µM $CsPbBr_3$ NCs in anhydrous toluene at room temperature for 1 h. For manganese doping, a 0.1 M solution of $MnBr_2$ (99%, anhydrous, Alfa Aesar) or MnI_2 (98%, Alfa Aesar) in a mixture of toluene and acetone (3:1 v:v) was added to the 2.4 µM $CsPbBr_3$ NCs colloidal solution and was kept stirring for 1 h.[22] Afterwards, the NCs were purified by the addition of 2/1 v/v anhydrous methyl acetate and centrifugation at 12 000 rpm for 5 min. As will be discussed below, for both types of dopant the choice of solvent is of crucial importance for the successful doping process.

Characterization

Scanning electron microscopy (SEM) measurements were performed on a ZEISS Ultra 55 FE scanning electron microscope equipped with a Bruker QUANTAX EDS system, and transmission electron microscopy (TEM) images were collected with an FEI Tecnai F20 microscope. ICP-AES measurements were performed on a Shimadzu 9000 spectrometer. Standards solutions of Pb, Al and Mn were prepared by diluting the ICP standards of the three metal ions with Milli-Q water with HNO_3 10% (v/v). Subsequently, calibration curves were established for the concentration range relevant to our samples. The detection wavelength for each element was 405.783 nm (Pb), 396.153 nm (Al), and nm (Mn). For UV-vis and PL measurements, a Hewlett Packard 8452A diode-array spectrophotometer and a Hitachi F-4500 fluorescence spectrophotometer were used, respectively. X-ray photoelectron spectroscopy (XPS) analyses were carried out with a Versa Probe II spectrometer (ULVAC-PHI) equipped with a monochromated Al Kα source (hν = 1486.6 eV). The core-level peaks were recorded with a constant pass energy of 23.3 eV. The XPS spectra were fitted with CasaXPS 2.3 software using Shirley background. Binding energies (BEs) are referenced with respect to adventitious carbon (C 1s BE = 284.8 eV).

For powder X-ray diffraction (XRD), the samples were drop-casted on a disoriented silicon substrate, and the measurements were performed with a PANalytical X'pert Pro powder diffractometer equipped with a copper anode (λKα=1.5406 Å) and an X'Celerator 1D detector. HighScore Plus software was used for the Le Bail refinement of the crystal lattice. For the temperature dependent measurements, we used a Bruker D8 diffractometer equipped with a copper anode (λKα=1.5406 Å) and a 1D LynxEye detector, as well as a heating element. The sample was not drop-casted but rather dried and ground to fine powder before being deposited in a Ni chamber. Cooling of the sample down to -190 °C was achieved by liquid nitrogen. Le Bail refinement was done with the TOPAS software.

Measurements of the absolute photoluminescence quantum yield (PLQY) were performed on Fluorolog-3 spectrofluorometer (Jobin-Yvon) equipped with an integration sphere, using an R928 PMT detector, and a 450 W Xenon lamp as the excitation source. The excitation wavelength was 420 nm and the optical density of the samples at this wavelength was adjusted between 0.1 and 0.2.

Temperature-dependent photoluminescence spectroscopy was performed in a confocal system. The irradiation source was provided by a continuous-wave 405 nm semiconductor laser with a power density of 28 W/cm^2. The signal was then collected with a Horiba iHR-550 spectrometer equipped with a 600 grooves/nm grating and coupled with a Princeton Instrument CCD camera.

Time-resolved photoluminescence spectroscopy was performed in another confocal system. Continuous-wave (CW) excitation was provided by a 405 nm laser diode, focused through a microscope objective with a numerical aperture of 0.55. The 0.46 m spectrometer was equipped with a 1200 grooves/mm grating providing a resolution of around 0.7 meV with a slit width of 0.2 mm, and slightly less than 0.2 meV with the smallest slit width (0.05 mm). For the detection, we used a CCD camera of 1024×256 pixels (26 µm/pixel). Pulsed excitation was provided by a near infra-red picosecond Titanium-Sapphire laser, doubled in frequency to 440 nm (2.82 eV) using a frequency doubling βBaB2O4 crystal. The pulse frequency was 76 MHz, resulting in a repetition time of 13.1 ns. For time-resolved data, the detection was provided by single-photon avalanche photodiodes (APD) id100-50 from id-Quantique, mounted on the side exit of the spectrometer. The diameter of the active area of the APD was 50 µm. The spectrometer was equipped with 1200 grooves/mm grating. The magneto-optical measurement was performed on the same system, but the sample was placed within a commercial neodymium iron boron magnet (0.5 Tesla) with the magnetic field pointing towards the lens. A λ/4 wave plate in tandem with a linear polarizer were used to detect light with different circular polarizations.

Results and Discussion

Al-doped $CsPbBr_3$ NCs

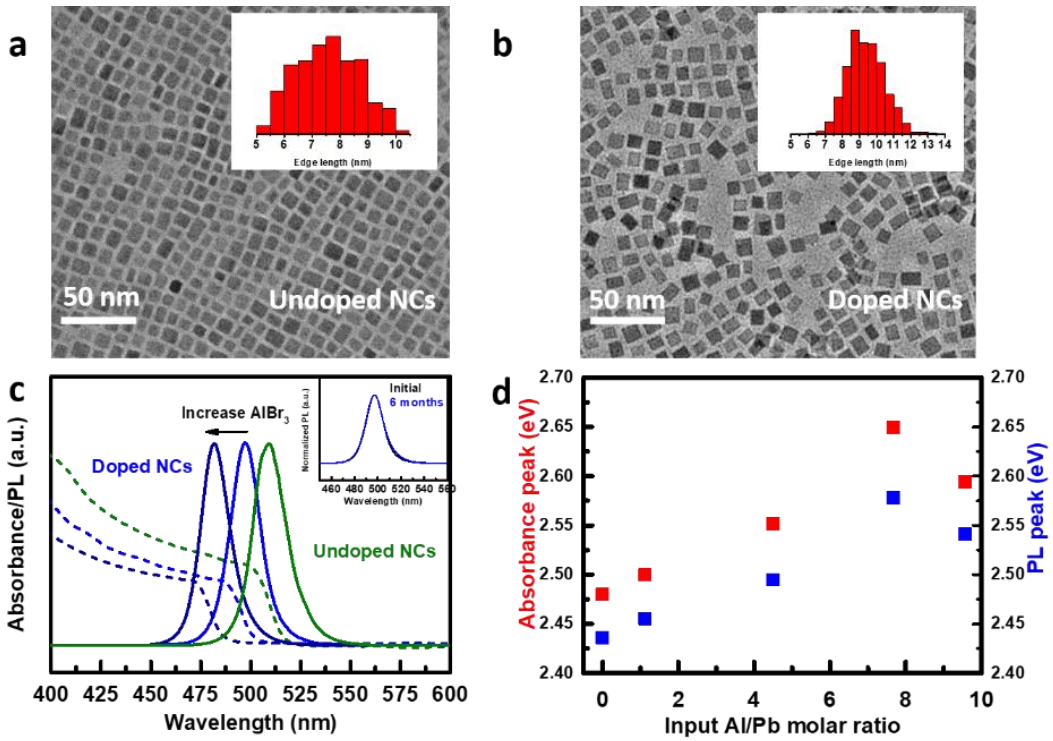

Figure 4.1. a, b) TEM images of the undoped and doped NCs (Al/Pb ratio: 4.5), c) Absorption and PL spectra of undoped and doped NCs (Al/Pb ratio of 4.5 and 7.7), with the inset showing the PL of doped

NCs (Al/Pb ratio 4.5) recorded directly after synthesis and after 6 months, d) Variation in absorption and PL peaks with the doping input ratio.

Figure 4.1a and b show TEM images of doped and undoped $CsPbBr_3$ NCs. Up to an Al/Pb input ratio of 4.5, a small size increase was observed without affecting the size distribution, namely, for the ratio of 4.5 from 7.6 ± 1.2 nm (undoped sample) to 9.4 ± 1.1 nm (doped sample). For larger Al/Pb ratios, the NC size slightly decreased (Figure 4.2). Moreover, the organization of the NCs on the TEM grid became less ordered, suggesting that the surface of these NCs has been altered.

As visible in Figure 4.1c, the UV−vis absorption and photoluminescence (PL) spectra exhibited a blueshift after introducing Al^{3+}, and by varying the concentration of the $AlBr_3$ precursor, the PL peak of the doped NCs could be adjusted in the range 509−482 nm. The PLQY slightly decreased upon doping from 72.5% for the undoped NCs to 57.4% and 63.5% for the doped sample with an Al/Pb ratio of 4.5 and 7.5, respectively. This decrease is attributed to the additional washing step of the doped samples.[20] Importantly, for a given doping level, no spectral shift was observed even after 6 months of storage (Figure 4.1c, inset), which implies that the doping process led to a stable structural configuration. Increasing the Al/Pb input ratio above 8 resulted in a reverse spectral behavior, i.e., a bathochromic shift in both the absorption and PL emission spectra. A similar trend has been observed for the doping of $CsPbBr_3$ NCs with the divalent cations Sn^{2+}, Cd^{2+}, and Zn^{2+}.[13]

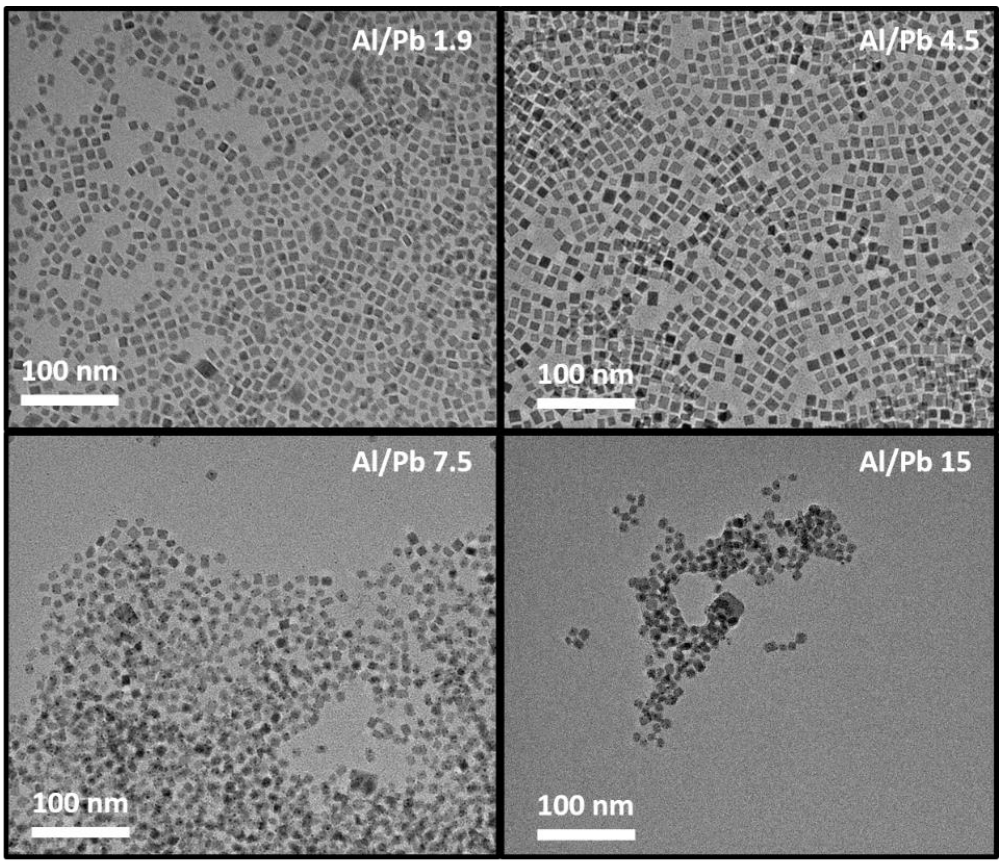

Figure 4.2. TEM images of doped samples with different Al/Pb input ratios.

Determining the Al^{3+} content with EDX spectroscopy turned out to be challenging, as the Kα energy of Al (1.4867 keV) is very close to the Lα energy of Br (1.4804 keV), rendering them indistinguishable. Moreover, increasing the incident energy to record the Kα energy of Br (11.9242 keV) presents a

significant risk of destroying the sample. Therefore, XPS and ICP-AES were employed to analyze the doped NCs in more detail. In Figure 4.3, it can be seen that, after the post-synthetic treatment with the $AlBr_3/CH_2Br_2$ solution, a new signal related to Al 2p was detected at 74.2 eV, corresponding to the Al^{3+} oxidation state. ICP-AES measurements yielded an Al concentration of 8.1%, 15.2%, and 24.3% of Pb when the input Al/Pb ratios were 1, 2.5, and 4.5. Therefore, here the term "doping" is not appropriate in a strict sense, as it is generally applied for dopant concentrations in the low percent or subpercent range. It is noteworthy that the same doping procedure but with the aluminum precursor ($AlBr_3$) dissolved in toluene instead of dibromomethane resulted in no Al^{3+} signal (Figure 4.3b). In this case, no spectral shifts were observed either, demonstrating that the doping process was unsuccessful. We hypothesize that this difference is due to the molecular structure of $AlBr_3$. In the solid-state, $AlBr_3$ molecules exist as the dimer Al_2Br_6 (Figure 4.3b, inset). When these molecules are dissolved in aromatic solvents such as benzene or toluene, they retain their dimeric structure.[23] The steric hindrance as well as the coordination sphere of Al_2Br_6 make it unfavorable for Al^{3+} ions to be incorporated into the perovskite structure. In contrast, when CH_2Br_2 is used as the solvent, due to the strong nucleophilicity of the bromide group, it can coordinate more easily with Al2Br6 and possibly dissociate the dimer into the $AlBr_3$ monomer or $AlBr^{4-}$ ion, both of which can be inserted more easily into the host lattice. Although no direct reference for CH_2Br_2 was found, molecular weight determination and conductivity measurements of $AlBr_3$ dissolved in similar solvents (C_2H_5Br or CH_3Br) agree with this hypothesis.[23-24]

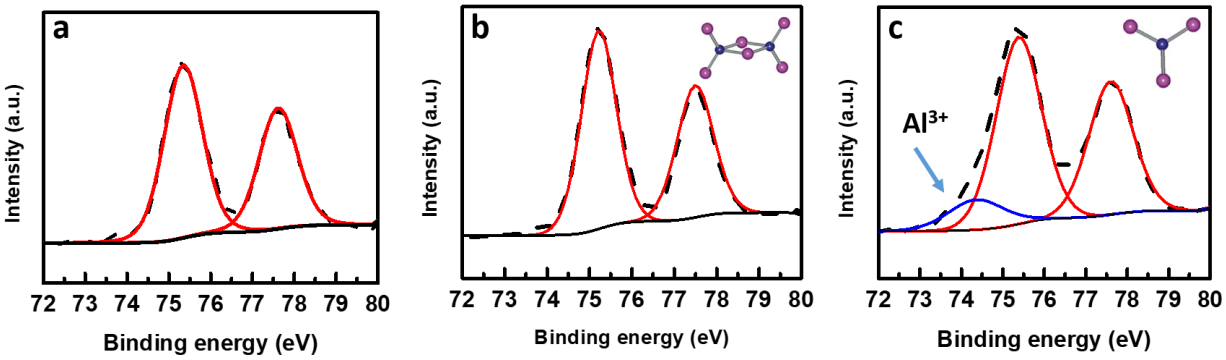

Figure 4.3. Cs 4d XPS spectra of (a) undoped $CsPbBr_3$ NCs, and doped NCs (Al/Pb input ratio: 2.5) using $AlBr_3$/toluene (b) and $AlBr_3/CH_2Br_2$ solutions for the doping process (c).

There are currently two explanations for the blueshift of the PL peak upon B-site doping in $CsPbBr_3$ NCs. For divalent cations such as Cd^{2+}, Sn^{2+}, and Zn^{2+}, de Mello Donegá and co-workers reported that doping created strain in the crystal lattice, as shown by the reduced lattice parameter of the doped NCs extracted from HAADF STEM analyses.[13] However, the effect of dopants with other valence states was not investigated. Conversely, for doping with Al^{3+}, Liu et al. proposed that the substitution of Pb^{2+} with Al^{3+} extended the band gap of the material and introduced a new level within the band gap.[19] The role of lattice contraction did not play a predominant role in this scenario for explaining the observed spectral shifts.

To elucidate this point in our case, powder X-ray diffraction on a series of samples with different doping levels was performed (Figure 4.4). Figure 4.4a provides evidence for the differences in the relative diffraction peak intensities between the undoped and doped samples. Due to their shape, $CsPbBr_3$ NCs are known to adopt a preferential orientation when deposited on a flat surface. The

hypothesis of an altered surface for the doped NCs suggested from TEM observations can explain different degrees of preferential orientation for the different samples, leading to differences in the relative diffraction peak intensities. This was confirmed by X-ray diffraction measurements performed in a capillary configuration (cf. Figure 4.5), which is known to favor random orientation of the crystallites, where the relative peak intensities are coherent with the reference pattern. As expected, compared to the undoped NCs, the diffraction peaks of the doped NCs (Al/Pb input ratio: 4.5) showed a shift to higher angles (Figure 4.4a). Since the ionic radius of Al^{3+} is significantly smaller than Pb^{2+}, this shift can be a sign of the lattice contraction induced by the substitution of Pb^{2+} with Al^{3+}.

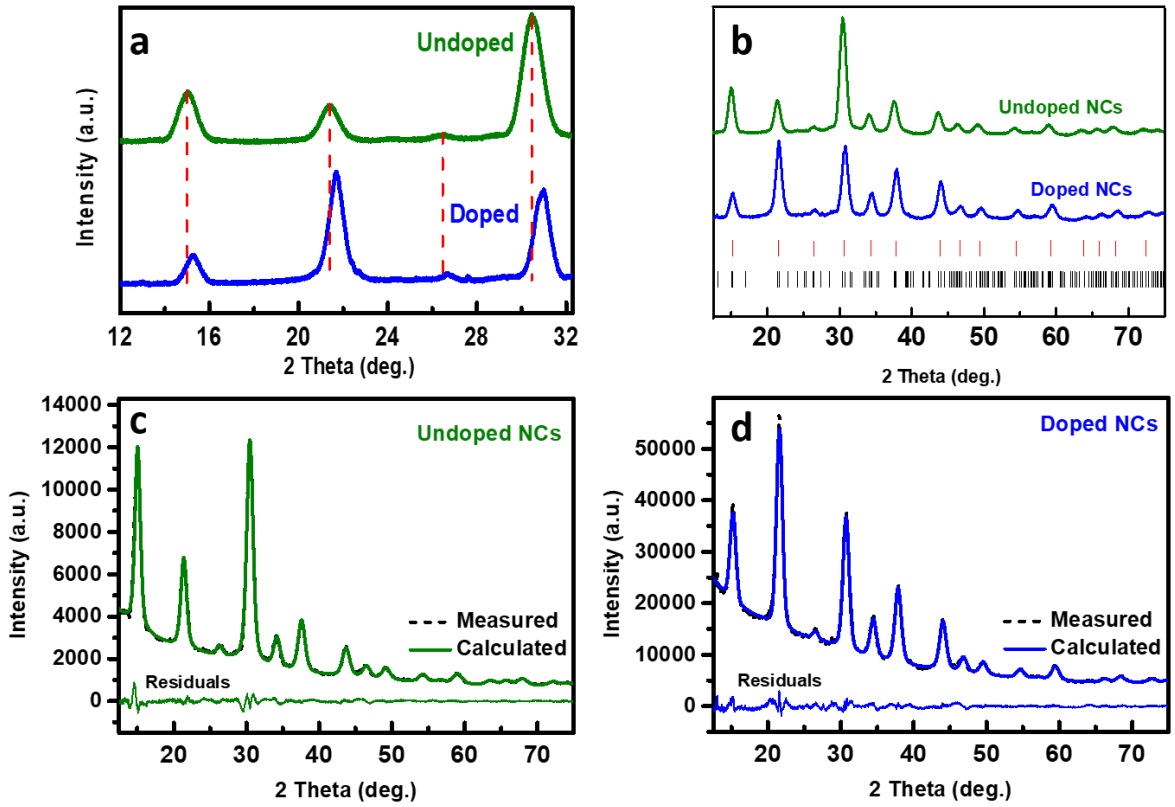

Figure 4.4. a) Zoom into the X-ray diffractograms of doped and undoped $CsPbBr_3$ NCs highlighting the shift of the diffraction peaks upon Al^{3+} doping (Al/Pb input ratio: 4.5), b) XRD patterns of the doped and undoped NCs, with the red and black bars indicating the peak positions of the cubic and orthorhombic reference patterns, respectively, c, d) Le Bail refinement of the cubic structure for the undoped (c) and doped (d) NCs.

At a first glance, the XRD patterns of both the undoped and doped NCs correspond to that of $CsPbBr_3$ in the cubic phase (ICDD 00-054-0752) (Figure 4.4b). However, two weak signals at 23° and 28.5° are visible, which can be assigned to the diffraction of the (120) and (122) planes of the $CsPbBr_3$ orthorhombic phase (ICDD 04-014-9676). While the reported phase of $CsPbBr_3$ NCs at room temperature is indeed orthorhombic,[25] we chose to consider the cubic structure. While it also accounts for the main features of the diffraction pattern, it has only one lattice parameter value to refine, as opposed to three values for the orthorhombic structure. As such, using the cubic structure can lead to better precision in the determination of the lattice parameters by Le Bail refinement (Figure 4.4c, d). Moreover, it allows a more straightforward comparison of our result with the similar

work in the literature.[13] The calculated patterns fit well with the measured diffraction patterns for both the doped and undoped NCs showing only slight mismatches at 15° and 30.4° due to the use of the cubic structure instead of the orthorhombic one for the refinement. The refined lattice parameter of the undoped NCs is 5.84 Å, which decreases to 5.81 Å upon doping with an Al/Pb input ratio of 4.5. As the amount of dopant was increased, the lattice contraction increased accordingly.

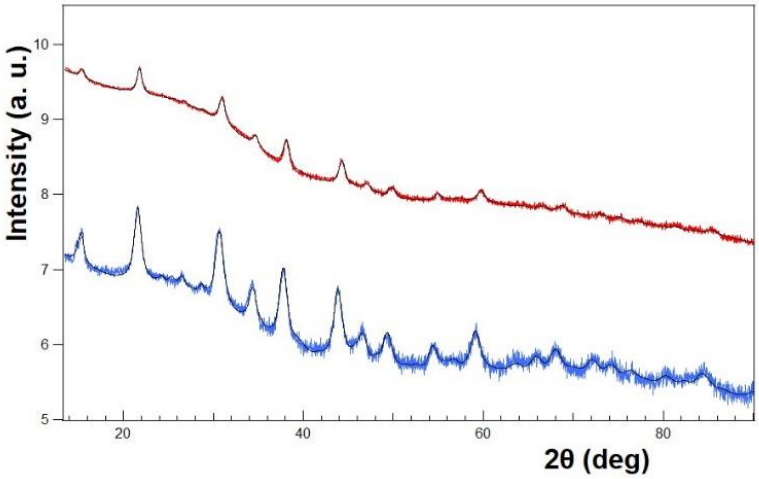

Figure 4.5. X-ray diffraction patterns obtained in capillary configuration for undoped and doped (Al/Pb input ratio 2.5) samples, respectively in blue and red. In black, calculated patterns obtained from Rietveld refinement considering orthorhombic structure and resulting in the following sets of lattice parameter values: (a = 8.22 Å, b = 8.30 Å, c = 11.79 Å) for the undoped sample, in good agreement with ICDD 04-014-9676; (a = 8.22 Å, b = 8.23 Å, c = 11.57 Å) for the doped sample.

Using the data from the Le Bail refinement of samples with different doping levels, we constructed a relationship between the PL peak energy and the lattice parameter (Figure 4.6a). The fitted line shows an inverse linear relationship between the lattice parameter and the PL peak energy. This trend is similar to that reported in the study of de Mello Donegá et al.[13], but with different slopes of −1.96 eV/Å (this work) and −1.61 eV/Å (ref. 13). The apparent discrepancy in the lattice parameters of samples with similar PL energy is due to the different experimental methods used: while in this work the lattice parameters were extracted from X-ray diffraction, the literature study used electron diffraction. The observed lattice contraction with Al^{3+} (0.55%, ionic radius 54 pm, Al/Pb input ratio of 4.5) is similar to that in ref. 13 for Cd^{2+} (0.5%, ionic radius 95 pm), albeit smaller than that for Zn^{2+} (0.7%, ionic radius 74 pm). In comparison with the divalent cations used at similar nominal doping levels, Al^{3+} thus induces a lower lattice contraction than expected given its small ionic radius.

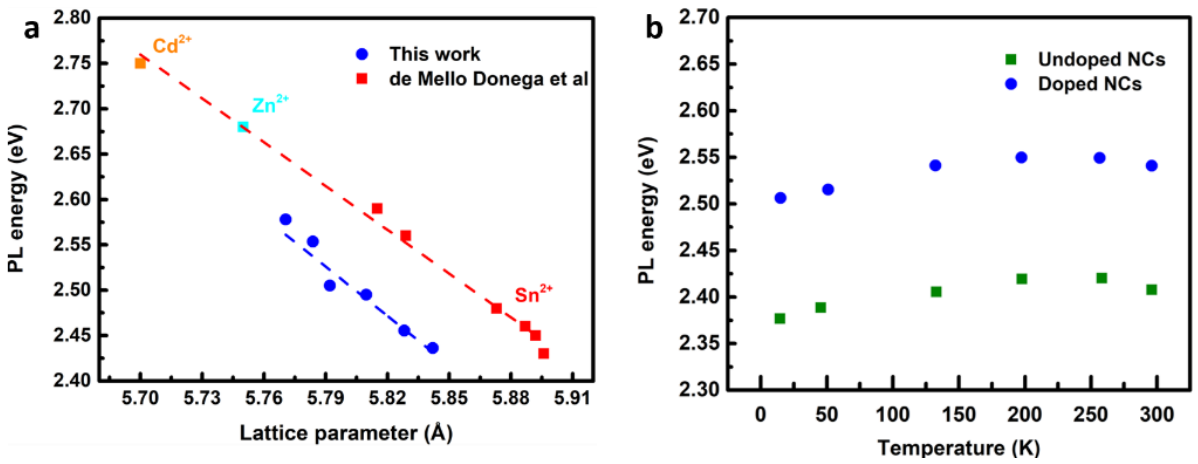

Figure 4.6. a) PL peak position as a function of the lattice parameter for NCs doped with Al^{3+} and with divalent dopants (relevant data were taken from Figure 6, ref. 13), b) Temperature dependence of the PL peak position of undoped and doped NCs (Al/Pb input ratio: 4.5).

The observed correlation between emission energy and lattice constant, although in line with ref. 13, stands out against other literature reports.[26-28] Unlike conventional NCs of II− VI or III−V compounds, in lead halide perovskite NCs both band edges are composed of antibonding orbitals.[29-30] When the lattice contracts, we have shrinkage of the Pb−Br bond length, hence stronger antibonding coupling between Pb-6p and Br-4s orbitals for the conduction band minimum (CBM) and between Pb-6s and Br-4p orbitals for the valence band maximum (VBM). Therefore, both CBM and VBM will shift to higher energies. However, the CBM shift is much weaker due to negligible Br-4s hybridization with Pb-6p, so that the overall band gap becomes narrower and a redshift of the PL peak is observed when the lattice parameter decreases, e.g., through temperature decrease.[26-28, 31] In our case, this behavior is indeed observed for temperatures below approximately 200 K (Figure 4.6b). Yet there is a change in the slope, and when decreasing the temperature in the range from 300 to 200 K, the PL energy first increases. Intriguingly, the doped NCs follow the same trend as the undoped NCs, with the PL energy difference between both samples remaining essentially constant across the whole investigated temperature range. Boziki et al. demonstrated that in $CsPbBr_3$ nanocrystals a large distribution of Cs−Pb distances exists in a broad temperature range, which means that the crystalline environment is not uniform, inducing a distribution of band gap values due to deformation and octahedral tilting.[32] Coming back to the origin of the spectral shifts observed upon doping (Figure 4.1 c, d), the replacement of Pb with significantly smaller Al ions produces not only local lattice shrinkage but also octahedral tilting with respect to the octahedra network. Studies of pressure effects on perovskites have clearly shown that the band gap increase related to tilting is dominant over the decrease due to lattice shrinkage.[33-34] Hence, this effect can explain the band gap increase observed here in the cases of Al-doping and lowering of the temperature in the 300−200 K range.

In a parallel study, we investigated the crystal structure of undoped and doped $CsPbBr_3$ NCs as a function of the temperature. With no phase transition occurring for temperatures below 361 K, this measurement provides us with the opportunity to interpret the change in lattice parameters as the effects of pure lattice contraction. Additionally, by comparison between the undoped and doped NCs, we could gain more insight into the effects of the Al^{3+} dopant on the perovskite structure.

Using undoped and 20% Al-doped $CsPbBr_3$ NCs (Al/Pb feed ratio 4.5), we measured their diffraction patterns from 80 K to 300 K, and then increased the temperature to 361 K and 443 K to induce the

phase transitions to the tetragonal and cubic phases, respectively.[35] We then kept the samples at 443 K overnight to sinter the nanocrystals into micrometer-sized particles. Finally, we repeated the measurements from 80 K to 300 K. The main purpose of annealing the nanocrystals is to get the bulk material for an *in situ* precise reference, since the diffraction peaks of nanomaterials experience a high degree of broadening because of the decrease in the coherent scattering domain size. As such, overlapping between neighbor peaks occurs, complicating the pattern analysis. By first measuring the diffraction pattern of the nanocrystals, then increasing their size and repeating the same measurements, we would be able to compare the result for the nanocrystals with the (supposedly) bulk reference.

Figure 4.7 plots the evolution of the unit cell volume with the temperature. Two regimes can be identified for the undoped NCs from 80 – 300 K (Figure 4.7b). Below 200 K, the cell volume increases linearly with the temperature at a rate of 0.026 ± 0.001 $Å^3$/K, whereas above 200 K, the increase becomes faster (0.052 ± 0.006 $Å^3$/K), but with less agreement to the linear fit. When correlated to the change in the photoluminescence peak position with temperature, the high and low-temperature regimes correspond to the increase and decrease in PL energy, respectively, with 200 K being the common transition point (Figure 4.6b). The anomaly near this temperature has been discussed previously.[36] Changes in the local octahedral environment, expansion coefficient, and dielectric response were observed, implying that there was an isostructural phase transition at around 220 K, which involved a redistribution of Pb-Br bond distances. It is possible that as this happens, the population of optical phonon modes increases. The resulting increased electron-phonon coupling above this temperature leads to the observed optical properties of $CsPbBr_3$ NCs discussed above.[37] The doped NCs share both the structural and optical behavior in the 200 – 300 K regime, but from 80 K to 200 K, the cell volume increases before unexpectedly probably staying constant (120 – 200 K), (Figure 4.7e). In contrast to the undoped NCs where the lattice expansion and PL energy shift are in good agreement below 200 K, the shift in the doped NCs in the 120 – 200 K range cannot be accounted for by only the cell volume. Indeed, the slope of the PL energy evolution in this temperature range is lower than in the 10 - 120 K range (Figure 4.8).

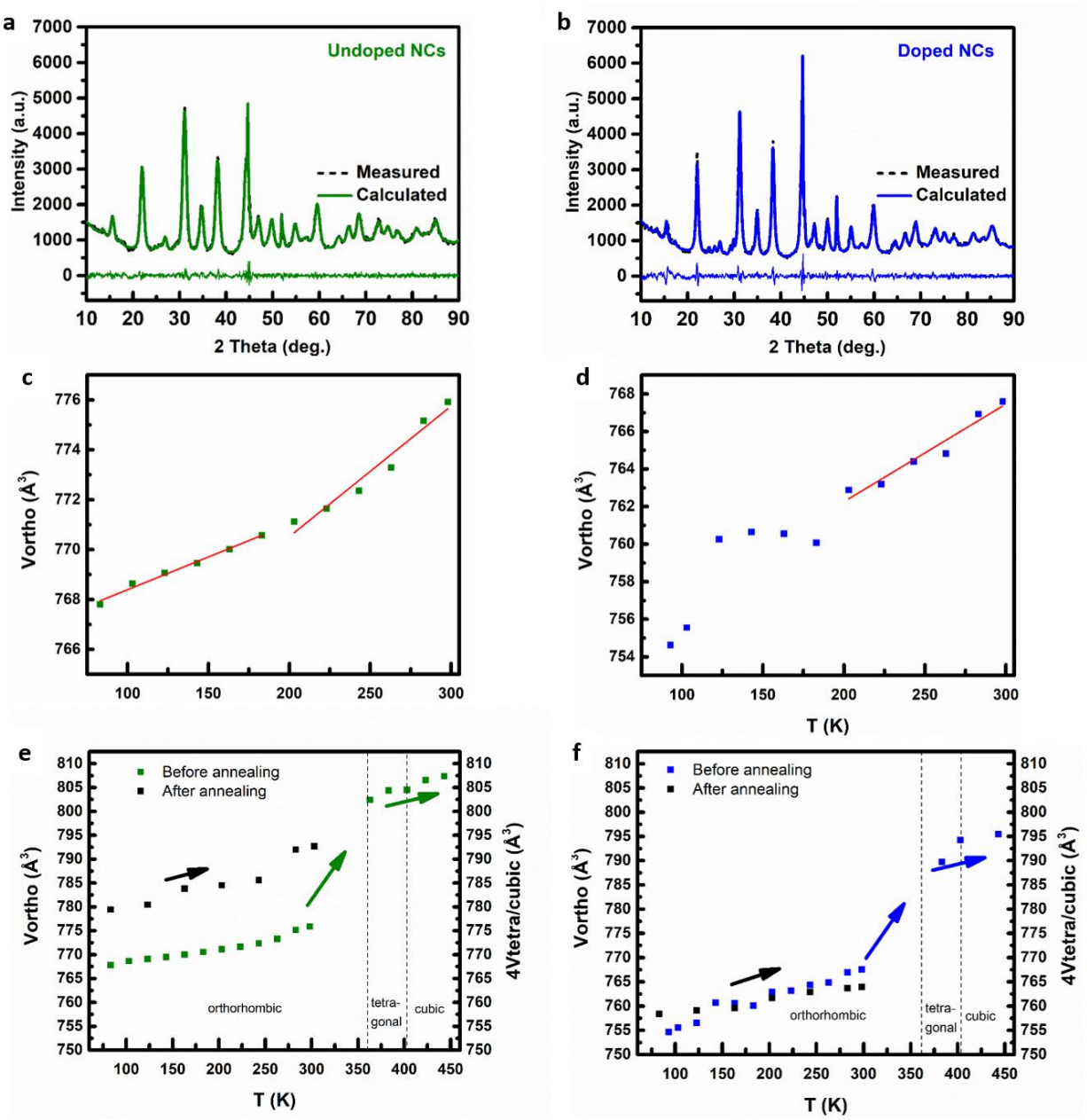

Figure 4.7. Le Bail refinement for samples measured at 300 K (a, b), and cell volume as a function of the temperature for undoped (green) and doped (blue) NCs. c, d) Cell volume determined from XRD measurements performed in a temperature range from 80 to 300 K; e, f) temperature increase from 80 to 300 K, then to the temperatures where the phase transitions occur (361 K and 443 K, keeping this temperature overnight for annealing), and finally repetition of the measurement from 80 to 300 K. The volume of the crystal in tetragonal and cubic phases were scaled up to provide a better comparison to the volume in orthorhombic phase.

Comparing the undoped and doped NCs in the entire temperature range, it can be seen that the lattice parameters of the doped sample are consistently lower than those of the undoped NCs (Figure 4.7c, f). This feature is consistent with the constant PL energy difference observed previously. One noticeable difference is the behavior of the undoped NCs after the phase transition. Compared to the doped NCs, for which the cell volume remains more or less identical after annealing, the volume of the undoped NCs increases after annealing. While this result is contradicting the established data for

bulk and 12 nm $CsPbBr_3$ NCs,[25] the cell volume of the crystal after annealing (792.71 Å^3 at 300 K) is in good agreement with that of bulk $CsPbBr_3$ prepared by ball milling (792.87 Å^3 at 300 K).[38]

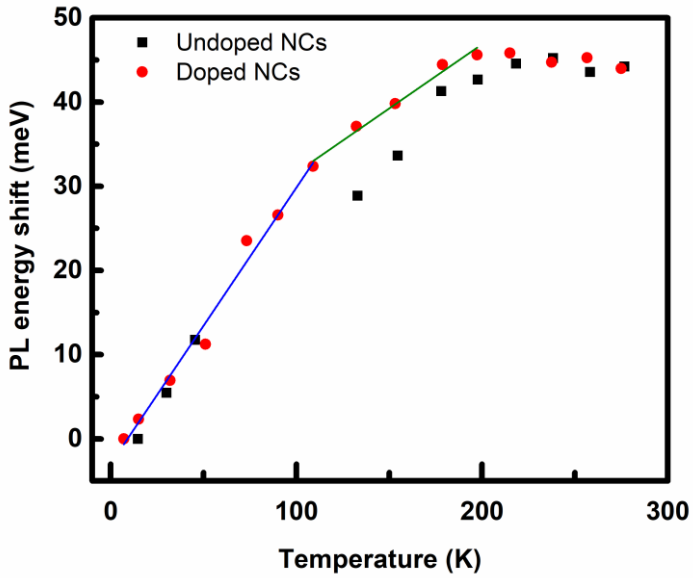

Figure 4.8. Comparative temperature-dependent PL energy shift of undoped and doped NCs, the straight lines are meant to guide the eyes.

During the measurement, we noticed the appearance of additional diffraction peaks at 29.8° and 33.7° after the phase transition (Figure 4.9a). They are likely the peaks of $CsPb_2Br_5$ crystals (ICDD 04-024-4338), obtained as a side product from thermal annealing.[39] As the temperature increases, the surface ligands start to desorb from the NCs. Since the $CsPbBr_3$ NCs are terminated by CsBr,[40-41] this desorption can also lead to the loss of Cs^+ and Br^- ions. As a consequence, $CsPb_2Br_5$ irreversibly forms, and the degree of conversion to this composition depends on the length of the ligands, which inversely correlates with their volatility. It is worth noting that even though $CsPb_2Br_5$ also appears in the case of doped NCs, its relative amount compared to $CsPbBr_3$ was lower (cf. Figure 4.9b-c). One possible explanation is that due to the lattice contraction induced by Al^{3+}, surface ions are more tightly bound, preventing them from desorption and subsequent $CsPb_2Br_5$ formation. Since the $CsPbBr_3$ microcrystals now contains $CsPb_2Br_5$ crystal domains, the structural behavior is no longer representative of pure-phase $CsPbBr_3$. Therefore, we cannot consider the data after annealing as reference bulk data as it was originally intended.

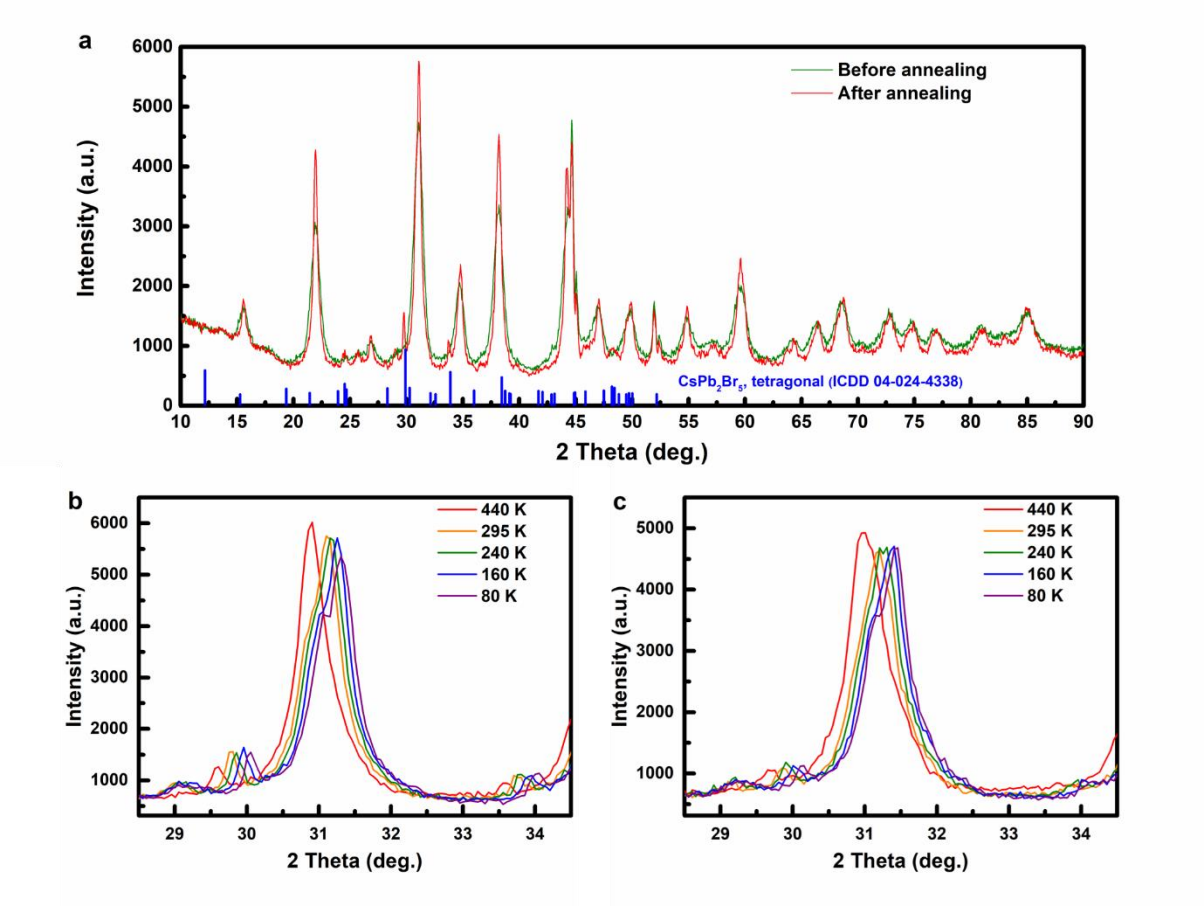

Figure 4.9. a) XRD patterns of undoped NCs at 300 K before and after annealing, the evolution of the observable $CsPb_2Br_5$ peaks with temperature for undoped (b) and doped (c) NCs.

An important question related to the doping of aluminum in $CsPbBr_3$ NCs is the position of the dopant within the host. Previous works on divalent and trivalent dopants have postulated that the dopant generally substitutes Pb^{2+} despite the huge difference in ionic size.[13, 18] It is a highly plausible hypothesis since the charge imbalance introduced by the dopant is minimized this way. However, for Al-doped $CsPbBr_3$ NCs, we questioned this idea. Even though the difference in ionic radii between Al^{3+} and Pb^{2+} is larger than for any previous dopant, we recorded an Al/Pb ratio as high as 24.3% without any significant change in the structural behavior of the host material. Therefore, we simulated the expected diffraction patterns of $CsAl_xPb_{1-x}Br_3$ NCs where x = 0%, 5%, and 20% (corresponding to Al/Pb ratio of 25%), assuming that Al atoms occupy the same crystallographic site as Pb ones. Finally, we compare them with the experimental data of 20% Al-doped NCs. As the Al content increases from 0% to 20%, the relative intensities of the diffraction peaks generally decrease, except for the peaks from 24° to 33° (Figure 4.10). The difference between the two simulated patterns is most clearly visible in the 2θ range from 15° to 50°. Comparisons to the experimental pattern reveals that the simulated pattern with 0% Al is in better agreement with the measured data than with 20% Al. This comparison demonstrates that substitution of Pb^{2+} by Al^{3+} is not the preponderant doping mechanism in our case. The conclusion is also supported by elemental analysis, with the Cs/Pb atomic ratio before (0.75 ± 0.04) and after (0.77 ± 0.04) Al^{3+} doping being almost identical. Since Al^{3+} has a small size, A-site doping cannot satisfy the condition imposed by the tolerance factor. The most plausible hypothesis is that Al^{3+} ions occupy interstitial sites. Indeed, this tendency has been shown for small alkali cations such as Li^+ and Na^+, and charge neutrality is maintained thanks to the presence of charged defects, for example

vacancies, in the host lattice.[42] However, incorporation of such ions can lead to lattice expansion instead of contraction. Therefore, the diffraction pattern of $CsPbBr_3$ with Al^{3+} in interstitial sites will be simulated to verify this hypothesis.

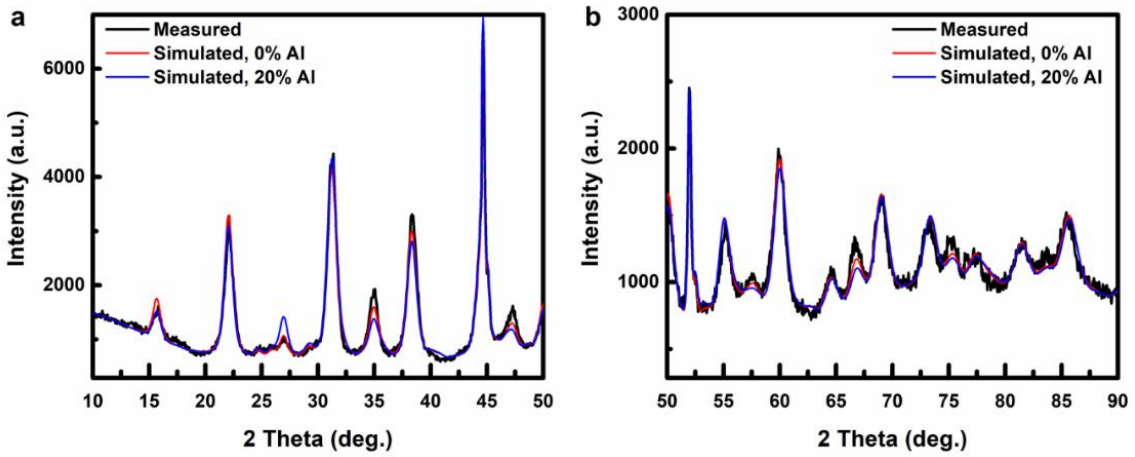

Figure 4.10. Simulated diffraction patterns of Al-doped $CsPbBr_3$ NCs using Rietveld refinement with different Al contents (red, blue) in comparison with the experimental data for 20%-Al doped $CsPbBr_3$ NCs.

Mn-doped $CsPbBr_3$ NCs

To observe the effects of the sp-d exchange and the resulting giant Zeeman effect, only free spins from isolated Mn^{2+} ions are relevant. This consideration imposes an upper limit on the dopant concentration, above which all dopants experience increased antiferromagnetic coupling due to the superexchange. For randomly distributed dopants at low concentration, the effective concentration x_{eff} can be estimated from the real concentration x by the equation $x_{eff} = x(1-x)^n$, where n is the number of nearest neighbors. In conventional II-VI nanocrystals with wurtzite or zinc blende structures, each cation has 12 nearest neighbors, x_{eff} is maximized at ~3% when x is ~8%. In the perovskite structure, the number of nearest neighbors is only 6, which in principle can extend the absolute dopant concentration (x_{eff} is maximized at ~5.7% when x is ~14%).

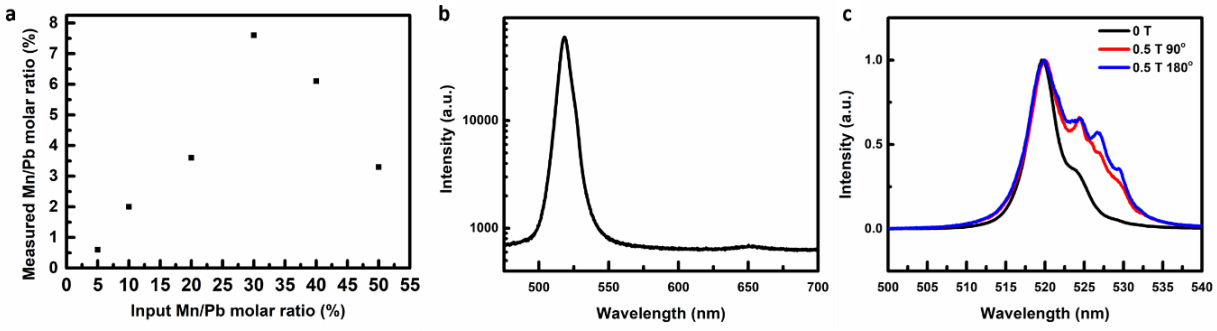

Figure 4.11. a) Relationship between input and measured Mn/Pb molar ratio, b) Photoluminescence spectrum of $CsPbBr_3$ NCs doped with a Mn/Pb feed ratio of 0.2 (2% doping level from elemental analysis), b) Spectra of the band-edge emission at 0 and 0.5 T with different circular polarizations, revealing that no change in the emission energy occurred under magnetic field and at different polarization angles. The measurements were performed at 6 K.

At low dopant concentrations (Mn/Pb feed ratio <0.5), we recorded the Mn signal with elemental analysis, with the final Mn/Pb ratio being typically 4 to 8 times lower than the feed ratio, leading to a nominal doping level from 0.5%–7.5% (Figure 4.11a). We then performed PL measurement at 6 K, as such low temperature was required to observe the Mn d–d transition in $CsPbBr_3$. From here on, all the subsequent PL measurements were carried out at this temperature. In the PL spectra, we failed to observe the Mn d–d transition signal at ~620 nm at all studied concentrations (Figure 4.11b). For a sample with a 2% nominal doping level, a very low intensity signal at 650 nm can be detected, however, its origin remains unknown as the spectral position does not correspond to that expected for Mn^{2+}. The Mn^{2+} ions likely resided on the surface of the NCs, since the related optical transition should still be visible even at a nominal doping level as low as 2%.[22] Nevertheless, we tried to study the effect of the magnetic field on the $CsPbBr_3$ band-edge emission. The small difference in the emission spectra at 0 T and 0.5 T was due to the inhomogeneity of the sample surface, but the main band-edge emission energy was unchanged. Furthermore, there was no spectral shift at different circular polarizations. Though many factors could contribute to the failure of this experiment, we first focused on the lack of Mn emission from the doped NCs. As mentioned before, this is a sign that the doped Mn^{2+} was not incorporated inside the host NCs but rather adsorbed on the surface. For the dopant to diffuse in the bulk, either the reaction time or the dopant feed concentration should be increased (or both).

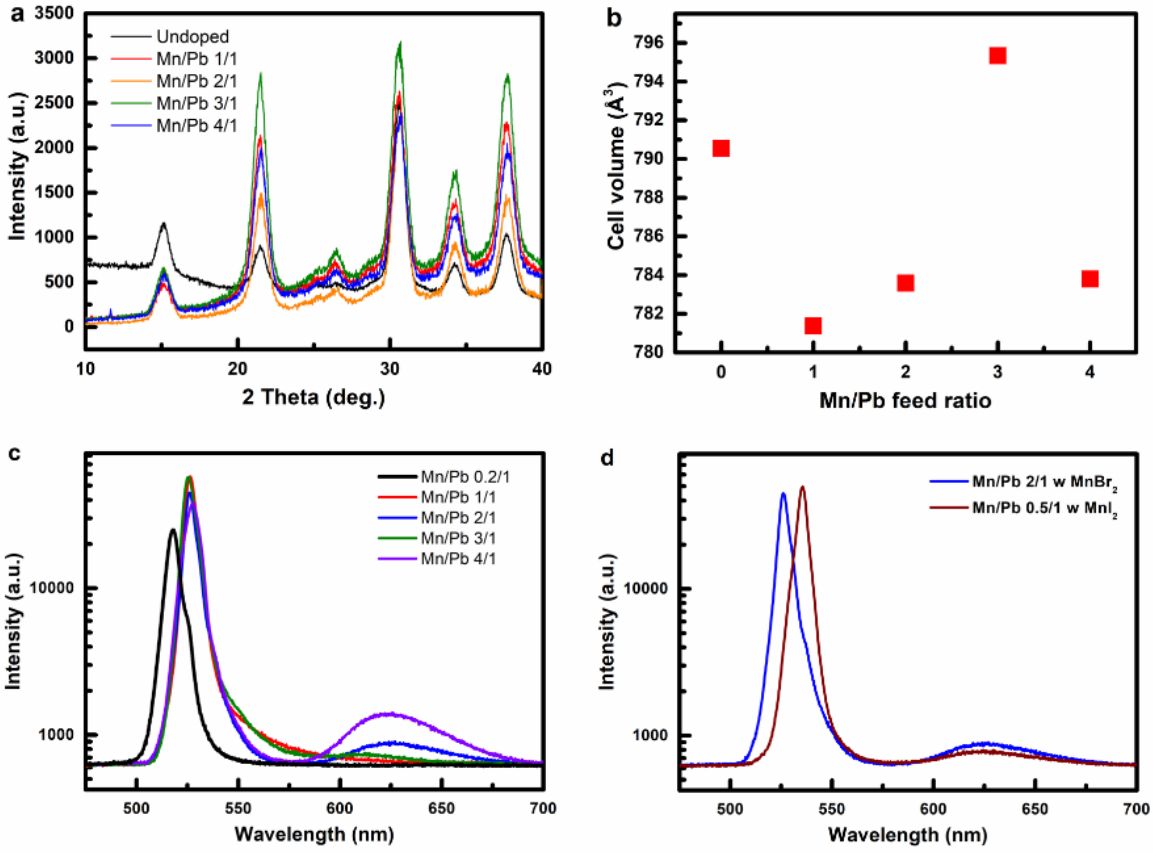

Figure 4.12. a) XRD patterns of Mn-doped $CsPbBr_3$ NCs with different Mn/Pb feed ratios, b) Cell volume as a function of the Mn/Pb feed ratio, c) Photoluminescence spectra showing the band-edge and Mn transitions for different Mn/Pb feed ratios, d) Photoluminescence spectra of Mn-doped $CsPbBr_3$ and $CsPb(Br/I)_3$ NCs.

We then decided to increase the Mn/Pb feed ratio up to 4, as well as increase the reaction time to 1 h. Unfortunately, elemental analysis has not been performed to assess the nominal doping level. Nevertheless, we found no significant effects on the $CsPbBr_3$ crystal structure even though these ratios far exceed what can be considered doping. In general, we did not find any observable peak shift in the diffraction pattern (Figure 4.12a). However, Le Bail refinement demonstrated that the cell volume decreased after doping, except for the ratio of 3/1. This decrease is in agreement with the lattice contraction associated with Mn^{2+} doping.[22] The emission of the characteristic Mn d–d transition was also detected in these samples at 623 nm (Figure 4.12c). However, only the 2/1 and 4/1 samples showed clear peaks, the other samples showed only a shoulder at 611 nm. Considering that the emission tails of the 1/1 and 3/1 samples had higher intensity than the 2/1 and 4/1 ones, the energy of the Mn transition likely overlapped with the band edge emission.

Mn-doping using Mn halides also allowed for tuning the band gap of the host NCs. Since the hybridization between the d levels of Mn and the s and p levels of the host depends on their relative energy, it is essential to be able to control the band edge positions of the host NCs. It has been established that when $MnCl_2$ is used as the Mn precursor to dope $CsPbBr_3$, incorporation of Mn^{2+} is accompanied by anion exchange.[43] As a result the doped NCs exhibit a larger band gap due to the mixed halide $CsPb(Cl,Br)_3$ structure. We applied the same strategy, using MnI_2 to introduce iodide into the $CsPbBr_3$ host and hence reduce the band gap of the perovskite NCs. With a lower CBM, the relevant energy levels of $CsPb(Br/I)_3$ are expected to be closer to those of Mn^{2+}. At an Mn/Pb feed ratio of 0.5, the band edge emission shifts from its original position of 526 nm to 535.6 nm (Figure 4.12d). It is noteworthy that even at such a low feed ratio, the intensity of the resulting Mn d-d transition is comparable to that of the doped NCs using $MnBr_2$ with a Mn/Pb ratio of 2. It indicates that either the anion exchange has facilitated the Mn-doping process or the excitation transfer to Mn was enhanced by changing the band gap.

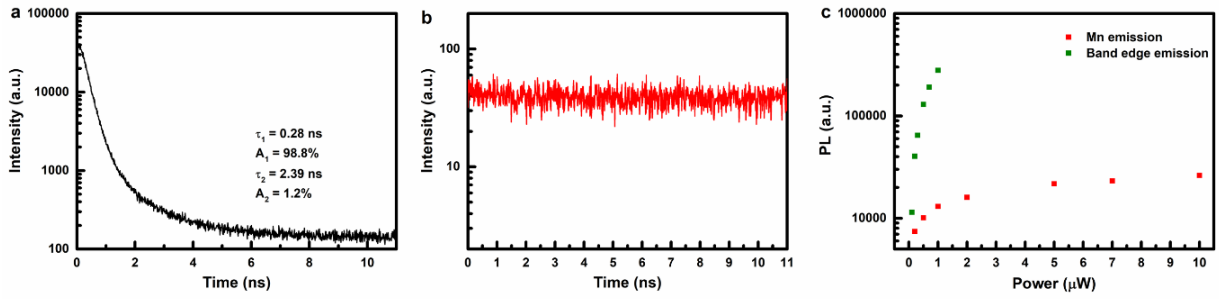

Figure 4.13. Photoluminescence decay curves of the band-edge emission recorded at 528 nm (a) and the Mn d–d transition recorded at 623 nm (b) of Mn:$CsPbBr_3$ NCs having a Mn/Pb feed ratio of 2 and using $MnBr_2$ as the dopant precursor. c) Emission intensity as a function of the irradiation power.

One of the challenges for the characterization of the Mn-doped $CsPbBr_3$ NCs is that the Mn d–d transition cannot be observed at room temperature. For this reason, all the photoluminescence measurements have been conducted at 6 K. $CsPbBr_3$ NCs show a near single exponential decay of charge carries with an average lifetime of 0.3 ns (Figure 4.13a). On the contrary, the Mn d–d transistion is typically very long (μs or ms range) and has much lower intensity, because it is forbidden according to the selection rules (Figure 4.13b). Therefore, at room temperature, back energy transfer from the Mn $^4T_1$ state to $CsPbBr_3$ can occur before the decay to the Mn ground state, quenching the luminescence. Even at 6 K, the slow decay limits the photoluminescence of this transition. Its intensity

quickly reaches a plateau when the excitation energy increases from 0 to 10 µW, in contrast to the band-edge emission (Figure 4.13c).

The emission spectrum of Mn-doped NCs shows two lines with different intensities, and their relative intensities changed randomly with different points of measurements. These two lines could be attributed to NCs with two size distributions as their excited charge carrier lifetimes are similar. Despite the presence of the Mn emission peak, specific magneto-optical properties of the Mn-doped $CsPbBr_3$ NCs still were not observable (Figure 4.14a). The band edge emission energy did not shift under an applied field of 0.5 T, and there was no polarization of light. One reason for our inability to observe the shift is orientation of the doped NCs. In a large ensemble such as a thin film, each NC would orient randomly, and combined with the inhomogeneous broadening, small energy shifts would become unobservable. Because of the limitation of our experimental setup, a stronger magnet could not be used, while the magnetic field usually employed in such types of experiments can be as high as 20 T.[44]

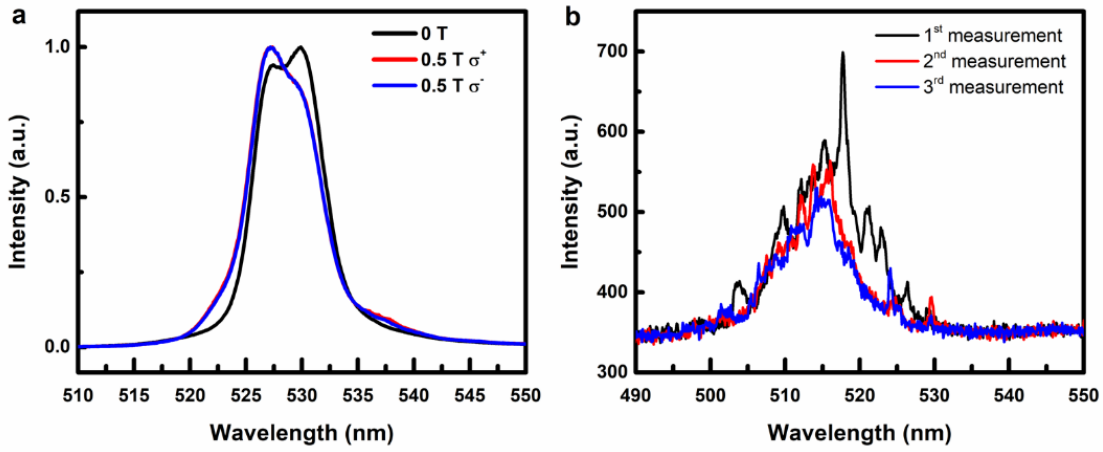

Figure 4.14. a) Spectra of the band-edge emission at 0 and 0.5 T with different circular polarizations for a thin film of Mn-doped $CsPbBr_3$ NCs. b) Successive measurements on small clusters of Mn-doped $CsPbBr_3$ NCs under an applied field of 0.5 T.

To reduce the spectral broadening, we therefore measured clusters of NCs instead of large ensembles. Though the peaks of individual NCs became easier to be resolved, this measurement encountered the problem of reproducibility (Figure 4.14b). As fluorescence intermittency/blinking is significant in $CsPbBr_3$ NCs (as in most other types of fluorescent NCs), the emission spectra fluctuated strongly with each measurement, making it impossible to follow the evolution of any single peak. On the other hand, the possibility that the sp–d exchange between Mn and $CsPbBr_3$ is simply inefficient in the studied samples cannot be ruled out either. In this case, the use of $CsPb(Br/I)_3$ mixed halide perovskite NCs as the host could potentially improve this interaction so that the giant Zeeman splitting can be observed.

Conclusion

In conclusion, we successfully doped $CsPbBr_3$ NCs with Al^{3+} ions using a facile post-synthetic treatment at room temperature implying $AlBr_3$ dissolved in dibromomethane. The doped NCs exhibited a blue-shift in the absorption and PL spectra, which is tunable with the Al^{3+} dopant concentration and stable over time. Le Bail refinement of the XRD data evidenced a lattice contraction when the dopant was introduced into the $CsPbBr_3$ host lattice and revealed a linear relationship between the PL energy (and

hence band gap of the NCs) and the lattice parameter with a slope of −1.96 eV/Å. This behavior is opposed to the established relationship between band gap and lattice parameters for perovskite NCs. Therefore, additional effects such as octahedral tilting and structural disorder need to be considered for explaining the spectral shifts of $CsPbBr_3$ NCs observed upon Al^{3+} doping.

The post-synthetic doping was also successful in the case of Mn^{2+}, using Mn halides as the precursors, although at Mn/Pb feed ratios < 0.5, the Mn d–d transition was not observed and no magneto-optical effect was recorded, either. At Mn/Pb feed ratios > 2, the d–d peak became visible at 4 K, and its intensity saturated quickly with increasing irradiation power. Nevertheless, we did not manage to observe the giant Zeeman splitting for Mn-doped $CsPbBr_3$ NCs deposited as a thin film or in form of small clusters of NCs, eventually due to the limited magnetic field achievable in our experiments (0.5 T). Additionally, we found that doping with Mn^{2+} can be facilitated by switching the dopant precursor from $MnBr_2$ to MnI_2. This exchange also decreased the band gap of the host NCs via halide exchange, which can strongly affect the sp–d coupling between Mn and $CsPbBr_3$ and make it more favorable for the observation of the giant Zeeman splitting.

References

1. Protesescu, L.; Yakunin, S.; Bodnarchuk, M. I.; Krieg, F.; Caputo, R.; Hendon, C. H.; Yang, R. X.; Walsh, A.; Kovalenko, M. V., Nanocrystals of Cesium Lead Halide Perovskites (CsPbX(3), X = Cl, Br, and I): Novel Optoelectronic Materials Showing Bright Emission with Wide Color Gamut. *Nano Lett.* **2015,** *15* (6), 3692-6.
2. Akkerman, Q. A.; D'Innocenzo, V.; Accornero, S.; Scarpellini, A.; Petrozza, A.; Prato, M.; Manna, L., Tuning the Optical Properties of Cesium Lead Halide Perovskite Nanocrystals by Anion Exchange Reactions. *J. Am. Chem. Soc.* **2015,** *137* (32), 10276-81.
3. Thapa, S.; Bhardwaj, K.; Basel, S.; Pradhan, S.; Eling, C. J.; Adawi, A. M.; Bouillard, J.-S. G.; Stasiuk, G. J.; Reiss, P.; Pariyar, A.; Tamang, S., Long-term ambient air-stable cubic CsPbBr3 perovskite quantum dots using molecular bromine. *Nanoscale Advances* **2019,** *1* (9), 3388-3391.
4. Braly, I. L.; Stoddard, R. J.; Rajagopal, A.; Uhl, A. R.; Katahara, J. K.; Jen, A. K. Y.; Hillhouse, H. W., Current-Induced Phase Segregation in Mixed Halide Hybrid Perovskites and its Impact on Two-Terminal Tandem Solar Cell Design. *Acs Energy Lett* **2017,** *2* (8), 1841-1847.
5. Duong, T.; Mulmudi, H. K.; Wu, Y.; Fu, X.; Shen, H.; Peng, J.; Wu, N.; Nguyen, H. T.; Macdonald, D.; Lockrey, M.; White, T. P.; Weber, K.; Catchpole, K., Light and Electrically Induced Phase Segregation and Its Impact on the Stability of Quadruple Cation High Bandgap Perovskite Solar Cells. *ACS applied materials & interfaces* **2017,** *9* (32), 26859-26866.
6. Zhang, H.; Fu, X.; Tang, Y.; Wang, H.; Zhang, C.; Yu, W. W.; Wang, X.; Zhang, Y.; Xiao, M., Phase segregation due to ion migration in all-inorganic mixed-halide perovskite nanocrystals. *Nature communications* **2019,** *10* (1), 1088.
7. Knight, A. J.; Herz, L. M., Preventing phase segregation in mixed-halide perovskites: a perspective. *Energy & Environmental Science* **2020,** *13* (7), 2024-2046.
8. Chen, Y.; Liu, Y.; Hong, M., Cation-doping matters in caesium lead halide perovskite nanocrystals: from physicochemical fundamentals to optoelectronic applications. *Nanoscale* **2020,** *12* (23), 12228-12248.
9. Aldakov, D.; Reiss, P., Safer-by-Design Fluorescent Nanocrystals: Metal Halide Perovskites vs Semiconductor Quantum Dots. *The Journal of Physical Chemistry C* **2019,** *123* (20), 12527-12541.
10. Mir, W. J.; Swarnkar, A.; Nag, A., Postsynthesis Mn-doping in CsPbI3 nanocrystals to stabilize the black perovskite phase. *Nanoscale* **2019,** *11* (10), 4278-4286.
11. Qiao, T.; Parobek, D.; Dong, Y.; Ha, E.; Son, D. H., Photoinduced Mn doping in cesium lead halide perovskite nanocrystals. *Nanoscale* **2019,** *11* (12), 5247-5253.
12. Imran, M.; Ramade, J.; Di Stasio, F.; De Franco, M.; Buha, J.; Van Aert, S.; Goldoni, L.; Lauciello, S.; Prato, M.; Infante, I.; Bals, S.; Manna, L., Alloy CsCd x Pb1-x Br3 Perovskite Nanocrystals: The Role of Surface Passivation in Preserving Composition and Blue Emission. *Chem. Mater.* **2020,** *32* (24), 10641-10652.

13. van der Stam, W.; Geuchies, J. J.; Altantzis, T.; van den Bos, K. H.; Meeldijk, J. D.; Van Aert, S.; Bals, S.; Vanmaekelbergh, D.; de Mello Donega, C., Highly Emissive Divalent-Ion-Doped Colloidal CsPb1-xMxBr3 Perovskite Nanocrystals through Cation Exchange. *J. Am. Chem. Soc.* **2017,** *139* (11), 4087-4097.
14. Yao, J. S.; Ge, J.; Han, B. N.; Wang, K. H.; Yao, H. B.; Yu, H. L.; Li, J. H.; Zhu, B. S.; Song, J. Z.; Chen, C.; Zhang, Q.; Zeng, H. B.; Luo, Y.; Yu, S. H., Ce(3+)-Doping to Modulate Photoluminescence Kinetics for Efficient CsPbBr3 Nanocrystals Based Light-Emitting Diodes. *J. Am. Chem. Soc.* **2018,** *140* (10), 3626-3634.
15. Lozhkina, O. A.; Murashkina, A. A.; Shilovskikh, V. V.; Kapitonov, Y. V.; Ryabchuk, V. K.; Emeline, A. V.; Miyasaka, T., Invalidity of Band-Gap Engineering Concept for Bi(3+) Heterovalent Doping in CsPbBr3 Halide Perovskite. *The journal of physical chemistry letters* **2018,** *9* (18), 5408-5411.
16. Lu, C. H.; Biesold-McGee, G. V.; Liu, Y.; Kang, Z.; Lin, Z., Doping and ion substitution in colloidal metal halide perovskite nanocrystals. *Chem. Soc. Rev.* **2020,** *49* (14), 4953-5007.
17. Begum, R.; Parida, M. R.; Abdelhady, A. L.; Murali, B.; Alyami, N. M.; Ahmed, G. H.; Hedhili, M. N.; Bakr, O. M.; Mohammed, O. F., Engineering Interfacial Charge Transfer in CsPbBr3 Perovskite Nanocrystals by Heterovalent Doping. *J. Am. Chem. Soc.* **2017,** *139* (2), 731-737.
18. Zhou, D.; Liu, D.; Pan, G.; Chen, X.; Li, D.; Xu, W.; Bai, X.; Song, H., Cerium and Ytterbium Codoped Halide Perovskite Quantum Dots: A Novel and Efficient Downconverter for Improving the Performance of Silicon Solar Cells. *Adv. Mater.* **2017,** *29* (42).
19. Liu, M.; Zhong, G.; Yin, Y.; Miao, J.; Li, K.; Wang, C.; Xu, X.; Shen, C.; Meng, H., Aluminum-Doped Cesium Lead Bromide Perovskite Nanocrystals with Stable Blue Photoluminescence Used for Display Backlight. *Advanced science* **2017,** *4* (11), 1700335.
20. Nafradi, B.; Szirmai, P.; Spina, M.; Lee, H.; Yazyev, O. V.; Arakcheeva, A.; Chernyshov, D.; Gibert, M.; Forro, L.; Horvath, E., Optically switched magnetism in photovoltaic perovskite CH3NH3(Mn:Pb)I3. *Nature communications* **2016,** *7*, 13406.
21. Lohmann, S. H.; Cai, T.; Morrow, D. J.; Chen, O.; Ma, X., Brightening of Dark States in CsPbBr(3) Quantum Dots Caused by Light-Induced Magnetism. *Small* **2021,** *17* (37), e2101527.
22. Mir, W. J.; Mahor, Y.; Lohar, A.; Jagadeeswararao, M.; Das, S.; Mahamuni, S.; Nag, A., Postsynthesis Doping of Mn and Yb into CsPbX3 (X = Cl, Br, or I) Perovskite Nanocrystals for Downconversion Emission. *Chem. Mater.* **2018,** *30* (22), 8170-8178.
23. Brown, H. C.; Wallace, W. J., Addition Compounds of Aluminum Halides with Alkyl Halides1. *J. Am. Chem. Soc.* **2002,** *75* (24), 6279-6285.
24. Grattan, D. W.; Plesch, P. H., Ionisation of aluminium halides in alkyl halides. *J. Chem. Soc., Dalton Trans.* **1977,** (18), 1734.
25. Cottingham, P.; Brutchey, R. L., On the crystal structure of colloidally prepared CsPbBr3 quantum dots. *Chem Commun (Camb)* **2016,** *52* (30), 5246-9.
26. Lee, S. M.; Moon, C. J.; Lim, H.; Lee, Y.; Choi, M. Y.; Bang, J., Temperature-Dependent Photoluminescence of Cesium Lead Halide Perovskite Quantum Dots: Splitting of the Photoluminescence Peaks of CsPbBr3 and CsPb(Br/I)3 Quantum Dots at Low Temperature. *The Journal of Physical Chemistry C* **2017,** *121* (46), 26054-26062.
27. Cheng, O. H.; Qiao, T.; Sheldon, M.; Son, D. H., Size- and temperature-dependent photoluminescence spectra of strongly confined CsPbBr3 quantum dots. *Nanoscale* **2020,** *12* (24), 13113-13118.
28. Shinde, A.; Gahlaut, R.; Mahamuni, S., Low-Temperature Photoluminescence Studies of CsPbBr3 Quantum Dots. *The Journal of Physical Chemistry C* **2017,** *121* (27), 14872-14878.
29. Umebayashi, T.; Asai, K.; Kondo, T.; Nakao, A., Electronic structures of lead iodide based low-dimensional crystals. *Physical Review B* **2003,** *67* (15).
30. Butler, K. T.; Frost, J. M.; Walsh, A., Band alignment of the hybrid halide perovskites CH3NH3PbCl3, CH3NH3PbBr3and CH3NH3PbI3. *Materials Horizons* **2015,** *2* (2), 228-231.
31. Mannino, G.; Deretzis, I.; Smecca, E.; La Magna, A.; Alberti, A.; Ceratti, D.; Cahen, D., Temperature-Dependent Optical Band Gap in CsPbBr3, MAPbBr3, and FAPbBr3 Single Crystals. *The journal of physical chemistry letters* **2020,** *11* (7), 2490-2496.
32. Boziki, A.; Dar, M. I.; Jacopin, G.; Gratzel, M.; Rothlisberger, U., Molecular Origin of the Asymmetric Photoluminescence Spectra of CsPbBr3 at Low Temperature. *The journal of physical chemistry letters* **2021,** *12* (10), 2699-2704.

33. Lu, X.; Yang, W.; Jia, Q.; Xu, H., Pressure-induced dramatic changes in organic-inorganic halide perovskites. *Chemical science* **2017,** *8* (10), 6764-6776.
34. Wang, L.; Wang, K.; Zou, B., Pressure-Induced Structural and Optical Properties of Organometal Halide Perovskite-Based Formamidinium Lead Bromide. *The journal of physical chemistry letters* **2016,** *7* (13), 2556-62.
35. Hirotsu, S.; Harada, J.; Iizumi, M.; Gesi, K., Structural Phase Transitions in CsPbBr3. *J. Phys. Soc. Jpn.* **1974,** *37* (5), 1393-1398.
36. Svirskas, Š.; Balčiūnas, S.; Šimėnas, M.; Usevičius, G.; Kinka, M.; Velička, M.; Kubicki, D.; Castillo, M. E.; Karabanov, A.; Shvartsman, V. V.; de Rosário Soares, M.; Šablinskas, V.; Salak, A. N.; Lupascu, D. C.; Banys, J., Phase transitions, screening and dielectric response of CsPbBr3. *Journal of Materials Chemistry A* **2020,** *8* (28), 14015-14022.
37. Wei, K.; Xu, Z.; Chen, R.; Zheng, X.; Cheng, X.; Jiang, T., Temperature-dependent excitonic photoluminescence excited by two-photon absorption in perovskite CsPbBr₃ quantum dots. *Opt. Lett.* **2016,** *41* (16), 3821-4.
38. Lopez, C. A.; Abia, C.; Alvarez-Galvan, M. C.; Hong, B. K.; Martinez-Huerta, M. V.; Serrano-Sanchez, F.; Carrascoso, F.; Castellanos-Gomez, A.; Fernandez-Diaz, M. T.; Alonso, J. A., Crystal Structure Features of CsPbBr3 Perovskite Prepared by Mechanochemical Synthesis. *ACS omega* **2020,** *5* (11), 5931-5938.
39. Palazon, F.; Dogan, S.; Marras, S.; Locardi, F.; Nelli, I.; Rastogi, P.; Ferretti, M.; Prato, M.; Krahne, R.; Manna, L., From CsPbBr(3) Nano-Inks to Sintered CsPbBr(3)-CsPb(2)Br(5) Films via Thermal Annealing: Implications on Optoelectronic Properties. *The journal of physical chemistry. C, Nanomaterials and interfaces* **2017,** *121* (21), 11956-11961.
40. Chen, Y.; Smock, S. R.; Flintgruber, A. H.; Perras, F. A.; Brutchey, R. L.; Rossini, A. J., Surface Termination of CsPbBr3 Perovskite Quantum Dots Determined by Solid-State NMR Spectroscopy. *J. Am. Chem. Soc.* **2020**.
41. Bodnarchuk, M. I.; Boehme, S. C.; Ten Brinck, S.; Bernasconi, C.; Shynkarenko, Y.; Krieg, F.; Widmer, R.; Aeschlimann, B.; Gunther, D.; Kovalenko, M. V.; Infante, I., Rationalizing and Controlling the Surface Structure and Electronic Passivation of Cesium Lead Halide Nanocrystals. *Acs Energy Lett* **2019,** *4* (1), 63-74.
42. Li, C.; Wang, A.; Xie, L.; Deng, X.; Liao, K.; Yang, J.-a.; Li, T.; Hao, F., Emerging alkali metal ion (Li+, Na+, K+ and Rb+) doped perovskite films for efficient solar cells: recent advances and prospects. *Journal of Materials Chemistry A* **2019,** *7* (42), 24150-24163.
43. Huang, G.; Wang, C.; Xu, S.; Zong, S.; Lu, J.; Wang, Z.; Lu, C.; Cui, Y., Postsynthetic Doping of MnCl(2) Molecules into Preformed CsPbBr(3) Perovskite Nanocrystals via a Halide Exchange-Driven Cation Exchange. *Adv. Mater.* **2017,** *29* (29).
44. Aggarwal, R. L.; Jasperson, S. N.; Becla, P.; Furdyna, J. K., Optical determination of the antiferromagnetic exchange constant between nearest-neighbor Mn2+ ions in Zn0.95Mn0.05Te. *Physical review. B, Condensed matter* **1986,** *34* (8), 5894-5896.

General conclusion and perspectives

Conclusion

This thesis had three main objectives: to passivate $CsPbBr_3$ NCs with an AlO_x shell, to integrate the obtained core/shell NCs into a nanopatch antenna structure and evaluate their potential as single photon emitters, as well as to dope $CsPbX_3$ (X = Br, I) NCs with Mn^{2+} and investigate the magneto-optical properties. In general, the syntheses of the core/shell structure, doped NCs, and the fabrication of the antenna structure were successful. Moreover, the core/shell structure displayed a clear enhancement in photostability, and an emission rate increase from the antenna structure was recorded, however, no giant Zeeman splitting was observed in the case of the Mn-doped NCs.

To grow an AlO_x shell with controllable thickness, we decided to use a nonhydrolytic sol-gel reaction due to the lower reaction rate compared to sol-gel reactions involving water. The challenge of this method was to anchor the primary shell precursor $AlBr_3$ on the surface of the core NCs. To facilitate this step, we first explored an intermediate layer of $Pb(OA)_2$ between the $CsPbBr_3$ NCs and $AlBr_3$. Despite indications from XPS and FTIR that $AlBr_3$ was successfully grafted on the core and that AlO_x subsequently formed, the photostability test showed no improvement of the core/shell structure over core NCs. In this process, we discovered that by changing the solvent of the $AlBr_3$ solution, we can control whether or not Al^{3+} is doped into the $CsPbBr_3$ NCs. By optimizing the solvent mixture for $AlBr_3$, we managed to graft it on the core NCs and form the AlO_x shell. The core/shell NCs demonstrated enhanced PLQY (94.1% compared to 84.5% for the core NCs), as well as improved photostability under 405 nm laser irradiation at 154 W/cm^2. Finally, we found a way to control the thickness the shell.

Second, we constructed a nanopatch antenna structure where Ag nanocubes were deposited on a thin film containing $CsPbBr_3$ core or core/shell NCs encapsulated with PMMA. We found that the density of the NCs film can be controlled from single particles to a dense monolayer by decreasing the rotation speed during spin coating and by functionalizing the substrate surface with APTES molecules. The choice of the PMMA chain length, reflected by the average molecular weight, and polymer/NCs volume ratio strongly affected the morphology of the NCs film. In our case, PMMA with an average molecular weight of ~120 000 was much more efficient than 950 000 due to the reduced intramolecular interaction in the polymer and increased polymer-NCs binding. Finally, we synthesized Ag nanocubes of 71 ± 13 nm in size. The nanopatch antenna's performance was assessed, however we did not observe an intensity enhancement of the emission of NCs placed under the Ag nanocubes because of the PL contribution from NCs surrounding the antenna. However, a two-fold decrease in the charge carrier lifetime was recorded in the sample with the antenna, implying that the structure could accelerate the charge recombination as targeted.

Finally, we studied the behavior of $CsPbBr_3$ NCs doped with Al^{3+} and Mn^{2+}. Using $AlBr_3$, Al doping became possible by using CH_2Br_2 as the solvent, likely because it dissociates the bulky Al_2Br_6 dimer into $AlBr_3$. The incorporation of Al^{3+} contracted the lattice parameter of $CsPbBr_3$ and blue-shifted the emission wavelength of the host. The degree of the shift was found to be linearly correlated to the decrease in the lattice parameter. On the contrary, low-temperature structural and optical studies demonstrated that as the lattice shrank, the emission wavelength red-shifted, revealing that structural disorder such as tilting of the $PbBr_6$ octahedra has also to be taken into account when discussing the evolution of the band gap energy and hence of the PL peak position. Post-synthetic Mn-doping was facilitated by $MnBr_2$ and MnI_2. With the latter, partial substitution of Br^- by I^- also occurred, reducing the band gap of the host NCs. Despite the successful doping of Mn^{2+}, giant Zeeman splitting was not

observed at a magnetic field of 0.5 T. The reason could be the low value of the magnetic field used, or inhomogeneous broadening masking the emission peak shift.

Perspectives

The AlO_x shell does not only passivate the $CsPbBr_3$ NCs but can also allow more modifications to the system in terms of chemistry. The most important property is that the core/shell structure will be more hydrophilic than the core NCs. As a result, the addition of polar ligands can render the NCs dispersible in water, and their stability in the polar solvent is ensured by the shell. Additionally, the shell thickness can be optimized to provide maximal protection to the core NCs while retaining high PLQY.

Unfortunately, the lengthy progress of shell growth and antenna fabrication did not allow us to delve deeper into the characterization of the antenna structure and the Mn-doped NCs. For the nanopatch antenna, the main reason was that the photoluminescence of NCs far from the antenna was not quenched properly by the Au layer underneath. This problem can be solved by controlling the density of the NCs in the layer, or by quenching the PL of NCs surrounding the antenna by the electron beam during SEM measurements Afterward, characterizations of the photostability of the system and the dependence of the emission intensity on the irradiation power can be performed with more ease and accuracy. Finally, the fabrication of the nanopatch antenna structure with single NCs can be attempted.

The study of Mn-doped NCs is only in a preliminary stage. First of all, the instrumental limitation only allowed us to apply a weak magnetic field (0.5 T). By using an advanced setup, a magnetic field up to 11 T can be achieved. Second, the density of the NCs in the thin film can be reduced so that single particles can be measured, which can help to resolve better the giant Zeeman splitting. We also demonstrated that Mn-doping can be accompanied by band gap tuning for $CsPbX_3$ (X = Br, I). As the sp–d exchange is dependent on the position of the host's band edges, it is important to investigate the magneto-optical properties of the doped NCs as a function of the band gap. Finally, the dopant concentration can be reduced to a single dopant per NC. The interaction between the carrier spin with a single Mn spin is different compared to the interaction with the spins of many dopant atoms, and its investigation will give a complete picture of the spin-carrier interaction in the Mn-doped lead halide perovskite system paving the way for its future use in spintronics and spin-polarized light emitting diodes.

Appendices

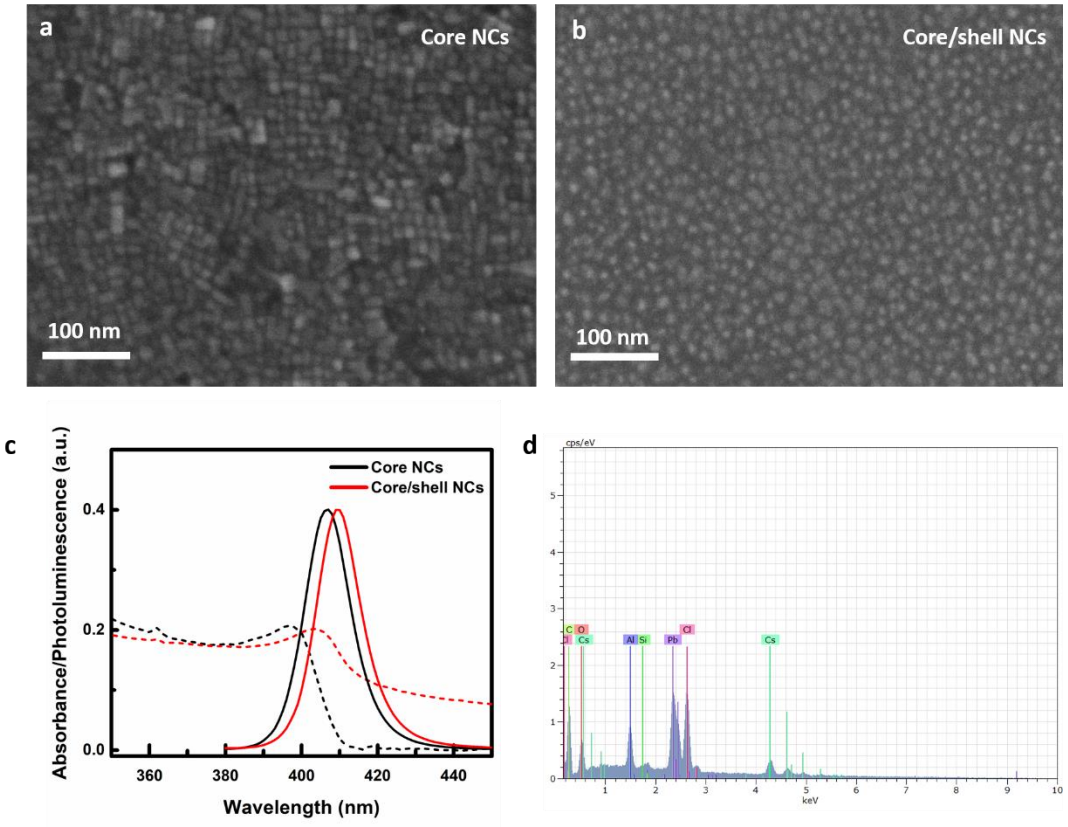

Figure S1. a, b) SEM images of $CsPbCl_3$ core and $CsPbCl_3/AlO_x$ core/thin shell NCs synthesized by using $AlCl_3$/toluene and $Al(IPA)_3$ without $Pb(OA)_2$ treatment, c) Absorption and emission spectra for core and core/shell NCs, d) Elemental composition of $CsPbCl_3/AlO_x$ NCs showing the strong presence of Al.

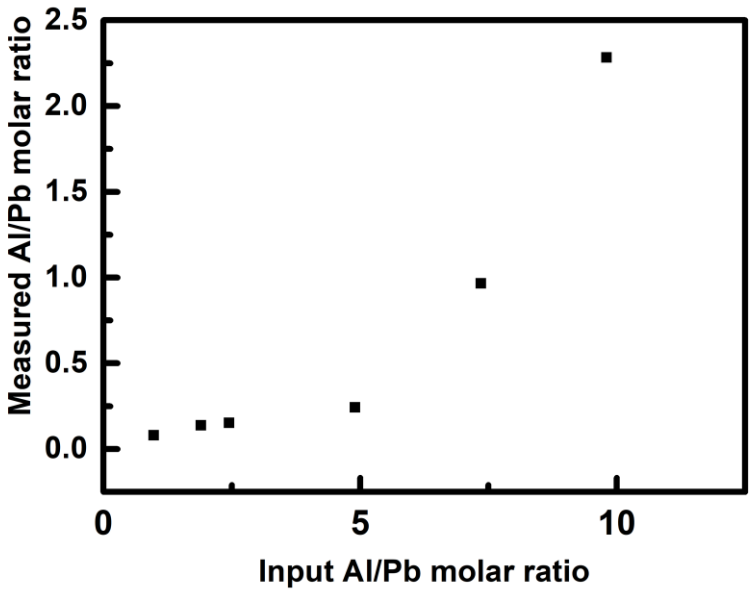

Figure S2. Relationship between input and measured Al/Pb molar ratio in Al-doped $CsPbBr_3$ NCs.

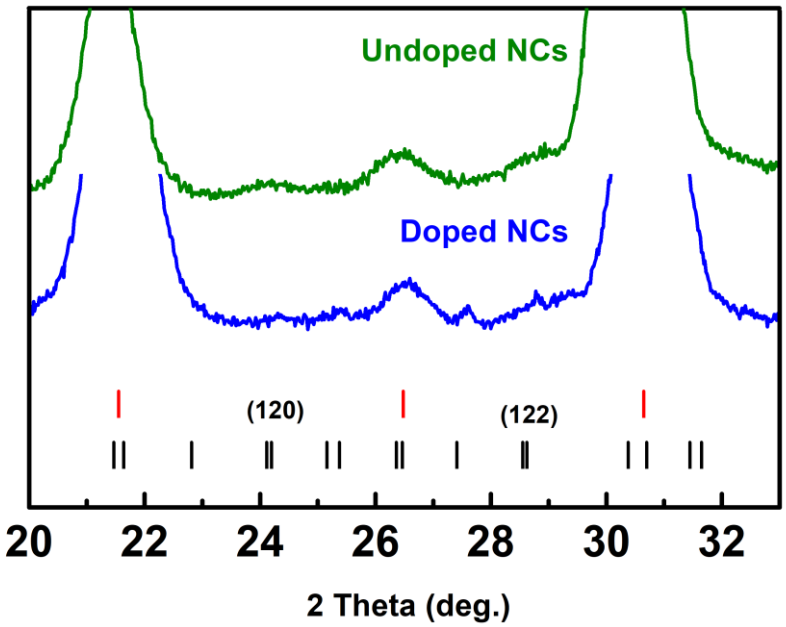

Figure S3. Zoomed in XRD pattern of undoped and doped NCs showing orthorhombic peaks

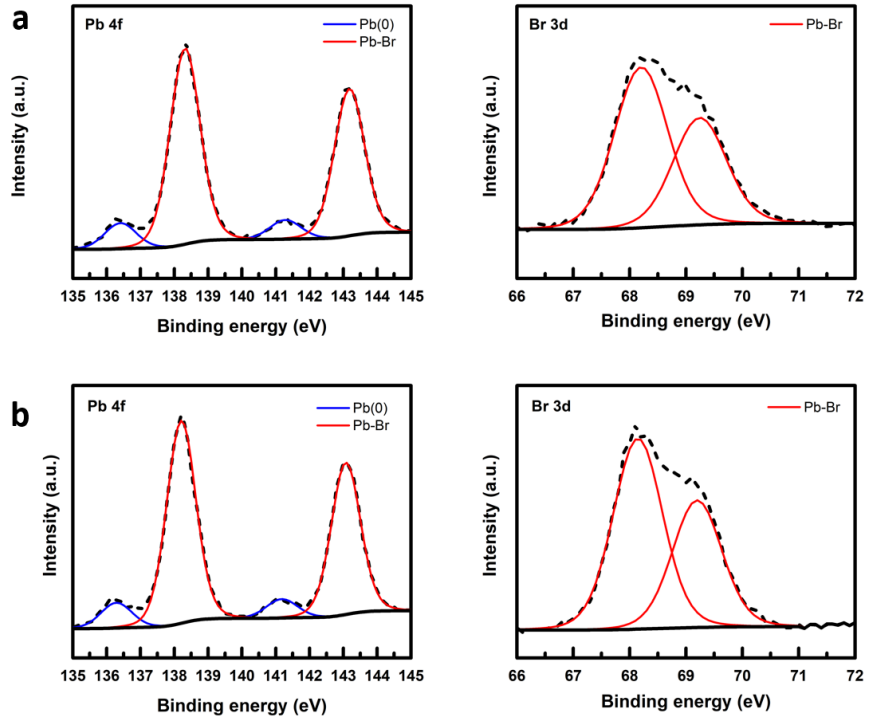

Figure S4. Pb and Br XPS spectra of a) undoped and b) doped samples (Al/Pb input ratio 2.5)

Abstract

Lead halide perovskites have received great research interest in the past decade thanks to their excellent optoelectronic properties. Initially studied by the photovoltaic community, the material quickly became popular in quantum dots research after reliable synthetic routes to high-quality perovskite nanocrystals were devised. One important research direction for these nanocrystals is quantum technology. As devices operate with the principles of quantum mechanics, quantum-confined nanocrystals will become an essential component, with applications in single photon sources and spintronics. In a single photon source, a single nanocrystal plays the role of the emitter, and by proper excitation as well as the design of the surrounding medium, single photons can be emitted at determined interval and direction. In contrast to single photon sources, where only the intrinsic optical properties of nanocrystals are concerned, the use of nanocrystals in spintronics depends on the effects resulting from doping the particles with magnetic ions and creating a class of material known as diluted magnetic semiconductors. For lead halide perovskites, only a limited number of studies have been conducted compared to II-VI and III-V semiconductors. However, the research on perovskites, especially nanocrystals, is challenged by the poor stability of the materials. Therefore, this thesis has been carried out with the aim to passivate lead halide perovskite nanocrystals on a single particle level with an oxide shell, then study their integration into a single photon source structure known as nanopatch antenna, and their magneto-optical properties when doped with Mn^{2+} ions. The major results were i) the successful overcoating of $CsPbBr_3$ nanocrystals with a homogeneous alumina shell, which led to an improvement of their photostability, and their successful incorporation into a nanopatch antenna device structure using silver nanocubes as resonators; ii) the doping of $CsPbBr_3$ nanocrystals with aluminum, giving rise to a controllable blueshift of the absorption and emission spectra; iii) the controlled doping of $CsPbBr_3$ nanocrystals with Mn^{2+} and the study of the magneto-optical properties.

Résumé

Les pérovskites halogénées de plomb ont suscité un grand intérêt au cours de la dernière décennie grâce à leurs excellentes propriétés optoélectroniques. Initialement étudié par la communauté photovoltaïque, ces matériaux sont rapidement devenus populaires dans la recherche sur les points quantiques (quantum dots) après la mise au point de méthodes de synthèse pour obtenir des nanocristaux de pérovskite de haute qualité. La technologie quantique est un axe de recherche important pour ces nanocristaux. Pour les dispositifs fonctionnant selon les principes de la mécanique quantique, les quantum dots dont les propriétés obéissent les mêmes lois peuvent devenir un composant essentiel, avec des applications notamment dans les sources de photons uniques et la spintronique. Dans la première, un nanocristal unique joue le rôle d'émetteur et, grâce à une excitation appropriée et à la conception du milieu environnant, des photons uniques peuvent être émis à un intervalle et dans une direction déterminés. Contrairement à cette application, où seules les propriétés optiques intrinsèques des nanocristaux sont concernées, l'utilisation des nanocristaux en spintronique dépend des effets résultant du dopage des particules avec des ions magnétiques et de la création d'une classe de matériaux connus sous le nom de semi-conducteurs magnétiques dilués. En ce qui concerne l'utilisation des pérovskites halogénées de plomb pour ces applications, seul un nombre très limité d'études a été mené par rapport aux semi-conducteurs II-VI et III-V. La recherche sur les pérovskites, en particulier sous forme de nanocristaux, est confrontée à la faible stabilité de ces matériaux. Cette thèse a été réalisée dans le but de passiver les nanocristaux de pérovskite halogénée au niveau de la particule individuelle avec une coquille d'oxyde, puis d'étudier leur intégration dans une structure de source de photons uniques (nano-antenne patch), et leurs propriétés magnéto-optiques lorsqu'ils sont dopés avec des ions Mn^{2+}. Les principaux résultats sont i) la synthèse de nanocristaux de $CsPbBr_3$ avec une coquille d'alumine homogène, qui a conduit à une amélioration de leur photo-stabilité, et leur incorporation réussie dans une structure photonique avec des nanocubes d'argent agissant comme antenne ; ii) le dopage des nanocristaux de $CsPbBr_3$ avec de l'aluminium, donnant lieu à un décalage bleu contrôlable des spectres d'absorption et d'émission ; iii) le dopage contrôlé des nanocristaux de $CsPbBr_3$ avec du Mn^{2+} et l'étude des propriétés magnéto-optiques.